Title
Earthquake locations and seismic velocity models for Southern California

Author
Lin, Guoqing

Publication Date
2007

Peer reviewed|Thesis/dissertation

UNIVERSITY OF CALIFORNIA, SAN DIEGO

Earthquake Locations and Seismic Velocity Models for Southern California

A dissertation submitted in partial satisfaction of the
requirements for the degree Doctor of Philosophy
in
Earth Sciences

by

Guoqing Lin

Committee in charge:

Professor Peter M. Shearer, Chair
Professor Scott Ashford
Professor Neal Driscoll
Professor J.-Bernard Minster
Professor Robert L. Parker

2007

The dissertation of Guoqing Lin is approved, and it is
acceptable in quality and form for publication on microfilm:

Chair

University of California, San Diego

2007

To my parents —

for their upbringing, support and love throughout my life

TABLE OF CONTENTS

LIST OF TABLES

LIST OF FIGURES

ACKNOWLEDGMENTS

My study as a graduate student at Scripps Institution of Oceanography has come to an end. During this long journey at IGPP, I have learned so much from people around here and I would not have been able to come to this point and finish this thesis without the extensive help from many people. I am deeply grateful to all of them. In particular, I am in great debt of my advisor, Professor Peter Shearer. Peter helps me find interesting problems to work on and shares his knowledge of seismology with me. He always encourages me to go to different meetings to present myself, has an open door to me answering my questions in patience, wants to hear about latest research results, and has endless suggestions of new ways to approach problems. Peter has been a great support for me through hard times with his encouragement and confidence in me. I am grateful beyond words for this life changing and great experience to work with him.

I would also like to acknowledge the members of my dissertation committee. I thank Bob Parker for his theoretical point of view and suggestions of my research and also for his advice and help in one of my papers. I thank Bernard Minster for his enthusiasm about my research, his encouragement to me and his cheerful talks. I thank Neal Driscoll and Scott Ashford for their time, their interest and their help in my work. I feel very fortunate to have such a great committee.

My deep gratitude also goes to my co-authors, Yuri Fialko, Egill Hauksson at Caltech and Cliff Thurber at UW-Madison. Yuri helped me get to know topography data and always provided me prompt help whenever I needed it. Egill hosted a few meetings at Caltech to discuss our research and helped me understand the tomographic code better. I thank him for his great suggestions and help in our collaboration. Cliff unselfishly provided me his tomographic code for my research. I thank him for his valuable suggestions and comments in the 3D velocity model study, especially during my visit to his group in 2006.

I would also like to thank George Backus, David Sandwell, Duncan Agnew, Debi Kilb and all the other faculty and researchers at IGPP who either taught me classes or helped me with my research. I have learned a lot from them.

The NetOps staff, particularly Edward Riesgo, Chris Garrod, and Wayne Chen, are of great help to me. I thank them for their computer assistance and patience waiting for my programs to finish up.

I would never have made it past the first year of my graduate school if it weren't for the help of my first-year classmates: Urška Manners, Germán Prieto, Vince Morton and Troy Swift. They were not only my study companions but also my English teachers. I thank them for their nice help to me. My former and current office-mates, Fiona Sutherland, Scott Nooner and Ashley Medin, deserve my full appreciation for providing a nice, quiet and friendly working environment. I would also like to thank Shearer seismology group, Elizabeth Cochran, Kris Walker and Jesse Lawrence, for their share of knowledge in science and life at group lunches and field trips.

Great thanks also go to my dear friends who have made my life during the past few years much more fun and easier. I thank Shenfu Dong, who has always been there for me sharing every moment with me like an older sister and helped me a lot in my personal life. Karen Weitemeyer, you started as a dancing companion and then became a great friend. I enjoy the dancing, running, swimming and small talks with you. Bettina Allmann and Alexander Goertz, going to concerts and performances with you guys makes my life colorful. I thank Chen-fen Huang, who always liked to discuss research with me and helped me a lot when I just got here. I am very fortunate to have such good friends as you all. I would also like to thank Hui Zhang, Jui-Yuan Chang, Satoko Oki, Meng Wei, Aihua Zhu, Hongxin Guo, Yaofeng He for their friendship.

My endless love goes to my parents and my sister. My mom and dad have been caring for and worrying about me since the day I was born. They are always there for me, listening to my small talks everyday. Without their support and love, I would never have made the big move to graduate school in the first place and would never have been able to come to this point. My dad always inspires me to take an interest in science and enjoy what I am doing. My mom is not only a parent, but also a mentor and a greatest friend of mine. She always shines my world and makes me believe in myself. My little sister, Anran, is an awesome and sweetest sister that anyone could have. Having such a great family is the most

fortunate thing in my life.

The text of Chapters Two, Three, Four and Five, in full, are reprints of the material as it appears in the Journal of Geophysical Research, Bulletin of Seismological Society of America, Seismological Research Letter, respectively. The text of Chapter Six and Seven have been submitted, in full, to the Journal of Geophysical Research. The dissertation author was the primary researcher and author on each of these and the co-authors listed directed and supervised the research that formed the basis for these chapters.

VITA

2002	B.S., in Geophysics Peking University, P. R. China
2007	Ph.D., in Earth Sciences University of California, San Diego

PUBLICATIONS

Lin, G., P. M. Shearer, and E. Hauksson, A search for temporal variations in station corrections in southern California from 1984 to 2002, in preparation.

Lin, G., P. M. Shearer, and E. Hauksson, Applying a 3D velocity model, waveform cross-correlation, and cluster analysis to locate southern California seismicity from 1981 to 2005, *submitted to J. Geophys. Res.*, 2007.

Lin, G., P. M. Shearer, E. Hauksson and C. H. Thurber, A 3-D crustal seismic velocity model for southern California from a composite event method, *submitted to J. Geophys. Res.*, 2007.

Lin, G. and P. M. Shearer, Estimating local V_p/V_s ratios within similar earthquake clusters, *Bull. Seism. Soc. Am.*, in press, 2007.

Guzofski, C. A., J. H. Shaw, G. Lin, and P. M. Shearer, Seismically active wedge structure beneath the Coalinga anticline, San Joaquin basin, California, *J. Geophys. Res.*, in press, 2007.

Lin, G. and P. M. Shearer, The COMPLOC 1.0 Earthquake Location Package, *Seism. Res. Lett.*, 77, 440-444, 2006.

Lin, G., P. M. Shearer, and Y. A. Fialko, Obtaining absolute locations for quarry seismicity using remote sensing data, *Bull. Seism. Soc. Am.*, 96, 722-728, 2006.

Shearer, P. M., E. Hauksson, and G. Lin, Southern California hypocenter relocation with waveform cross-correlation, Part 2: results using source-specific station terms and cluster analysis, *Bull. Seism. Soc. Am.*, 95, 904-915, 2005.

Lin, G. and P. M. Shearer, Tests of relative earthquake location techniques using synthetic data, *J. Geophys. Res.*, Vol. 110, B04304, doi: 10.1029/2004JB003380, 2005.

SELECTED ABSTRACTS

Shearer, P. M., G. Lin, and E. Hauksson, Refined locations for southern California earthquakes from 1981 to 2005, *Fall AGU meeting*, 2006.

Lin, G. and P. M. Shearer, Estimating local V_p/V_s ratios within similar earthquake clusters, *Fall AGU meeting*, 2006.

Lin, G. and P. M. Shearer, 3-D velocity models and earthquake locations in southern California using a new cross-correlation location method, *SSA meeting*, 2006.

Lin, G. and P. M. Shearer, 3-D velocity models and earthquake locations in southern California, *Fall AGU meeting*, 2005.

Lin, G. and P. M. Shearer, An Easy-to-Operate Earthquake Location Package: COMPLOC_1.0, *SCEC meeting*, 2005.

Shearer, P. M., G. Lin, G. Prieto and F. Vernon, The 2001 and 2005 Anza earthquakes: aftershock locations and source-time functions, *SCEC meeting*, 2005.

Walker, K., D. Kilb and G. Lin, The 2001 and 2005 Anza earthquakes: aftershock focal mechanisms, *SCEC meeting*, 2005.

Allmann, B., P. M. Shearer, and G. Lin, Stress drop variations in the Parkfield segment of the SAF from earthquake source spectra, *SCEC meeting*, 2005.

Lin, G., P. M. Shearer, E. Hauksson, and C. H. Thurber, Earthquake locations in southern California obtained from 3-D velocity inversion and waveform cross-correlation times, *SSA meeting*, 2005.

Lin, G. and P. M. Shearer, Synthetic earthquake location tests in southern California with new cross-correlation results, *Fall AGU meeting*, 2004.

Lin, G. and P. M. Shearer, Tests of relative earthquake location techniques using both synthetic and real data, *SSA meeting*, 2004.

Lin, G. and P. M. Shearer, Tests of relative earthquake location techniques using both synthetic and real data, *Fall AGU meeting*, 2003.

Shearer, P. M., E. Hauksson, G. Lin and D. Kilb, Comprehensive waveform cross-correlation of southern California seismograms: Part 2. Event locations obtained using cluster analysis. *Eos Trans. AGU, 84(46), Fall Meet. Suppl.*, Abstract S21D-0326, 2003.

FIELDS OF STUDY

Major Field: Earth Science (Geophysics)

Studies in Seismology
Professor Guy Masters, Bernard Minster and Peter Shearer

Studies in Gravity and Geomagnetism
Professor Bob Parker

Studies in Physics of Earth Material
Professor Duncan Agnew and Yuri Fialko

Studies in Marine Geology
Professor Christopher Charles, Jeffrey Gee, and David Hilton

Studies in Geophysical Data Analysis
Professor Duncan Agnew, Cathy Constable, and Frank Vernon

Studies in Geophysical Inverse Theory
Professor Cathy Constable and Steve Constable

Studies in Geodynamics
Professor Yuri Fialko and David Sandwell

ABSTRACT OF THE DISSERTATION

Earthquake Locations and Seismic Velocity Models
for Southern California

by

Guoqing Lin
Doctor of Philosophy in Earth Sciences
University of California, San Diego, 2007

Professor Peter M. Shearer, Chair

Earthquake locations are fundamental to studies of earthquake physics, fault orientations and Earth's deformation. Improving earthquake location accuracy has been an important goal branch in seismology for the past few decades. In this dissertation, I consider several methods to improve both relative and absolute earthquake locations. Chapter 2 is devoted to the comparison of different relative earthquake location techniques based on synthetic data, including the double-difference and source-specific station term (SSST) method. The shrinking box SSST algorithm not only provides similar improvements in relative earthquake locations compared to other techniques, but also improves absolute location accuracy compared to the simple SSST method. Chapter 4 describes and documents the COMPLOC software package for implementing the shrinking box SSST algorithm. Chapter 3 shows how absolute locations for quarry seismicity can be obtained by using remote sensing data, which is useful in providing absolute reference locations for three-dimensional velocity inversions and to constrain the shallow crustal structure in simultaneous earthquake location and velocity inversions. Chapter 5 presents and tests a method to estimate local V_p/V_s ratios for compact similar earthquake clusters using the precise P- and S- differential times obtained using waveform cross-correlation. Chapter 6 describes a new three-dimensional seismic velocity model for southern California obtained using the "composite event method" applied to the SIMULPS tomographic inversion algorithm. Based on this velocity model and waveform cross-correlation, Chapter 7 describes how a new earthquake location catalog is obtained for about 450,000 southern California earthquakes between 1981 and 2005.

Chapter 1

Introduction

1.1 Overview

Earthquake locations are fundamental for studies of earthquake physics, fault orientations and Earth's deformation. Improving earthquake location accuracy has been an important and challenging goal in seismology for the past few decades.

Standard location methods are based on Geiger's method (Geiger, 1912) and became more practical with the development of modern computers. The basic methodology is essentially unchanged from the classic papers of Bolt (1960), Flinn (1965) and Engdahl and Gunst (1966). The nonlinear earthquake location problem can be linearized using iterative methods if the starting locations are perturbed slightly from the true locations. The predicted arrival times for a starting location (hypocenter and origin time) are calculated for each receiver using a fixed (usually one-dimensional) velocity model. The arrival time residuals (observed time minus predicted time) can be related to the hypocenter perturbations so that the event location can be updated until some program termination criteria are satisfied (e.g., reaching a specified level of data misfit or data misfit change, perturbation step size, or reaching a set maximum number of iterations). Classical methods locate each event separately using one-dimensional velocity models. But due to inaccuracies and limitations in the velocity model, the locations are often biased (see Figure 1.1).

Several algorithms have been developed to reduce the effect of errors in the travel time model by locating many events at the same time. These include joint hypocenter determination (e.g., Douglas, 1967; Frohlich, 1979), the hypocentroidal decomposition method (Jordan and Sverdrup, 1981), and more recently, the source-specific station term (SSST) method (Richards-Dinger and Shearer, 2000; Lin and Shearer, 2005) and the double-difference (DD) method (Waldhauser and Ellsworth, 2000). These methods attempt to correct for correlated effects on travel times caused by three-dimensional velocity structure by explicitly or implicitly solving for station corrections from arrival time residuals. Significant improvements in relative locations can be achieved by these methods, especially by the SSST and DD methods for distributed seismicity.

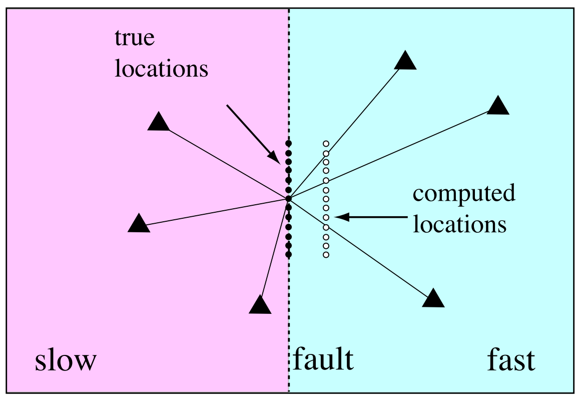

Figure 1.1. Cartoon illustrating how earthquake locations derived from a 1-D velocity model can be biased by lateral velocity heterogeneities.

Although relative location accuracy can be improved by the SSST and DD methods, the absolute earthquake locations are not changed much. Since the 1980s, tomography methods have been used to improve absolute locations for local events by accounting for crustal-scale three-dimensional velocity structure (e.g., Thurber, 1983, 1992; Thurber and Eberhart-Phillips, 1999; Zhang and Thurber, 2003). This is typically done by simultaneously solving for the three-dimensional velocity structure and earthquake locations for local events.

During the last 10 years, waveform cross-correlation has been an increasingly important tool for improving relative locations among nearby events because of the great accuracy of differential times (Nakamura, 1978; Got *et al.*, 1994; Dodge *et al.*, 1995; Nadeau *et al.*, 1995; Gillard *et al.*, 1996; Rubin *et al.*, 1999; Waldhauser *et al.*, 1999). Large earthquake location catalogs based on waveform cross-correlation have been developed (e.g., Hauksson and Shearer, 2005; Shearer *et al.*, 2005; Schaff and Waldhauser, 2005).

Improved earthquake locations help to better delineate fault structures and characterize the spatial and temporal characteristics of seismicity. High-resolution event catalogs in southern California have recently been used to study the decay of aftershock density with distance (Felzer and Brodsky, 2006), explore the spatial relationship between aftershocks and mainshock rupture planes (Liu *et al.*, 2003; Powers and Jordan, 2005), analyze the fractal dimension of seismicity (Kagan, 2006), and assess the mechanisms driving seismic swarms (Lohman and McGuire, 2006).

1.2 Thesis Organization

My Ph.D. research has considered several aspects of improvements in earthquake locations. The major contents of this dissertation consist of six chapters, from Chapter 2 to Chapter 7. In Chapter 2, I compare different relative earthquake location techniques based on synthetic data that simulate most of the statistical properties of real data. Chapter 3 shows how to obtain absolute locations for quarry seismicity by using remote sensing data. Chapter 4 describes the COMPLOC software package for the source-specific station term location method with phase data only. Chapter 5 presents a method to estimate local V_p/V_s ratios for compact similar earthquake clusters using the precise P- and S- differential times obtained using waveform cross-correlation. Chapter 6 is devoted to a new three-dimensional seismic velocity model for southern California. Chapter 7 demonstrates how a new earthquake location catalog is obtained for about 450,000 southern California earthquakes between 1981 and 2005 based on the new three-dimensional velocity model, waveform cross-correlation and cluster analysis. Finally, Chapter 8 addresses the conclusions of the thesis and suggestions for future research.

1.3 References

Bolt, B. A. (1960). The revision of earthquake epicenters, focal depths and origin times using a high-speed computer. *Geophys. J. R. Astron. Soc.*, **3**, 433–440.

Dodge, D. A., G. C. Beroza and W. L. Ellsworth (1995). Foreshock sequence of the 1992 Landers, California, earthquake and its implications for earthquake nucleation. *J. Geophys. Res.*, **100**, 9865–9880.

Douglas, A. (1967). Joint epicentre determination. *Nature*, **215**, 47–48.

Engdahl, E, R. and R. H. Gunst (1966). Use of a high speed computer for the preliminary determination of earthquake hypocenters. *Bull. Seismol. Soc. Am.*, **56**, 325–336.

Felzer, K. R. and E. E. Brodsky (2006). Decay of aftershock density with distance indicates triggering by dynamic stress. *Nature*, **441**, 735–738.

Flinn, E. A. (1965). Confidence regions and error determinations for seismic event location. *Rev. Geophys.*, **3**, 157–185.

Frohlich, C. (1979). An efficient method for joint hypocenter determination for large groups of earthquakes. *Computers & Geosciences*, **5**, 387–389.

Geiger, L. (1912). Probability method for the determination of earthquake epicenters from the arrival time only. *Bull. St. Louis Univ.*, **8**, 60–71.

Gillard, D., A. M. Rubin and P. Okubo (1996). Highly concentrated seismicity caused by deformation of Kilauea's deep magma system. *Nature*, **384**, 343–346.

Got, J.-L., J. Fréchet and F. W. Klein (1994). Deep fault plane geometry inferred from multiplet relative relocation beneath the south flank of Kilauea. *J. Geophys. Res.*, **99**, 15,375–15,386.

Hauksson, E. and P. Shearer (2005). Southern California hypocenter relocation with waveform cross-correlation, Part 1: results using the double-difference method. *Bull. Seismol. Soc. Am.*, **95**, 896–903.

Jordan, T. H. and K. A. Sverdrup (1981). Teleseismic location techniques and their application to earthquake clusters in the south-central Pacific. *Bull. Seismol. Soc. Am.*, **71**, 1105–1130.

Kagan, Y. Y. (2006). Earthquake spatial distribution: the correlation dimension. *Geophys. J. Int.*, doi:10.1111/j.1365–246X.2006.03251.x.

Lin, G. and P. M. Shearer (2005). Tests of relative earthquake location techniques using synthetic data. *J. Geophys. Res.*, **110**, B04304, doi: 10.1029/2004JB003380.

Liu, J., K. Sieh and E. Hauksson (2003). A structural interpretation of the aftershock "cloud" of the 1992 Mw 7.3 Landers Earthquake. *Bull. Seismol. Soc. Am.*, **93**, 1333–1344.

Lohman, R. B. and J. J. McGuire (2006). Earthquake swarms driven by aseismic creep in the Salton Trough, CA. *Water Resources Research*, under revision.

Nadeau, R. M., W. Foxall and T. V. McEvilly (1995). Clustering and periodic recurrence of microearthquakes on the San Andreas Fault at Parkfield, California. *Science*, **267**, 503–507.

Nakamura, Y. (1978). A_1 moonquakes: source distribution and mechanism. *Proc. Lunar Planet. Sci. Conf.*, **9**, 3589–3607.

Powers, P. and T. Jordan (2005). Seismicity rate vs. distance from strike-slip faults in southern California. *Eos Trans. AGU*, **86**, S13B–0199.

Richards-Dinger, K. B. and P. M. Shearer (2000). Earthquake locations in southern California obtained using source-specific station terms. *J. Geophys. Res.*, **105**, 10,939–10,960.

Rubin, A. M., D. Gillard and J.-L. Got (1999). Streaks of microearthquakes along creeping faults. *Nature*, **400**, 635–641.

Schaff, D. P. and F. Waldhauser (2005). Waveform cross-correlation-based differential travel-time measurements at the Northern California Seismic Network. *Bull. Seismol. Soc. Am.*, **95**, 2446–2461.

Shearer, P. M., E. Hauksson and G. Lin (2005). Southern California hypocenter relocation with waveform cross-correlation, Part 2: results using source-specific station terms and cluster analysis. *Bull. Seismol. Soc. Am.*, **95**, 904–915.

Thurber, C. and D. Eberhart-Phillips (1999). Local earthquake tomography with flexible gridding. *Comp. Geosci.*, **25**, 809–818.

Thurber, C. H. (1983). Earthquake locations and three-dimensional crustal structure in the Coyote Lake area, central California. *J. Geophys. Res.*, **88**, 8226–8236.

Thurber, C. H. (1992). Hypocenter-velocity structure coupling in local earthquake tomography. *Phys. Earth Planet. Inter.*, **75**, 55–62.

Waldhauser, F. and W. L. Ellsworth (2000). A double-difference earthquake location algorithm: method and application to the Northern Hayward Fault, California. *Bull. Seismol. Soc. Am.*, **90**, 1353–1368.

Waldhauser, F., W. L. Ellsworth and A. Cole (1999). Slip-parallel seismic lineations on the northern Hayward Fault, California. *Geophys. Res. Lett.*, **26**, 3525–3528.

Zhang, H. and C. H. Thurber (2003). Double-difference tomography: the method and its application to the Hayward Fault, California. *Bull. Seismol. Soc. Am.*, **93**, 1875–1889.

Chapter 2

Tests of Relative Earthquake Location Techniques Using Synthetic Data

Abstract. We compare three relative earthquake location techniques using tests on synthetic data that simulate many of the statistical properties of real travel time data. The methods are (1) the hypocentroidal decomposition method of Jordan and Sverdrup (1981), (2) the source-specific station term method (SSST) of Richards-Dinger and Shearer (2000), and (3) the modified double-difference method (DD) of Waldhauser and Ellsworth (2000). We generate a set of synthetic earthquakes, stations and arrival time picks in half-space velocity models. We simulate the effect of travel time variations caused by random picking errors, station terms, and general three-dimensional velocity structure. We implement the algorithms with a common linearized approach and solve the systems using a conjugate gradient method. We constrain the mean location shift to be zero for the hypocentroidal decomposition and double-difference locations. For a single compact cluster of events, these three methods yield very similar improvements in relative location accuracy. For distributed seismicity, the DD and SSST algorithms both provide improved relative locations of comparable accuracy. We also present a new location technique, termed the shrinking box SSST method, which provides some improvement in absolute location accuracy compared to the SSST method. In our implementation of these algorithms, the SSST method runs significantly faster than the DD method.

2.1 Introduction

The classic problem of locating earthquakes using arrival time data has recently been revitalized by methods that can greatly improve the relative location accuracy among nearby events, even when the arrival times are biased by the effects of three-dimensional velocity structure. These new methods include the double-difference algorithm (Waldhauser and Ellsworth, 2000, 2002) and source-specific station terms (Richards-Dinger and Shearer, 2000). Both of these techniques represent generalizations to distributed seismicity of methods that have previously been applied to isolated clusters of events, such as joint epicenter determination, station terms, and master event locations (e.g., Douglas, 1967; Evernden, 1969; Lilwall and Douglas, 1970; Frohlich, 1979; Jordan and Sverdrup, 1981; Smith, 1982; Pavlis and Booker, 1983; Viret *et al.*, 1984; Pujol, 1988). All of these methods attempt to correct for the systematic biases in arrival times caused by three-dimensional velocity variations without actually solving for the velocity structure itself. They are effective in reducing the relative errors among nearby events (for which the arrival time perturbations are correlated) but typically do not significantly improve absolute location accuracy (which requires knowledge of the true three-dimensional velocity structure).

Improvements in relative location accuracy obtained using these methods often produce a dramatic sharpening of seismicity patterns, particularly when more accurate timing is obtained using waveform cross-correlation (e.g., Rubin *et al.*, 1999; Waldhauser *et al.*, 1999; Waldhauser and Ellsworth, 2000; Shearer, 2002). Evaluating the performance of these methods is complicated, however, by the fact that the true earthquake locations are unknown. Here we generate synthetic data sets to compare four different relative earthquake location techniques: (1) the hypocentroidal decomposition method of Jordan and Sverdrup (1981), (2) the station term method (e.g., Frohlich, 1979), (3) the source-specific station term method (SSST) of Richards-Dinger and Shearer (2000), and (4) the modified double-difference method (DD) of Waldhauser and Ellsworth (2000). We also introduce a variation on the SSST method, which we term “shrinking box” SSST, that has some advantages over the conventional SSST method.

Our comparisons in this study are restricted to arrival time data alone, i.e., we do not consider waveform cross-correlation constraints. Our numerical experiments show that all of the methods give very close to the same result for the relative locations among nearby events, as should be expected from the theory underlying the methods. However, there are significant differences in the computational efficiency of the methods for large data sets and the shrinking box method appears to have a slight advantage over the simple SSST method in terms of absolute location accuracy.

2.2 Linearized Earthquake Location

Although the general earthquake location problem is nonlinear, the mathematics become much easier when we assume that perturbations to the locations are sufficiently small that a linear approximation is valid. In practical earthquake location algorithms this is typically achieved with an iterative approach, in which the location is assumed to be valid if the change in the location is very small at the final iteration.

In this section, we review some earthquake location techniques following the notation by Wolfe (2002). We begin with an introduction to the multiple-event location problem. Multiple-event location procedures are founded on the observation that the bias contaminating travel times from a set of nearby earthquakes tends to be strongly correlated; in particular, the error introduced by incorrect assumptions regarding Earth structure has a nearly constant value for arrival times measured at the same station (see Figure 2.1a). Since path bias of this type dominates the sample standard deviations computed for single-event locations (e.g., Freedman, 1967), the relative locations of events within a seismic cluster can be improved by taking these correlations into account.

Suppose we have a set of $p = 1, 2, ..., P$ earthquakes, with each earthquake constrained by N_p arrival-time observations. For simplicity we describe the situation in which P-wave phases alone are used and the data are weighted equally, but the methods can be generalized to cases where S or other phases are also included and the arrival times are assigned different weights. Given an initial location estimate $\mathbf{x}_{p0}$ for an earthquake p, a linearized estimate for how the arrival time residuals respond to small changes in the location may be written

$$\mathbf{A}_p \, \mathbf{\Delta x}_p + \mathbf{s}_p = \mathbf{\Delta t}_p \tag{2.1}$$

where $\mathbf{\Delta t}_p$ is a N_p-component vector containing the arrival time residuals, $\mathbf{A}_p$ defines the matrix of size

$N_p{\times}4$ containing the partial derivatives, calculated at the initial estimate $\mathbf{x}_{p0}$, $\mathbf{\Delta x}_p$ are the changes in earthquake hypocentral parameters ($4{\times}1$) which we wish to determine (typically these are dx, dy, dz, dt),

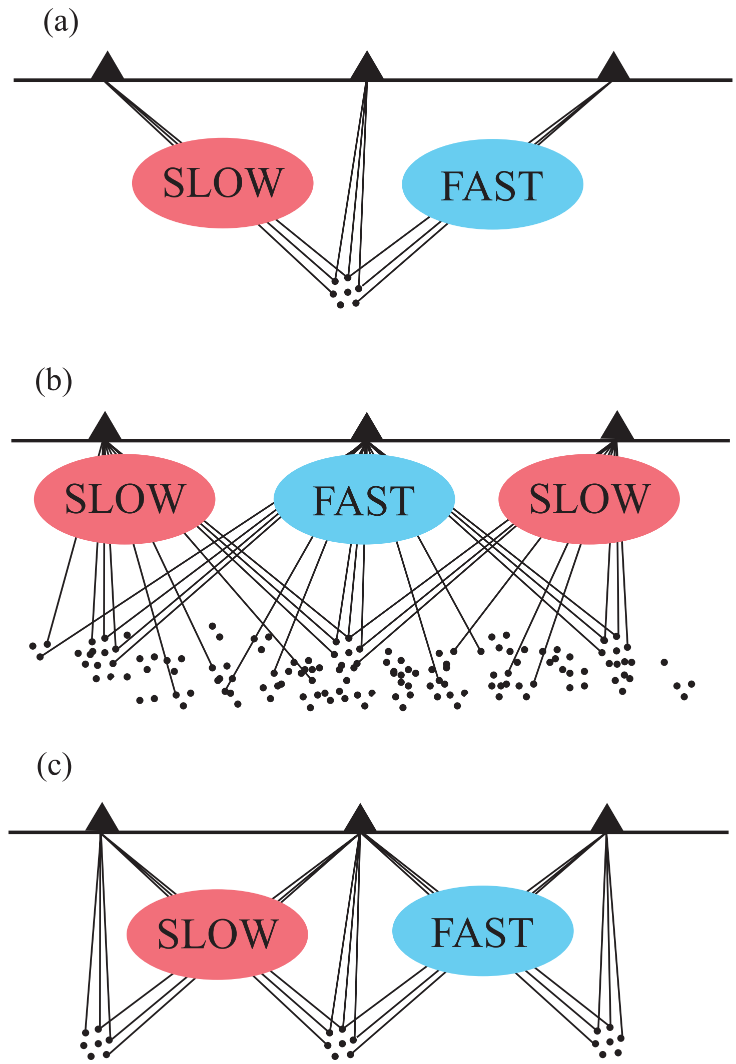

Figure 2.1. Cartoons illustrating how travel times and station terms are affected by three-dimensional velocity structure and different source-receiver geometries. (a) A compact cluster of events. The ray paths to each station pass through approximately the same velocity structure. In this case, a single travel-time correction term at each station (static station terms) can account for the biasing effects of the three-dimensional structure. (b) Distributed seismicity. Static station terms cannot fully account for general 3-D structure. They may, however, provide an estimate of the biasing effect of the shallow velocity anomalies below each of the stations. This can lead to some improvement in the locations, particularly when the 3-D variations at depth are small compared to the near-surface variations. (c) Distributed seismicity in general 3-D structure. The travel-time corrections to each station vary as a function of source position but are highly correlated among nearby events. Methods such as source-specific station terms (SSST) and double-difference (DD) can be used to improve locations in this case.

and $\mathbf{s}_p$ is a N_p-component vector of the path anomalies due to velocity heterogeneity along each of the source-receiver ray paths. The new locations will be updated as $\mathbf{x}_p = \mathbf{x}_{p0} + \mathbf{\Delta x}_p$. When equation (2.1) is applied to locate a single earthquake, $\mathbf{s}_p$ is either set to zero or to predetermined values. We will term this approach "single-event location," meaning that no information is used from any other events.

In most cases we compute the partial derivatives with respect to a one-dimensional reference seismic velocity model, although this is not required by the method. The path correction terms $\mathbf{s}_p$ then represent the biasing effects of the unmodeled three-dimensional structure or other errors in the velocity model.

Considering all P earthquakes as one linearized system, we may combine the individual single event location equations (2.1) into

$$\mathbf{A}\,\mathbf{\Delta X} + \mathbf{S} = \mathbf{\Delta T} \tag{2.2}$$

in which the locations are updated as $\mathbf{X} = \mathbf{X}_0 + \mathbf{\Delta X}$. In this case, we define M_{T} as the total number of unknown location parameters ($4P$) and N_{T} as the total number of arrival time observations. $\mathbf{\Delta X}$ is an $M_T \times 1$ vector in which the individual $\mathbf{\Delta x}_p$ vectors are strung end-to-end, and $\mathbf{S}$ and $\mathbf{\Delta T}$ are $N_T \times 1$ vectors with $\mathbf{s}_p$ and $\mathbf{\Delta t}_p$ strung end-to-end, respectively. $\mathbf{A}$ is an $N_T \times M_T$ matrix, containing the individual partial derivative $\mathbf{A}_p$ matrices along its diagonal, i.e.,

$$\begin{bmatrix} \mathbf{A}_1 & \mathbf{0} & . & \mathbf{0} \\ \mathbf{0} & \mathbf{A}_2 & . & \mathbf{0} \\ . & . & & . \\ . & . & & . \\ \mathbf{0} & . & . & \mathbf{A}_P \end{bmatrix} \begin{bmatrix} \mathbf{\Delta x}_1 \\ \mathbf{\Delta x}_2 \\ . \\ \mathbf{\Delta x}_P \end{bmatrix} + \begin{bmatrix} \mathbf{s}_1 \\ \mathbf{s}_2 \\ . \\ . \\ \mathbf{s}_P \end{bmatrix} = \begin{bmatrix} \mathbf{\Delta t}_1 \\ \mathbf{\Delta t}_2 \\ . \\ . \\ \mathbf{\Delta t}_P \end{bmatrix}$$

As written, this equation permits the trivial solution $\mathbf{\Delta X} = \mathbf{0}$ and $\mathbf{S} = \mathbf{\Delta T}$, in which the individual path anomaly correction terms are set to the travel time residuals for each source-receiver ray path. Meaningful solutions are only possible if we apply constraints to the correction terms to reduce the number of free parameters. These constraints typically assume that the correction terms are correlated for nearby ray paths. The simplest form of these constraints is to assume that the earthquakes are in a compact enough cluster that the path anomaly to each seismic station is constant.

In this case if K_T is the number of stations providing observations for the set of events, then the full correction terms vector $\mathbf{S}$ can be expressed as

$$\mathbf{S} = \mathbf{B}\mathbf{s} \tag{2.3}$$

where $\mathbf{s}$ is a $K_T \times 1$ vector that contains the terms at each station and $\mathbf{B}$ is the $N_T \times K_T$ matrix that assigns one of these K_T terms to each of the N_T travel time residuals:

$$\mathbf{B}_{ij} = \begin{cases} 1 & \text{when } \boldsymbol{\Delta}\mathbf{T}_i \text{ is from station } j \\ 0 & \text{otherwise} \end{cases} \tag{2.4}$$

and (2.2) becomes

$$\mathbf{A}\,\boldsymbol{\Delta}\mathbf{X} + \mathbf{B}\mathbf{s} = \boldsymbol{\Delta}\mathbf{T} \tag{2.5}$$

We will term the $\mathbf{s}$ values the "static" station terms to indicate that they have fixed values for each station regardless of the event location. In contrast, the "source-specific" station terms (SSST) that we will later consider have different values for different source locations. It is important to note at this point that (2.5) does not have a unique least squares solution for $\boldsymbol{\Delta}\mathbf{X}$ and $\mathbf{s}$ because their projections onto the data space are not linearly independent. The most obvious nonuniqueness is the tradeoff between the event origin time part of $\boldsymbol{\Delta}\mathbf{X}$ and the station terms; any constant time could be added to one and subtracted from the other. This ambiguity can be removed fairly easily by imposing additional constraints on $\mathbf{s}$, for example, by forcing the mean station term to zero.

However, there are also tradeoffs between the x, y, z locations of the events and the values of $\mathbf{s}$. For example, north-south shifts in the absolute event locations can be accommodated by adding times to station terms to the north of the event cluster and subtracting times from the station terms to the south. This tradeoff between the station terms and the locations is complete if the partial derivatives are identical for all of the events (i.e., the same reference location $\mathbf{x}_{p0}$ is used) (Jordan and Sverdrup, 1981; Pavlis and

Hokanson, 1985). In this case the absolute location of the event cluster is unconstrained, provided no additional constraints are imposed on $\mathbf{s}$. When the partial derivative matrices differ among the events, in principle this tradeoff is broken and absolute location information can be obtained. However, in practice the system remains very ill-conditioned and absolute locations are not significantly constrained until the event separation becomes quite large (at which point the static station term approximation is probably no longer valid because the path anomalies to each station will vary between events).

The improvement in location accuracy obtained by using (2.5) is found in the relative locations among the events in the cluster. One might ask why this is achieved given that the path anomalies are the same for all of the events and could be expected to have a similar biasing effect on all of the event locations. The improvement occurs largely because of the fact that arrival times for the events are not always recorded by the same set of stations and thus are biased by the path anomalies by differing amounts. In addition, least squares solutions will tend to weight the largest residuals the most and thus the solutions may be dominated by the small set of stations with the largest station terms.

In the following sections, we will show how different techniques improve relative locations.

2.2.1 Hypocentroidal Decomposition (JS)

This method was introduced by Jordan and Sverdrup (1981) (hereinafter referred to as JS) and involves projecting out the part of the problem that is sensitive to the static station terms. In this case we define the $N_T \times N_T$ projection operator $\mathbf{Q_{JS}}$:

$$\mathbf{Q_{JS}} \equiv \mathbf{I}^{N_T} - \mathbf{B}\mathbf{B}^{\dagger} \tag{2.6}$$

where $\mathbf{B}^{\dagger}$ is the generalized inverse of $\mathbf{B}$ calculated by singular value decomposition (SVD).

Define w_k to be the number of earthquakes recorded by station k and $\mathrm{w}_{k(i)}$ to be the number of earthquakes recorded by the station recording $[\mathbf{\Delta T}]_i$. Then

$$[\mathbf{Q_{JS}}]_{ij} = \delta_{ij} - \frac{1}{\mathrm{w}_{k(i)}}\Delta_{ij} \tag{2.7}$$

where δ_{ij} is the Kronecker delta function and $\mathbf{\Delta}_{ij} = 1$ if $[\mathbf{\Delta T}]_i$ and $[\mathbf{\Delta T}]_j$ are from same station, and zero otherwise.

$\mathbf{Q_{JS}}$ transforms $\mathbf{\Delta T}$ into $\mathbf{\Delta T}$ minus the travel time residual averages at each station. In the static station term case, all of the terms are equal to these averages, and thus $\mathbf{Q_{JS}B} = \mathbf{0}$ and (2.5) becomes

$$\mathbf{Q_{JS}A}\,\mathbf{\Delta X} = \mathbf{Q_{JS}\Delta T} \tag{2.8}$$

The least squares solution to this equation can be obtained as

$$\mathbf{\Delta X} = (\mathbf{Q_{JS}A})^{\dagger}\,\mathbf{Q_{JS}\Delta T} \tag{2.9}$$

Thus the new locations can be obtained without solving explicitly for the station terms. Note that stations that only record one earthquake will not contribute to this solution because the average residual in this case will always equal the residual itself; these stations can simply be deleted from the system prior to any calculation.

Further insight into this method may be obtained by decomposing the set of location perturbations $\{\mathbf{\Delta x}_p; p = 1, 2, \cdots, P\}$ into two parts:

$$\mathbf{\Delta x}_p = \mathbf{\Delta x}_0 + \delta\mathbf{x}_p \tag{2.10}$$

where

$$\mathbf{\Delta x}_0 \equiv P^{-1}\sum_{p=1}^{P}\mathbf{\Delta x}_p \tag{2.11}$$

and

$$\sum_{p=1}^{P}\delta\mathbf{x}_p = 0 \tag{2.12}$$

$\mathbf{x}_0 + \mathbf{\Delta x}_0$ is called the *hypocentroid*, the average absolute location of the earthquakes, and the $\{\delta\mathbf{x}_p\}$ are called the *cluster vectors*, which only define the relative locations of the earthquakes, of the event group. Consequently,

$$\mathbf{\Delta X} = \mathbf{\Delta X}_0 + \delta\mathbf{X} \tag{2.13}$$

The method of Jordan and Sverdrup (1981) was developed to study groups of shallow teleseismic earthquakes over limited regions. In this situation, the partial derivatives do not vary much with earthquake location, so in the Jordan and Sverdrup method, the partial derivatives in $\mathbf{A}$ for all earthquakes are set to an identical reference point. In this special case, it can be proved that $\mathbf{Q_{JS}}\mathbf{A}\boldsymbol{\Delta}\mathbf{X}_0 = \mathbf{0}$ (Wolfe, 2002), so that only improved relative locations can be obtained. In practice, events within a cluster are located first using single event location. The mean cluster location is then fixed as the reference location (the hypocentroid) for the cluster and the method solves for the perturbations to this location. For clusters with large numbers of events, considerable computation will be involved in the singular value decomposition of the $N_T \times M_T$ matrix $\mathbf{Q_{JS}}\mathbf{A}\,\boldsymbol{\Delta}\mathbf{X}$. In these cases, we have found that iterative matrix inversion techniques such as the conjugate gradient method are effective in speeding the calculations.

2.2.2 Static Station Terms (ST)

One of the simplest and most widely applied relative location approaches is the station term method, which solves iteratively for a custom set of station-timing corrections (e.g., Frohlich, 1979; see also Pujol, 1988). Equation (2.5), $\mathbf{A}\,\boldsymbol{\Delta}\mathbf{X} + \mathbf{B}\mathbf{s} = \boldsymbol{\Delta}\mathbf{T}$, can be written

$$\begin{bmatrix} \mathbf{A}_1 & \mathbf{0} & . & \mathbf{0} \\ \mathbf{0} & \mathbf{A}_2 & . & \mathbf{0} \\ . & . & & . \\ . & . & & . \\ \mathbf{0} & . & . & \mathbf{A}_P \end{bmatrix} \begin{bmatrix} \boldsymbol{\Delta}\mathbf{x}_1 \\ \boldsymbol{\Delta}\mathbf{x}_2 \\ . \\ \boldsymbol{\Delta}\mathbf{x}_P \end{bmatrix} + \begin{bmatrix} 0 & 1 & . & 0 \\ 0 & 0 & . & 1 \\ & . & . & . \\ & . & . & . \\ 1 & 0 & . & 0 \end{bmatrix} \begin{bmatrix} \mathbf{s}_1 \\ \mathbf{s}_2 \\ . \\ \mathbf{s}_P \end{bmatrix} = \begin{bmatrix} \boldsymbol{\Delta}\mathbf{t}_1 \\ \boldsymbol{\Delta}\mathbf{t}_2 \\ . \\ . \\ \boldsymbol{\Delta}\mathbf{t}_P \end{bmatrix} \tag{2.14}$$

This is a coupled set of equations for the location parameters, $\boldsymbol{\Delta}\mathbf{X}$, and the station terms, $\mathbf{s}$. We solve this iteratively by alternatively solving for each vector, while leaving the other vector fixed. In the first step the station corrections are held fixed (either set to zero or to values obtained elsewhere) and we solve for $\mathbf{\Delta X}$ using

$$\mathbf{A}\,\mathbf{\Delta X} = \mathbf{\Delta T} - \mathbf{Bs} \tag{2.15}$$

The events are located with respect to a corrected set of arrival times. Because there is no coupling between the event locations at this step, each event can be located separately from the other events. Next, we solve for a new set of station terms using

$$\mathbf{Bs} = \mathbf{\Delta T} - \mathbf{A}\,\mathbf{\Delta X} \tag{2.16}$$

Notice that the right hand side is simply the arrival time residuals; the least squares solution for $\mathbf{s}$ will set each station term to the mean residual of all of the events for the station. The process is then repeated until a stable set of locations and station terms is obtained. In Appendix A., we demonstrate that this algorithm should converge. In practice, we have found in most cases that convergence is rapid and that no more than 5 to 10 iterations are necessary.

The method is much faster than hypocentroidal decomposition because there is no need to use the full $\mathbf{A}$ matrix in the calculations. The approach is also quite flexible because the station term calculation is performed separately from the event location calculation, so that any desired location method can be used, including standard or preexisting algorithms. However, the nonuniqueness inherent in these equations between the mean cluster location and the station terms still exists. In practice, the mean cluster location is largely determined at the first iteration for the event locations.

Finally, we note that the static station term method can be applied even when the events are not in a compact cluster (Figure 2.1b). In this case, the station terms will only be weakly correlated among different events at the same station because the source-receiver ray paths will sample different parts of the three-dimensional velocity structure. However, the method may nonetheless yield some improvement in location accuracy because differences in the shallow velocity structure beneath each station will be accounted for by the station terms. In this case, more accurate absolute event locations are possible, depending upon the details of the three-dimensional velocity structure that is biasing the times, azimuthal coverage and relative sizes of the velocity perturbations.

2.2.3 Source-Specific Station Terms (SSST)

Static station terms work best when the differences between the actual travel times in the Earth and those in the assumed velocity model to each station are the same for all events. When the seismicity covers a large region containing significant lateral velocity heterogeneity (e.g., Figure 2.1c), neither the hypocentroidal decomposition method nor the static station term method is likely to work very well. In this case, a generalization of the station term approach, termed the source-specific station term (SSST) method by Richards-Dinger and Shearer (2000) can be applied. In this method, the location and station term calculations are again performed alternatively and the solution is obtained iteratively, but the station terms no longer consist of a single value at each station; rather, each station will have a station correction function which will vary as a function of source position.

For static station terms, we simply calculate the station term for each station as the mean of the residuals at that station from all events. For source-specific station terms (SSSTs), we calculate a separate correction for each source-receiver pair at the given station using the residuals from nearby events. In this case, there is a different value of the station term vector $\mathbf{S}$ for every value of the residual vector $\mathbf{\Delta T}$; these values are a smoothed version of the event-specific residual field for each station. This smoothing over adjacent events can be done in a number of different ways. Richards-Dinger and Shearer (2000) smoothed over a fixed number of neighboring events using a natural neighbor tesselation.

Here we will implement the SSST approach by selecting the nearby events that are located within a sphere of specified radius $r_{\max}$ around the target event. The station term for the target event is then computed as the mean residual of these events. Note that different results will be obtained depending upon the size of the cutoff distance. If $r_{\max}$ is set to a large enough distance, then the SSST method will give the same result as the static station term method. However, if $r_{\max}$ is set to a very small distance, the number of events may not be sufficient to obtain a reliable estimate of the true station term. Thus selection of the cutoff distance is a key factor in application of the SSST method.

The SSST method shares some of the advantages of the static station term technique. The event location part of the calculation is separate from the station term calculation and can be performed quickly using any desired single-event location method. Computing the station terms at each iteration is also a simple calculation; the most numerically taxing part of this is identifying the events within the cutoff radius for each target event. In practice, convergence to a stable set of locations and station terms requires only a few iterations (although we have not derived a formal proof of convergence for the SSST algorithm). Note that in theory, the ST and SSST methods should yield the same locations for a single compact cluster that is smaller than the applied SSST cutoff distance $r_{\max}$.

When Richards-Dinger and Shearer (2000) applied the SSST method to locate southern California earthquakes, they obtained their initial locations using the static station term method, and then used these station terms as a starting point for the SSST calculation. In this way, they achieved some improvement in the absolute locations of the events before focusing on the relative locations among closely spaced events. A generalization of this approach is to continuously shrink the SSST cutoff distance $r_{\max}$ between the first and final iteration. In other words, we start the cutoff distance with a large value to include all the events from which we calculate station terms, then decrease it to some specified minimum distance to calculate station terms using only the closest events. We will show later that this method seems to give the best results on our synthetic data sets.

2.2.4 Double-Difference (DD)

The double-difference location algorithm (Waldhauser and Ellsworth, 2000, 2002) allows the simultaneous relocation of distributed events by minimizing residual differences for pairs of earthquakes without explicitly solving for station corrections.

The single-event location problem for the kth observation of earthquake i can be written as

$$\frac{\partial t_k^i}{\partial \mathbf{x}} \boldsymbol{\Delta}\mathbf{x}^i + s_k^i = \Delta t_k^i \tag{2.17}$$

where s_k^i is the path anomaly correction between event i and station k. Thus we can express the time difference between the residuals at the same station for two events i and j as

$$\frac{\partial t_k^i}{\partial \mathbf{x}} \mathbf{\Delta x}^i + s_k^i - \frac{\partial t_k^j}{\partial \mathbf{x}} \mathbf{\Delta x}^j - s_k^j = dr_k^{ij} \tag{2.18}$$

where dr_k^{ij} is the residual between observed and calculated differential travel times between these two events, i.e.,

$$dr_k^{ij} = (t_k^i - t_k^j)^{obs} - (t_k^i - t_k^j)^{cal} \tag{2.19}$$

If the events are close to each other, then their path corrections are likely to be similar, and so making the approximation $\mathbf{s}_k^i = \mathbf{s}_k^j$, the path anomalies cancel and we have simply

$$\frac{\partial t_k^i}{\partial \mathbf{x}} \mathbf{\Delta x}^i - \frac{\partial t_k^j}{\partial \mathbf{x}} \mathbf{\Delta x}^j = dr_k^{ij} \tag{2.20}$$

After combining these equations from all event pairs for a station, and for all stations, we obtain a system of linear equations of the form

$$\mathbf{G \Delta X} = \mathbf{d} \tag{2.21}$$

where $\mathbf{G}$ defines a matrix of size $M_{\mathrm{DD}} \times M_{\mathrm{T}}$ (M_{DD} is the number of double-difference observations) containing partial derivatives, $\mathbf{\Delta X}$ is a vector containing the changes in hypocentral parameters that we wish to determine, and $\mathbf{d}$ is the data vector containing the double-difference times.

Equivalently, this can be written as

$$\mathbf{Q_{DD} A \Delta X} = \mathbf{Q_{DD} \Delta T} \tag{2.22}$$

where

$$\mathbf{Q_{DD} A} = \mathbf{G} \tag{2.23}$$

and

$$\mathbf{Q_{DD} \Delta T} = \mathbf{d} \tag{2.24}$$

$\mathbf{Q_{DD}}$ is the double-difference operator combining differences of earthquake arrival times recorded at a given station k, $\Delta t_k^i - \Delta t_k^j$ (for $i \neq j$ and $i < j$), and has the form:

$$\begin{bmatrix} 1 & . & . & -1 & . & . & . & . & 0 \\ 1 & . & . & . & . & . & -1 & . & . \\ . & . & . & . & . & . & . & . & . \\ 0 & . & . & . & . & 1 & . & . & -1 \end{bmatrix} \tag{2.25}$$

with each row containing only two nonzero terms, 1 and -1.

The double-difference approach permits different types of differential arrival time data and choices in terms of selection and weighting of these data. One of the advantages of DD is that it is easy to incorporate dt results obtained from waveform cross correlation. DD can also be applied to phase data alone by selecting dt pairs from the individual arrival time picks. For small data sets consisting of a single isolated cluster it is practical to use all available event pairs. For large numbers of events or distributed seismicity, it makes sense to restrict the event pairs to those within some specified maximum separation distance. The algorithm released by Waldhauser (2001) allows the user to select this separation distance, as well as weight the differential times by distance and include absolute arrival time data if desired.

To facilitate comparisons with the other methods, we wrote our own version of the double-difference algorithm. We do not use damping in any of the methods we test. Since the distance weighting of Waldhauser and Ellsworth should only work when damping is employed (Wolfe, 2002), we do not apply distance weighting in our location tests. We do, however, include an event separation distance cutoff. Thus, $\mathbf{Q_{DD}}$ does not combine all possible differences of arrival times recorded by the same station, instead, we only consider the events in a sphere centered on the targeted event with the radius set to the cutoff distance, as discussed previously for the SSST algorithm. Our DD method uses only these differential times to refine the locations; the absolute pick times are used to obtain the initial locations but are not used in the DD algorithm itself.

2.3 Synthetic Data Tests

We perform all our synthetic tests in a $64 \times 64 \times 32$ km uniform half-space with a P wave velocity of 6 km/s and a P-to-S velocity ratio of 1.73. We generate 20 random station locations on the surface of the half-space and a set of specified earthquake locations. Although more realistic structures with slower near-surface velocities may result in downgoing ray paths from the source, our model provides reasonably approximate ray paths for the $9-11$ km deep events that we model. To simulate the irregular pick availability of real earthquake data, for each event we generate P picks with 0.67 probability and S picks with 0.5 probability. Thus each synthetic event is recorded by a different set of stations with an average of 13 P picks and 10 S picks per event.

The linear location system is solved by minimizing the L2 norm of the travel time residuals using a conjugate gradient algorithm. We compute 100 conjugate gradient iterations, although in most cases the solution converges much more quickly, depending on the data set and the starting conditions. For the SSST method, we used 100 conjugate gradient iterations at each location step, and found that 5 to 10 iterations for the station term calculation was sufficient. We begin all of the methods with linearized single event location to obtain a set of starting locations that are typically shifted somewhat from the true locations, depending upon the perturbations applied to the travel time picks. We will consider two forms of errors in the locations. Absolute location error is the difference between the computed location and the true location. Relative error is the difference between the computed and actual relative locations of two nearby events. Thus the concept of relative location error only makes sense for nearby events.

We start our relocation with single event location, for which the starting locations are some random locations shifted from the true locations. Then the new locations from the single event location method are input as the starting locations for the three targeted techniques. The hypocentroidal decomposition method does not improve the mean location of the whole cluster, but the relocations significantly depend on the starting locations. We choose the mean location of the starting cluster as the common reference point and the partial derivatives are fixed to this point. We constrain both JS and DD methods to have no mean location shift relative to this reference point during relocation because we found that even a small amount of random picking error can produce unstable results for the DD algorithm if this constraint is not applied. It is likely that this constraint would be unnecessary if we used absolute pick times as well as relative times in our implementation of the DD method.

2.3.1 Single Isolated Cluster Tests

In principle, all of the location techniques should yield similar relative locations for a compact event cluster. Our first test is to locate 27 events in a compact $2 \times 2 \times 2\,\mathrm{km}$ cube with the center at 10 km depth. We apply a cutoff distance for the DD and SSST algorithms that is large enough to cover all the events in the cube; in this case the static station term and SSST methods are equivalent. Figure 2.2 shows the distributions of the stations and events from one random realization of the station positions.

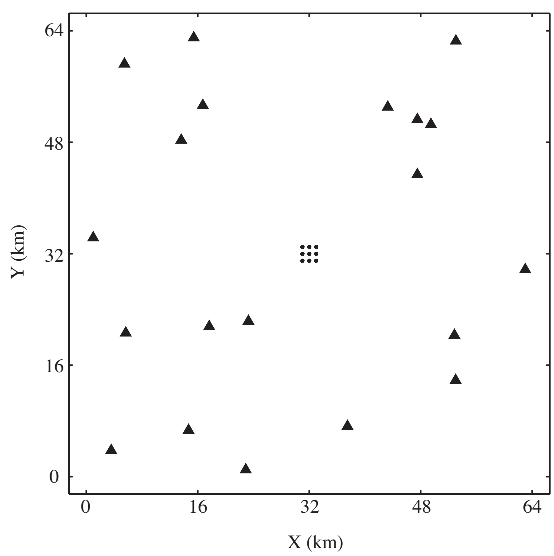

Figure 2.2. Map view of 20 random station locations (triangles) and 27 specified true event locations (dots) in a 2×2×2 km grid at 10 km depth (each dot represents locations at 9, 10 and 11 km depth).

We add two types of noise to the theoretical travel times: (1) Gaussian distributed station terms with zero mean and 0.3 s standard deviation (SD) for P picks (scaled by 1.73 for S picks), which are constants for all events recorded by a given station; (2) Gaussian distributed random picking errors with zero mean and 0.01 s standard deviation for P picks and 0.02 s for S picks. Random picking errors introduce location errors that cannot be improved with any of the methods discussed here. Since the focus of our study is on the relative location improvement that can be achieved by accounting for the station terms, we assign small values to the random pick errors in order to enhance the improvements that we will achieve. However, it is important to include at least some random picking error because otherwise the algorithms might achieve improvements in absolute location accuracy that are unlikely to be obtained with real data.

Figure 2.3 shows the location results of one random realization of our synthetic data. As we expect, the single event location method produces quite large errors in both absolute and relative locations. These locations are equivalent to the standard (catalog) locations for real data. The shift in the mean cluster location (which dominates the absolute location errors for the JS, DD and SSST methods), results from the random station terms and the finite number of stations. The size and direction of this shift vary among the different random realizations of the synthetic data. The location map views and cross sections for this example clearly indicate that all three techniques, JS, DD and SSST, yield similar improvements in relative location accuracy. Furthermore, JS and DD provide almost the same absolute locations, while SSST relocations are a little different from those of JS and DD. This is mainly due to the constraint on the JS and DD methods that the mean location shift is zero during relocation.

We note that in principle, this constraint on the mean location shift is not required for the JS and DD methods and it might be possible in some circumstances to improve the absolute location accuracy by relaxing this requirement. In practice, however, we found that if even a very small amount of random picking error is present in the synthetic data, the absolute locations for the DD method sometimes become very unstable and unreliable unless the zero mean location shift constraint is applied.

We estimate the relocation errors from 60 random realizations of the synthetic data. In Table 2.1, we show the root-mean-squares (RMS) of both absolute and relative location errors. The relative location errors are calculated for each event relative to all the other events in the cube. As expected, all three methods (JS, DD and SSST) show improvement in location accuracy compared to the single event locations. Although some improvement is achieved in the absolute location accuracy (by reducing the scatter in the locations, not from any significant shift in the mean cluster location), the most dramatic improvement is in the relative location accuracy, where the relative errors in horizontal position are reduced from 1.1 km

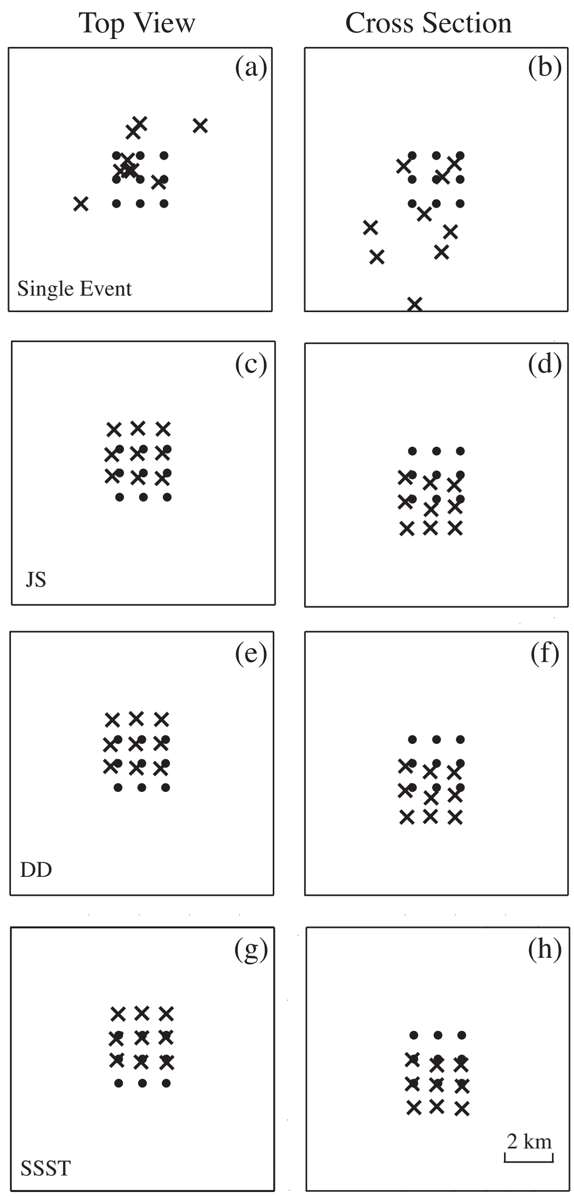

Figure 2.3. Comparison of different location methods for a single compact cluster of 27 events from one random realization. Dots are true locations and crosses are computed locations. (a) Single event location top view. (b) Single event location cross section. (c) JS location top view. (d) JS location cross section. (e) DD location top view. (f) DD location cross section. (g) SSST location top view. (h) SSST location cross section. In each case, the middle (middle layer for top view and middle standing surface for cross section) nine events are shown, not the full 27.

to about 70 m. As is typically the case with real data, the horizontal location accuracy is much better than the vertical location accuracy.

Table 2.1. Single cluster location results comparison. We show absolute and relative location RMS errors from 60 random realizations. For a given event, the relative locations are with respect to all the other events in the cluster. ([a]No mean location shift during relocation.)

	RMS of Absolute Error		RMS of Relative Error	
Method	Horizontal, km	Vertical, km	Horizontal, km	Vertical, km
Single Event	1.55	2.26	1.14	2.41
JS[a]	1.10	1.54	0.07	0.34
DD[a]	1.10	1.54	0.07	0.34
SSST	0.91	1.69	0.06	0.36

2.3.2 Three-Dimensional Velocity Model Tests

It is not surprising that all three techniques provide similar improvements in relative location accuracy for a compact cluster. The advantage of the SSST and DD methods is that they can also be applied to distributed seismicity. In this case, the events are far enough apart that the travel time perturbations cannot be assumed constant for each station. To generate realistic synthetic data for distributed events, we compute travel-time differences resulting from an isotropic three-dimensional velocity model with random P velocity variations of 0.3 km/s RMS using a $k^{-1.8}$ power law. S velocity variations are scaled as 3 times the P variations. We sum the travel-time anomalies along each source-station ray path to generate realistic spatial correlations in the travel-time anomalies. We sum the anomalies along the straight-line ray paths that would exist in the unperturbed half space. The three-dimensional (3-D) ray tracing would be more realistic, but our approximate approach is probably adequate to generate spatially correlated station terms of sufficient accuracy to address the relative location problem that is the focus of this paper. Figure 2.4 is an example of the isotropic 3-D velocity model, and Figure 2.5 shows the resulting station term field for a specific station location.

As before, for each realization we generate 20 randomly located stations on the surface. We include 549 events in three layers of 183 events in the pattern shown in Figure 2.6. Events in each line of earth-

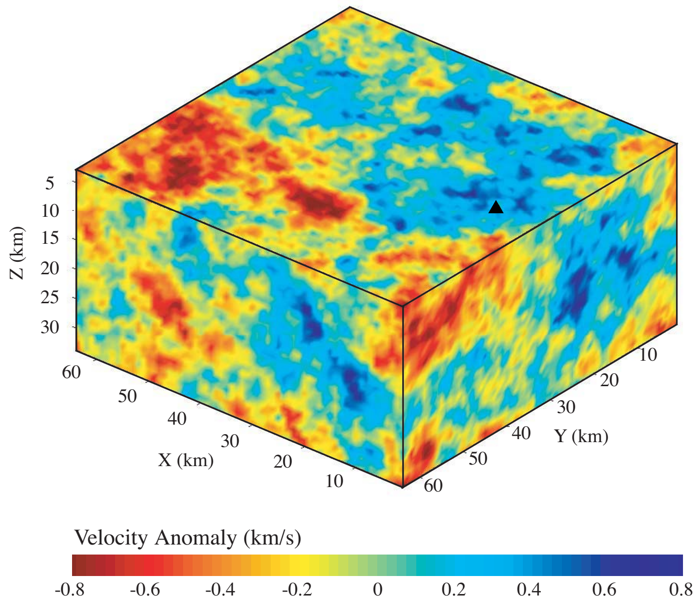

Figure 2.4. A random three-dimensional P velocity model relative to a constant velocity of 6 km/s, generated using a $k^{-1.8}$ power law.

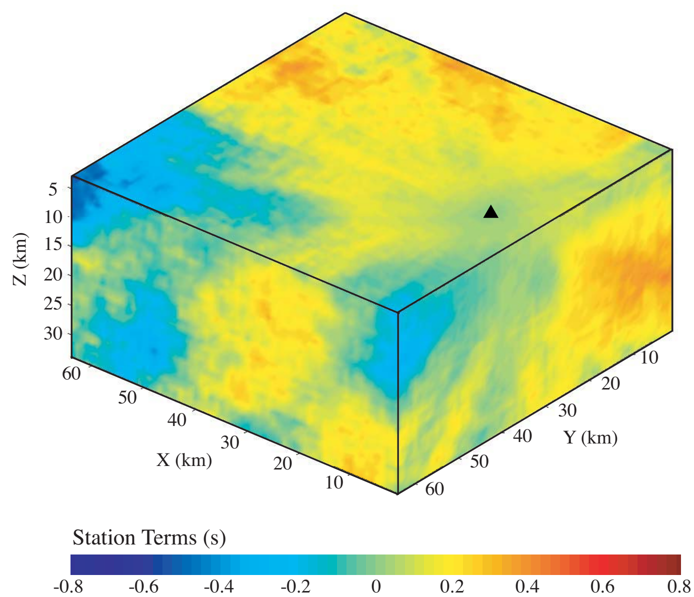

Figure 2.5. Source-specific station terms for the station shown as the triangle, corresponding to the random 3-D velocity model in Figure 2.4.

quakes are separated by 1 km. The three layers are located at depths of 9, 10 and 11 km. Picks for each event to each station are again generated with 0.67 probability for P and 0.5 probability for S. We apply a cutoff distance of 8 km for the DD and SSST methods. In most cases, this results in about 50 neighboring events in average for each target event in the calculations. For the shrinking box SSST method, we use a starting cutoff distance large enough to include all the events and then decrease the distance by a constant fractional change with each iteration to the final cutoff of 8 km.

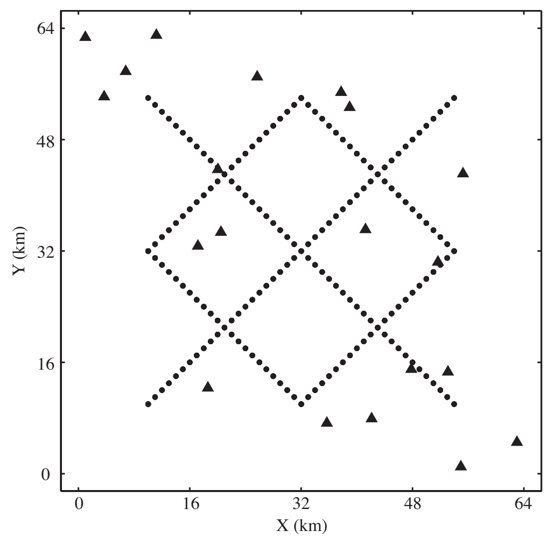

Figure 2.6. Earthquake locations and 20 random station locations for the distributed seismicity test of the location methods. Each dot represents earthquakes at 9, 10 and 11 km depth in this top view.

Figure 2.7 and Figure 2.8 are the map views and cross sections of the relocation results of one random realization of the station locations and the 3-D velocity model. Notice the scatter in the single event locations compared to those of the other three methods. The difference between absolute and relative location errors is apparent in these plots. The reduced scatter in the relative locations sharpens the alignment of the events in each line, but the lines are still displaced from their true locations.

Table 2.2 compares the location accuracy of the different methods, as measured by the RMS of absolute and relative location errors from 60 random realizations. The relative location errors are calculated for each event relative to a set of nearby events that are within a range of 2 km both in horizontal distance and in depth. As in the single event cluster test, the methods improve the absolute location accuracy only

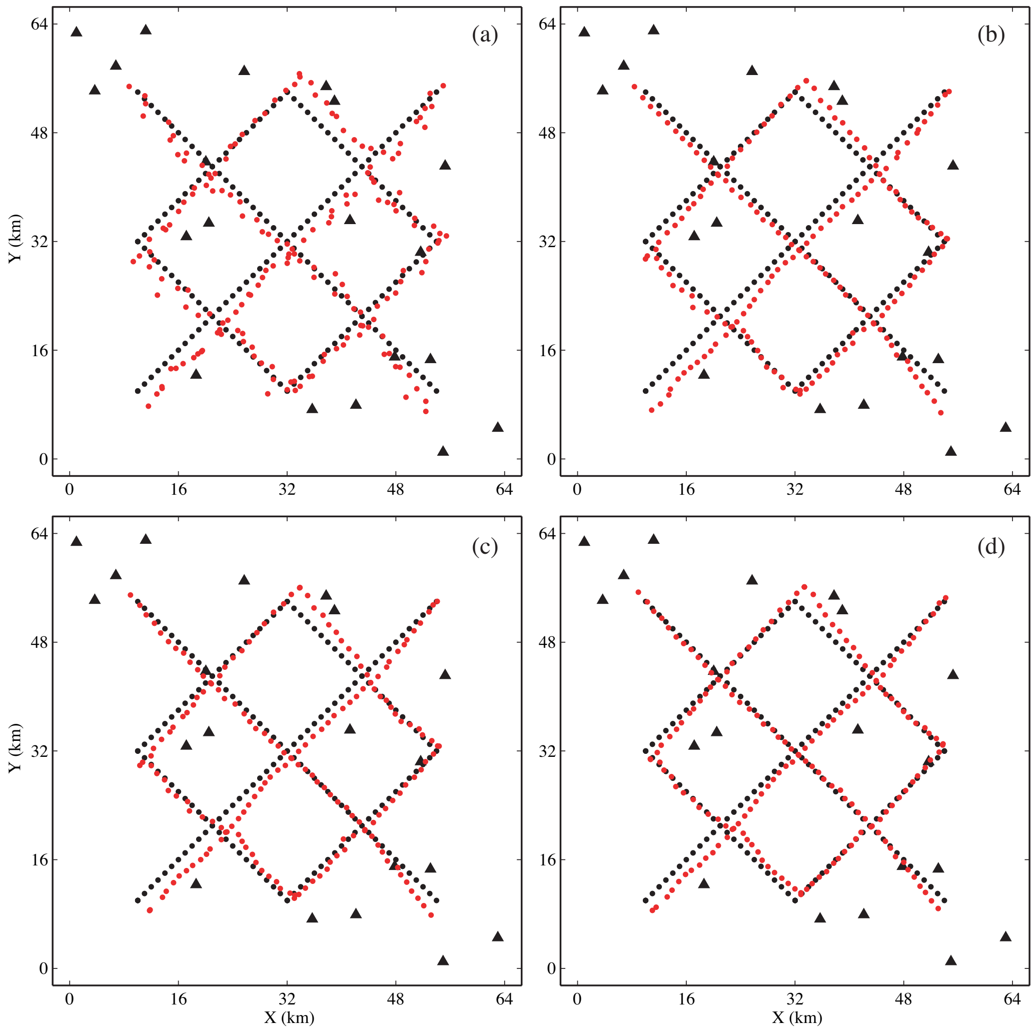

Figure 2.7. Comparison of different location methods for one random realization of the three-dimensional velocity structure shown in Figure 2.4. Black dots are true locations, and red dots are computed locations, and triangles are stations. (a) Single event location. (b) DD location. (c) SSST location. (d) Shrinking box SSST location. In each case, the middle 183 events are shown, not the full 549.

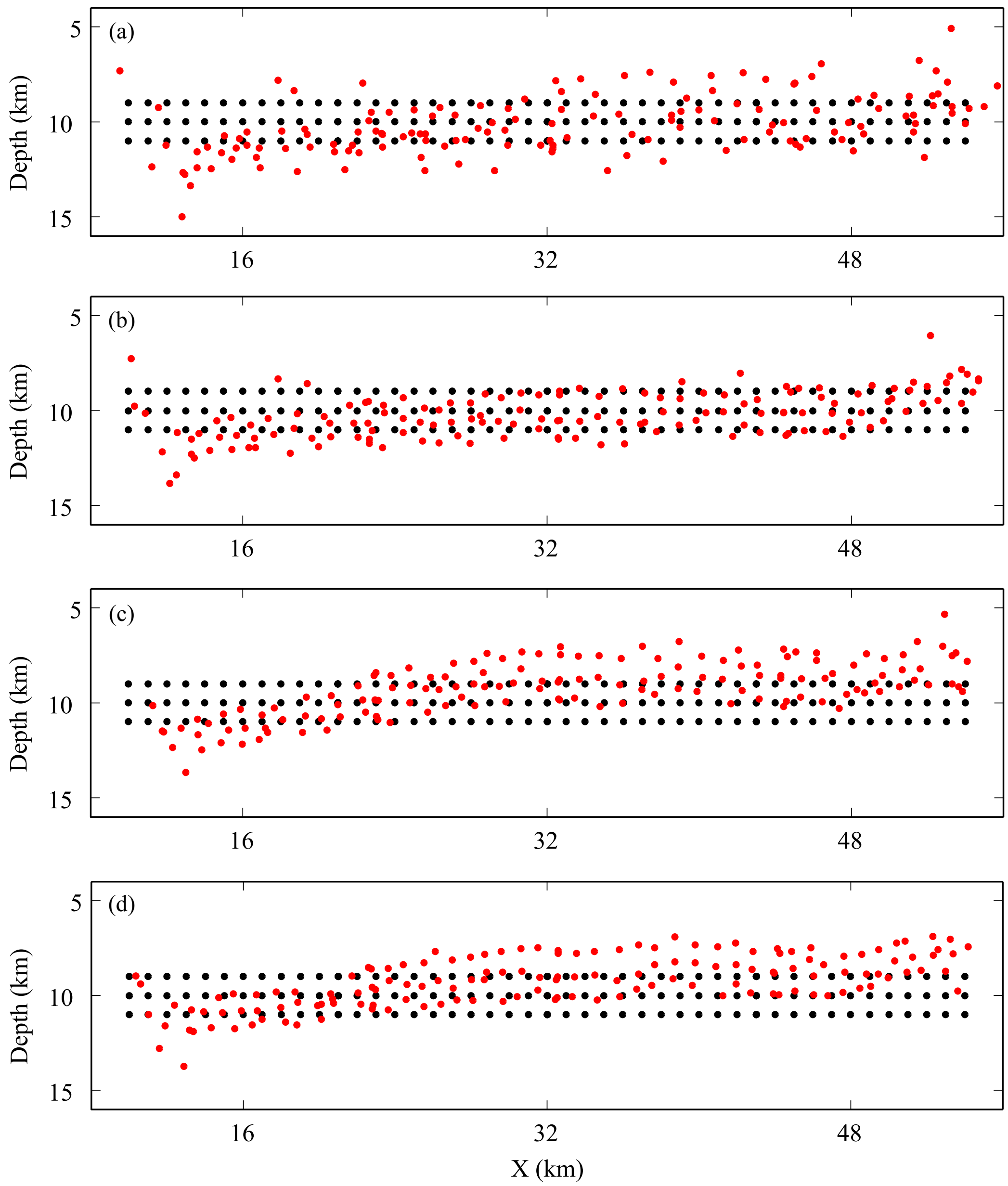

Figure 2.8. Cross-section comparison of different location methods for one random realization of the three-dimensional velocity structure shown in Figure 2.4. Black dots are true locations, and red dots are computed locations. (a) Single event location. (b) DD location. (c) SSST location. (d) Shrinking box SSST location. In each case, the diagonal 147 events are shown, not the full 549.

Table 2.2. A comparison of four location techniques applied to synthetic travel time data predicted by random 3-D velocity models. We show absolute and relative location RMS errors from 60 random realizations. For a given event, the relative locations are with respect to the events within 2 km. Also we give the computation time of each technique relative to the single event location. ([a]No mean location shift during relocation.)

	RMS of Absolute Error		RMS of Relative Error		
Method	Horizontal, km	Vertical, km	Horizontal, km	Vertical, km	Computation Time (Relative)
Single Event	2.10	2.28	0.70	0.95	1
DD[a]	1.73	2.09	0.29	0.47	126
SSST	1.67	1.90	0.30	0.49	5
Shrinking Box SSST	1.33	1.59	0.27	0.41	24

slightly but significantly improve the relative location accuracy. There are greater errors in the vertical direction than in the horizontal direction. Finally, the shrinking box SSST method produces a slight, but noticeable improvement in absolute location accuracy compared to the other methods. We do not completely understand why the shrinking box method provides this advantage; it seems to respond to some of the longer wavelength structure in the source-specific station term field that is not included in the DD or SSST methods when a fixed event separation distance is applied. We performed some experiments to see if methods that apply a distance weighting function to the SSST smoothing operator (i.e., weighting the nearby events more, the distant events less, with the weight a smooth function of distance rather than a simple cutoff at a fixed distance). However, we were not able to achieve results as good as the shrinking box method with this approach. We also performed some experiments in implementing the shrinking box approach to the DD method by reducing the range cutoff with increasing iteration number. We obtained some improvements in relative location accuracy, but the absolute locations were not as good as those given by the shrinking box SSST method.

Table 2.2 also lists a measure of the computation time for the different methods, relative to single event location. In our implementation, the SSST technique is significantly faster than the DD method. This is because the SSST event locations at each iteration are still performed separately, so the run time scales approximately as the number of iterations (the station term calculation at each iteration is very fast compared to the location part of the calculation). In contrast, in the DD approach the location of every event is linked to the locations of all of the other events. This significantly increases the computation time even when the conjugate gradient method is used to solve the linear system. However, these results should be considered approximate because run times often depend upon specific details of program construction.

Many networks do not produce as many S picks as we used in our synthetic experiments. To test the performance of the algorithms under these conditions, we also perform experiments using synthetic data that only contained P picks. Although the relocations are not as good as those obtained with both P and S picks, especially in depth, we still come to the same conclusion that DD and SSST produce quite similar relocation results and that the shrinking box SSST method is slightly better than the conventional

SSST.

2.4 Discussion

The advantage of our synthetic tests over real earthquake data sets is that the true event locations are known so that it is possible to directly measure the location errors. Although it is not possible to simulate every feature that may exist in real data, we have attempted to include the main factors that affect event locations, including random picking errors, incomplete and irregular pick distributions, station terms, and general three-dimensional velocity structure. We have focused on methods (JS, DD and SSST) that attempt to improve the relative location accuracy among nearby events by taking advantage of the correlated travel anomalies from these events to each station. Despite differences in how the methods work, they are all solving the same underlying problem. Indeed, it is possible to demonstrate that station term algorithms provide a least squares iterative solution to the same equations that are used in the JS and DD methods. Thus it is reassuring that all of the methods achieve comparable results when applied to identical synthetic data sets.

The DD and SSST methods can be used for large numbers of distributed earthquakes. An advantage of the DD algorithm is that a documented program has been released to the seismology community (Waldhauser, 2001). This code also can incorporate differential time measurements provided by waveform cross correlation, a feature that is not included in our study, which uses only arrival time picks. In principle, our synthetic tests could be adopted to include waveform cross-correlation data by including differential times of greater accuracy than the individual picks. This will be a goal of our future work, as well as experimenting with the effects of some of the adjustable parameters in the DD and SSST algorithms.

2.5 Acknowledgments

We thank George Backus and Bob Parker for advice regarding the convergence properties of the iterative solution discussed in Appendix A. Cecily Wolfe and an anonymous reviewer provided constructive comments. Funding for this research was provided by NEHRP/USGS grant 03HQPA0001. This research was also supported by the Southern California Earthquake Center, which is funded by NSF Cooperative Agreement EAR-0106924 and USGS Cooperative Agreement 02HQAG0008. This is SCEC contribution 782.

2.6 Appendix A. Convergence of Static Station Term Method

Here we demonstrate the convergence of the static station term method. Equation (2.5) gives the linearized location problem for a set of $p = 1, 2, \cdots, P$ earthquakes recorded by K_T stations:

$$\mathbf{A\Delta X} + \mathbf{Bs} = \mathbf{\Delta T}$$

where $\mathbf{\Delta T}$ is a N_T vector containing the arrival time residuals, $\mathbf{A}$ defines a $N_T \times M_T$ matrix containing the partial derivatives which are calculated at a set of initial location estimates, $\mathbf{\Delta X}$ is a M_T vector containing the changes in hypocentral parameters we wish to determine ($M_T = 4 \times P$), and $\mathbf{s}$ is a K_T vector containing static station terms, each of which is a constant for all events recorded by a given station. $\mathbf{B}$ is a $N_T \times K_T$ matrix that selects the correct station term for each arrival time, i.e.,

$$\left[\mathbf{B_p}\right]_{ij} = \begin{cases} 1 & \text{when } \left[\mathbf{\Delta t_p}\right]_i \text{ is from station } j \\ 0 & \text{otherwise} \end{cases}$$

This is a coupled set of equations for the unknowns $\mathbf{\Delta X}$ and $\mathbf{s}$, which may be solved iteratively by first solving for the locations $\mathbf{\Delta X}$ while holding the station terms $\mathbf{s}$ fixed, then solving for the station terms $\mathbf{s}$ while holding the locations $\mathbf{\Delta X}$ fixed, etc. This method has been applied for many years in seismology and was described by Frohlich (1979). Here we show that this method is equivalent to a power series, which should converge to the least squares solution for $\mathbf{\Delta X}$ and $\mathbf{s}$.

For the first iteration, we begin with zero station terms:

$$\mathbf{s}_1 = \mathbf{0}$$

then we solve the single event location problem starting with the initial guess of the hypocenter parameters and data,

$$\mathbf{A\Delta X}_1 = \mathbf{\Delta T}$$

$$\mathbf{\Delta X}_1 = \mathbf{A}^{\dagger}\mathbf{\Delta T}$$

but since the data cannot be fit perfectly even with the adjusted locations, we will obtain a new set of travel time residuals $\mathbf{R}_1$. The next step is to solve for the station terms from the new locations.

$$\begin{aligned}
\mathbf{R}_1 &= \mathbf{\Delta T} - \mathbf{A}\mathbf{\Delta X}_1 \\
&= \mathbf{\Delta T} - \mathbf{A}\mathbf{A}^{\dagger}\mathbf{\Delta T} \\
&= \left(\mathbf{I}_{\mathbf{N_T}} - \mathbf{A}\mathbf{A}^{\dagger}\right)\mathbf{\Delta T}
\end{aligned}$$

$$\begin{aligned}
\mathbf{s}_2 &= \mathbf{B}^{\dagger}\mathbf{R}_1 \\
&= \mathbf{B}^{\dagger}\left(\mathbf{I}_{\mathbf{N_T}} - \mathbf{A}\mathbf{A}^{\dagger}\right)\mathbf{\Delta T}
\end{aligned}$$

$$\begin{aligned}
\mathbf{\Delta T}_2 &= \mathbf{\Delta T} - \mathbf{B}\mathbf{s}_2 \\
&= \mathbf{\Delta T} - \mathbf{B}\mathbf{B}^{\dagger}\left(\mathbf{I}_{\mathbf{N_T}} - \mathbf{A}\mathbf{A}^{\dagger}\right)\mathbf{\Delta T} \\
&= \left[\mathbf{I}_{\mathbf{N_T}} - \mathbf{B}\mathbf{B}^{\dagger} + (\mathbf{B}\mathbf{B}^{\dagger})(\mathbf{A}\mathbf{A}^{\dagger})\right]\mathbf{\Delta T}
\end{aligned}$$

where $\mathbf{R}_1$ is a travel-time residual vector and dagger means generalized inverse.

We continue with the second iteration as follows:

$$\begin{aligned}
\mathbf{A}\mathbf{\Delta X}_2 &= \mathbf{\Delta T}_2 \\
\mathbf{\Delta X}_2 &= \mathbf{A}^{\dagger}\mathbf{\Delta T}_2 \\
&= \mathbf{A}^{\dagger}\left[\mathbf{I}_{\mathbf{N_T}} - \mathbf{B}\mathbf{B}^{\dagger} + (\mathbf{B}\mathbf{B}^{\dagger})(\mathbf{A}\mathbf{A}^{\dagger})\right]\mathbf{\Delta T}
\end{aligned}$$

$$\begin{aligned}
\mathbf{R}_2 &= \mathbf{\Delta T}_2 - \mathbf{A}\mathbf{\Delta X}_2 \\
&= \mathbf{\Delta T}_2 - \mathbf{A}\mathbf{A}^{\dagger}\mathbf{\Delta T}_2 \\
&= \left(\mathbf{I}_{\mathbf{N_T}} - \mathbf{A}\mathbf{A}^{\dagger}\right)\mathbf{\Delta T}_2 \\
&= \left(\mathbf{I}_{\mathbf{N_T}} - \mathbf{A}\mathbf{A}^{\dagger}\right)\left[\mathbf{I}_{\mathbf{N_T}} - \mathbf{B}\mathbf{B}^{\dagger} + (\mathbf{B}\mathbf{B}^{\dagger})(\mathbf{A}\mathbf{A}^{\dagger})\right]\mathbf{\Delta T}
\end{aligned}$$

$$
\begin{aligned}
\mathbf{s}_3 &= \mathbf{B}^{\dagger}\mathbf{R}_2 \\
&= \mathbf{B}^{\dagger}\left(\mathbf{I}_{\mathbf{N_T}} - \mathbf{A}\mathbf{A}^{\dagger}\right)\boldsymbol{\Delta}\mathbf{T}_2 \\
&= \mathbf{B}^{\dagger}\left(\mathbf{I}_{\mathbf{N_T}} - \mathbf{A}\mathbf{A}^{\dagger}\right)\left[\mathbf{I}_{\mathbf{N_T}} - \mathbf{B}\mathbf{B}^{\dagger} + (\mathbf{B}\mathbf{B}^{\dagger})(\mathbf{A}\mathbf{A}^{\dagger})\right]\boldsymbol{\Delta}\mathbf{T}
\end{aligned}
$$

$$
\begin{aligned}
\boldsymbol{\Delta}\mathbf{T}_3 &= \boldsymbol{\Delta}\mathbf{T}_2 - \mathbf{B}\mathbf{s}_3 \\
&= \boldsymbol{\Delta}\mathbf{T}_2 - \mathbf{B}\mathbf{B}^{\dagger}\left(\mathbf{I}_{\mathbf{N_T}} - \mathbf{A}\mathbf{A}^{\dagger}\right)\boldsymbol{\Delta}\mathbf{T}_2 \\
&= \left[\mathbf{I}_{\mathbf{N_T}} - \mathbf{B}\mathbf{B}^{\dagger} + (\mathbf{B}\mathbf{B}^{\dagger})(\mathbf{A}\mathbf{A}^{\dagger})\right]\boldsymbol{\Delta}\mathbf{T}_2 \\
&= \left[\mathbf{I}_{\mathbf{N_T}} - \mathbf{B}\mathbf{B}^{\dagger} + (\mathbf{B}\mathbf{B}^{\dagger})(\mathbf{A}\mathbf{A}^{\dagger})\right]^2\boldsymbol{\Delta}\mathbf{T}
\end{aligned}
$$

This can be generalized to the $k+1$ iteration (k $\geq$ 0):

$$
\begin{aligned}
\boldsymbol{\Delta}\mathbf{X}_{k+1} &= \mathbf{A}^{\dagger}\boldsymbol{\Delta}\mathbf{T}_{k+1} \\
&= \mathbf{A}^{\dagger}\left[\mathbf{I}_{\mathbf{N_T}} - \mathbf{B}\mathbf{B}^{\dagger} + (\mathbf{B}\mathbf{B}^{\dagger})(\mathbf{A}\mathbf{A}^{\dagger})\right]^k\boldsymbol{\Delta}\mathbf{T}
\end{aligned}
$$

$$
\begin{aligned}
\mathbf{s}_{k+2} &= \mathbf{B}^{\dagger}\mathbf{R}_{k+1} \\
&= \mathbf{B}^{\dagger}\left(\mathbf{I}_{\mathbf{N_T}} - \mathbf{A}\mathbf{A}^{\dagger}\right) \\
&\qquad \cdot\left[\mathbf{I}_{\mathbf{N_T}} - \mathbf{B}\mathbf{B}^{\dagger} + (\mathbf{B}\mathbf{B}^{\dagger})(\mathbf{A}\mathbf{A}^{\dagger})\right]^k\boldsymbol{\Delta}\mathbf{T}
\end{aligned}
$$

So far, we have shown the changes in hypocentral parameters $\Delta\mathbf{X}_k$ and station terms $\mathbf{s}_k$ can be expressed as vector sequences. To show that these sequences are convergent, we use the equivalence between least squares fitting and orthogonal projection. Our problem can be defined as follows: we have a data space $\mathbf{T}$ and two model spaces, $\mathbf{M_U}$ and $\mathbf{M_V}$, the space of the location vectors and the space of the station term vectors. The linear function $\Phi_{\mathbf{U}} : \mathbf{M_U} \to \mathbf{T}$ gives the data vector produced by each location vector, and $\Phi_{\mathbf{V}} : \mathbf{M_V} \to \mathbf{T}$ gives the data vector produced by each station terms vector. Let $\mathbf{U} = \Phi_{\mathbf{U}}(\mathbf{M_U})$ and $\mathbf{V} = \Phi_{\mathbf{V}}(\mathbf{M_V})$.

If $\mathbf{t}$ is the observed data vector (i.e., $\boldsymbol{\Delta}\mathbf{T}$ in our previous notation), then our iteration scheme proceeds as follows. First, we set the initial station term contribution to the data vector to zero:

$$\begin{aligned}
\mathbf{v}_1 &= \mathbf{0} \\
\mathbf{u}_1 &= \mathbf{P_U}(\mathbf{t} - \mathbf{v}_1) = \mathbf{P_U}(\mathbf{t}) \\
\mathbf{v}_2 &= \mathbf{P_V}(\mathbf{t} - \mathbf{u}_1) = \mathbf{P_V}(\mathbf{t}) - \mathbf{P_V}\mathbf{P_U}(\mathbf{t}) \\
&\vdots
\end{aligned}$$

$$\begin{aligned}
\mathbf{v}_{k+1} &= \mathbf{P_V}(\mathbf{t} - \mathbf{u}_k) \\
\mathbf{u}_{k+1} &= \mathbf{P_U}(\mathbf{t} - \mathbf{v}_{k+1})
\end{aligned}$$

where $\mathbf{P_U}$ is the orthogonal projector of $\mathbf{T}$ onto $\mathbf{U}$ and $\mathbf{P_V}$ is the orthogonal projector of $\mathbf{T}$ onto $\mathbf{V}$. Note that $\mathbf{P_U} = \mathbf{A}\mathbf{A}^\dagger$ and $\mathbf{P_V} = \mathbf{B}\mathbf{B}^\dagger$ in our previous notation. Then for k ≥ 1,

$$\begin{aligned}
\mathbf{u}_{k+1} &= \mathbf{P_U}\big[\mathbf{t} - \mathbf{P_V}(\mathbf{t} - \mathbf{u}_k)\big] \\
&= \mathbf{P_U}(\mathbf{t}) - \mathbf{P_U}\mathbf{P_V}(\mathbf{t}) + \mathbf{P_U}\mathbf{P_V}(\mathbf{u}_k) \\
&= \check{\mathbf{u}} + \mathbf{P_U}\mathbf{P_V}(\mathbf{u}_k) \\
&= \left[\mathbf{I} + \mathbf{P_U}\mathbf{P_V} + \cdots + (\mathbf{P_U}\mathbf{P_V})^{k-1}\right]\check{\mathbf{u}} + \mathbf{P_U}\mathbf{P_V}(\mathbf{u}_1)
\end{aligned}$$

where $\check{\mathbf{u}} = \mathbf{P_U}(\mathbf{t}) - \mathbf{P_U}\mathbf{P_V}(\mathbf{t})$

$$\begin{aligned}
\mathbf{v}_{k+1} &= \mathbf{P_V}\big[\mathbf{t} - \mathbf{P_U}(\mathbf{t} - \mathbf{v}_k)\big] \\
&= \mathbf{P_V}(\mathbf{t}) - \mathbf{P_V}\mathbf{P_U}(\mathbf{t}) + \mathbf{P_V}\mathbf{P_U}(\mathbf{v}_k) \\
&= \mathbf{v}_2 + \mathbf{P_V}\mathbf{P_U}(\mathbf{v}_k) \\
&= \left[\mathbf{I} + \mathbf{P_V}\mathbf{P_U} + \cdots + (\mathbf{P_V}\mathbf{P_U})^{k-1}\right]\mathbf{v}_2
\end{aligned}$$

They will converge if $||\mathbf{P_V}\mathbf{P_U}|| < \mathbf{1}$ and $||\mathbf{P_U}\mathbf{P_V}|| < \mathbf{1}$. In finite-dimensional spaces, these inequalities hold whenever $\mathbf{U} \cap \mathbf{V} = \{\mathbf{0}\}$. However, in our case there is a nonuniqueness problem in that part of the data vector produced by the model can come from either the location vector or the station term vector. For example, a constant time added to the data vector could correspond to a change in the earthquake origin times or a change in the station terms. For this reason, in general $\mathbf{U} \cap \mathbf{V} \neq \{\mathbf{0}\}$.

In this case, let $\mathbf{W} = \mathbf{U} \cap \mathbf{V}$, $\mathbf{U} = \widetilde{\mathbf{U}} + \mathbf{W}$, and $\mathbf{V} = \widetilde{\mathbf{V}} + \mathbf{W}$, where $\widetilde{\mathbf{U}} \perp \mathbf{W}$ and $\widetilde{\mathbf{V}} \perp \mathbf{W}$. We then have $\widetilde{\mathbf{U}} \cap \widetilde{\mathbf{V}} = \{\mathbf{0}\}$. We can write $\mathbf{t} = \tilde{\mathbf{u}} + \tilde{\mathbf{v}} + \mathbf{w} + \tilde{\mathbf{t}}$, with $\tilde{\mathbf{u}} \in \widetilde{\mathbf{U}}$, $\tilde{\mathbf{v}} \in \widetilde{\mathbf{V}}$, $\mathbf{w} \in \mathbf{W}$, and $\tilde{\mathbf{t}} \in \left(\widetilde{\mathbf{U}} + \widetilde{\mathbf{V}} + \mathbf{W}\right)^{\perp}$.

Some remarks are:

$$\begin{aligned}
\widetilde{\mathbf{U}} \cap \mathbf{V} &= \mathbf{U} \cap \widetilde{\mathbf{V}} = \{\mathbf{0}\} \\
\mathbf{P}_{\mathbf{U}} &= \mathbf{P}_{\widetilde{\mathbf{U}}} + \mathbf{P}_{\mathbf{W}} \\
\mathbf{P}_{\mathbf{V}} &= \mathbf{P}_{\widetilde{\mathbf{V}}} + \mathbf{P}_{\mathbf{W}} \\
\mathbf{P}_{\widetilde{\mathbf{U}}}\mathbf{P}_{\mathbf{W}} &= \mathbf{P}_{\mathbf{W}}\mathbf{P}_{\widetilde{\mathbf{U}}} = \mathbf{0} \\
\mathbf{P}_{\widetilde{\mathbf{V}}}\mathbf{P}_{\mathbf{W}} &= \mathbf{P}_{\mathbf{W}}\mathbf{P}_{\widetilde{\mathbf{V}}} = \mathbf{0} \\
\mathbf{P}_{\mathbf{U}}\mathbf{P}_{\mathbf{V}} &= \mathbf{P}_{\widetilde{\mathbf{U}}}\mathbf{P}_{\widetilde{\mathbf{V}}} + \mathbf{P}_{\mathbf{W}} \\
\mathbf{P}_{\mathbf{V}}\mathbf{P}_{\mathbf{U}} &= \mathbf{P}_{\widetilde{\mathbf{V}}}\mathbf{P}_{\widetilde{\mathbf{U}}} + \mathbf{P}_{\mathbf{W}}
\end{aligned}$$

For the station terms vector we have

$$\begin{aligned}
\mathbf{v}_2 &= \mathbf{P}_{\mathbf{V}}(\mathbf{t}) - \mathbf{P}_{\mathbf{V}}\mathbf{P}_{\mathbf{U}}(\mathbf{t}) \\
&= \left[\mathbf{P}_{\widetilde{\mathbf{V}}}(\mathbf{t}) + \mathbf{P}_{\mathbf{W}}(\mathbf{t})\right] - \left[\mathbf{P}_{\widetilde{\mathbf{V}}}\mathbf{P}_{\widetilde{\mathbf{U}}}(\mathbf{t}) + \mathbf{P}_{\mathbf{W}}(\mathbf{t})\right] \\
&= \mathbf{P}_{\widetilde{\mathbf{V}}}(\mathbf{t}) - \mathbf{P}_{\widetilde{\mathbf{V}}}\mathbf{P}_{\widetilde{\mathbf{U}}}(\mathbf{t})
\end{aligned}$$

and for k ≥ 1

$$\begin{aligned}
\mathbf{v}_{k+1} &= \mathbf{v}_2 + \mathbf{P}_{\mathbf{V}}\mathbf{P}_{\mathbf{U}}(\mathbf{v}_k) \\
&= \mathbf{v}_2 + \mathbf{P}_{\widetilde{\mathbf{V}}}\mathbf{P}_{\widetilde{\mathbf{U}}}(\mathbf{v}_k) + \mathbf{P}_{\mathbf{W}}(\mathbf{v}_k)
\end{aligned}$$

Clearly $\mathbf{v}_2 \in \widetilde{\mathbf{V}}$, and if $\mathbf{v}_k \in \widetilde{\mathbf{V}}$ $(k \geq 2)$, then $\mathbf{P}_{\mathbf{W}}(\mathbf{v}_k) = 0$, so $\mathbf{v}_{k+1} \in \widetilde{\mathbf{V}}$. Thus, by induction, $\mathbf{v}_k \in \widetilde{\mathbf{V}}$ for all k, $\mathbf{P}_{\mathbf{W}}(\mathbf{v}_k) = 0$, and for k ≥ 1

$$\begin{aligned}
\mathbf{v}_{k+1} &= \mathbf{v}_2 + \mathbf{P}_{\widetilde{\mathbf{V}}}\mathbf{P}_{\widetilde{\mathbf{U}}}(\mathbf{v}_k) + \mathbf{P}_{\mathbf{W}}(\mathbf{v}_k) \\
&= \mathbf{v}_2 + \mathbf{P}_{\widetilde{\mathbf{V}}}\mathbf{P}_{\widetilde{\mathbf{U}}}(\mathbf{v}_k) \\
&= \left[\mathbf{I}_{\widetilde{\mathbf{V}}} + \mathbf{P}_{\widetilde{\mathbf{V}}}\mathbf{P}_{\widetilde{\mathbf{U}}} + \cdots + \left(\mathbf{P}_{\widetilde{\mathbf{V}}}\mathbf{P}_{\widetilde{\mathbf{U}}}\right)^{k-1}\right](\mathbf{v}_2)
\end{aligned}$$

Since $\widetilde{\mathbf{U}} \cap \widetilde{\mathbf{V}} = \{\mathbf{0}\}$, $||\mathbf{P}_{\widetilde{\mathbf{V}}}\mathbf{P}_{\widetilde{\mathbf{U}}}|| < 1$, so this series converges.

For the location vector, we have

$$\mathbf{u}_{k+1} = \mathbf{P}_{\mathbf{U}}(\mathbf{t} - \mathbf{v}_{k+1})$$

Since $\{\mathbf{v}_1, \mathbf{v}_2, \ldots\}$ converges and $\mathbf{P}_{\mathbf{U}}$ is continuous, then $\{\mathbf{u}_1, \mathbf{u}_2, \ldots\}$ also converges.

Our proof for convergence is limited to the least squares (L2 norm) solution of the static station term case described in the text. It can be shown that the proof fails for all non-Euclidian norms, but we do not know whether the result itself fails. We have found in practice (for both real and synthetic data) that convergence is quite rapid, typically being achieved in five iterations or less. We have also noticed that this iterative method seems to work for L1 norm locations algorithms as well, although we have not found a formal proof of convergence. Finally, this approach forms the basis for the SSST algorithm, which, although more complicated than static station terms, also achieves convergence in a small number of iterations in our tests on synthetic data. The SSST algorithm applied by Richards-Dinger and Shearer (2000) to the southern California seismic catalog used a grid-search L1 norm approach and achieved a reasonably stable result after 10 iterations.

2.7 References

Douglas, A. (1967). Joint epicentre determination. *Nature*, **215**, 47–48.

Evernden, J. F. (1969). Precision of epicentres obtained by small numbers of world-wide stations. *Bull. Seismol. Soc. Am.*, **59**, 1365–1398.

Freedman, H. W. (1967). A statistical discussion of P residuals from explosions, Part ii. *Bull. Seismol. Soc. Am.*, **57**, 545–561.

Frohlich, C. (1979). An efficient method for joint hypocenter determination for large groups of earthquakes. *Computers & Geosciences*, **5**, 387–389.

Jordan, T. H. and K. A. Sverdrup (1981). Teleseismic location techniques and their application to earthquake clusters in the south-central Pacific. *Bull. Seismol. Soc. Am.*, **71**, 1105–1130.

Lilwall, R. C. and A. Douglas (1970). Estimation of P-wave travel times using the joint epicentre method. *Geophys. J. R. Astron. Soc.*, **19**, 165–181.

Pavlis, G. L. and J. R. Booker (1983). Progressive multiple event location (PMEL). *Bull. Seismol. Soc. Am.*, **73**, 1753–1777.

Pavlis, G. L. and N. B. Hokanson (1985). Separated earthquake location. *J. Geophys. Res.*, **90**, 12,777–12,789.

Pujol, J. (1988). Comments on the joint determination of hypocenters and station corrections. *Bull. Seismol. Soc. Am.*, **78**, 1179–1189.

Richards-Dinger, K. B. and P. M. Shearer (2000). Earthquake locations in southern California obtained using source-specific station terms. *J. Geophys. Res.*, **105**, 10,939–10,960.

Rubin, A. M., D. Gillard and J.-L. Got (1999). Streaks of microearthquakes along creeping faults. *Nature*, **400**, 635–641.

Shearer, P. M. (2002). Parallel fault strands at 9-km depth resolved on the Imperial Fault, southern California. *Geophys. Res. Lett.*, **29**, doi: 10.1029/2002GL015302.

Smith, E. G. C. (1982). An efficient algorithm for routine joint hypocentre determination. *Phys. Earth Planet. Inter.*, **30**, 135–144.

Viret, M., G. A. Bollinger, J. A. Snoke and J. W. Dewey (1984). Joint hypocenter relocation studies with sparse data sets–a case history: Virginia earthquakes. *Bull. Seismol. Soc. Am.*, **74**, 2297–2311.

Waldhauser, F. (2001). hypoDD: A program to compute double-difference hypocenter locations (hypoDD version 1.0, 03/2001). *U. S. Geol. Surv. open-File Rept.*, 01–113.

Waldhauser, F. and W. L. Ellsworth (2000). A double-difference earthquake location algorithm: method and application to the Northern Hayward Fault, California. *Bull. Seismol. Soc. Am.*, **90**, 1353–1368.

Waldhauser, F. and W. L. Ellsworth (2002). Fault structure and mechanics of the Hayward Fault, California, from double-difference earthquake locations. *J. Geophys. Res.*, **107**, 2054, doi: 10.1029/2000JB000084.

Waldhauser, F., W. L. Ellsworth and A. Cole (1999). Slip-parallel seismic lineations on the northern Hayward Fault, California. *Geophys. Res. Lett.*, **26**, 3525–3528.

Wolfe, C. (2002). On the mathematics of using difference operators to relocate earthquakes. *Bull. Seismol. Soc. Am.*, **92**, 2879–2892.

The text of this chapter, in full, is a reformatted version of the material as it appears in Lin, G. and P. M. Shearer, Tests of Relative Earthquake Location Techniques Using Synthetic Data, *Journal of Geophysical Research, vol. 110*, B04304, doi:10.1029/2004JB003380, 2005. The dissertation author was the primary researcher and author. The co-author directed and supervised the research which forms the basis of this chapter. The original paper is copyrighted by the American Geophysical Union, and the material is included here by permission of AGU.

Chapter 3

Obtaining Absolute Locations for Quarry Seismicity Using Remote Sensing Data

Abstract. We obtain absolute locations for 19 clusters of mining-induced seismicity in southern California by identifying quarries using remote sensing data, including optical imagery and differential digital elevation models. These seismicity clusters contain 16,574 events from the Southern California Seismic Network from 1984 to 2002, which are flagged as quarry blasts but without any ground-truth location constraints. Using georeferenced airphotos and satellite radar topography data, we identify the likely sources of these events as quarries that are clearly visible within 1 to 2 km of the seismically determined locations. We then shift the clusters to align with the airphoto images, obtaining an estimated absolute location accuracy of $\sim$200 m for the cluster centroids. The improved locations of these explosions should be helpful for constraining regional 3D velocity models.

3.1 Introduction

Because of the trade-off between earthquake locations and velocity structure in the tomography problem, controlled sources are often used in velocity inversions to provide absolute reference locations for 3D velocity models and to constrain the shallow crustal structure. Ideally these are calibration shots of known locations and origin times. Quarry blasts are also sometimes used, however, which typically have known locations but unknown origin times. When included in the location algorithms, the hypocentral parameters of these controlled sources (locations and/or origin times) are fixed.

Absolute location information is typically available for only a fraction of the artificial sources located by local and regional networks. For example, the Southern California Seismic Network (SCSN) lists 23,748 events from 1984 to 2002 as shots or quarry blasts, but only 77 of these have true location information (E. Hauksson, personal comm., 2005). Here, we demonstrate with SCSN events how remote sensing data (air or satellite photos and digital elevation maps) can be used to determine the absolute locations of quarry seismicity clusters to about 200 m accuracy. The results produce a check on catalog location accuracy as well as new constraints for the tomography problem.

3.2 Method

We use as our starting point the SHLK location catalog (Shearer *et al.*, 2003, 2005), which contains precise relative relocations for more than 340,000 southern California earthquakes that occurred between 1984 and 2002, as computed by the source-specific station term, waveform cross-correlation, and cluster analysis methods. The relative location errors are estimated from the internal consistency of differential locations between individual event pairs and are often as small as tens of meters. Because of imprecise knowledge of the 3D velocity structure, however, the absolute locations of seismicity clusters are much worse constrained, with location errors as large as a few kilometers.

The SCSN flags 23,748 events as quarry blasts in southern California between 1984 and 2002 (see Figure 3.1). As noted by Agnew (1990), Richards-Dinger and Shearer (2000), and Wiemer and Baer (2000), artificial seismicity can also be identified using comparisons of daytime versus nighttime seismic

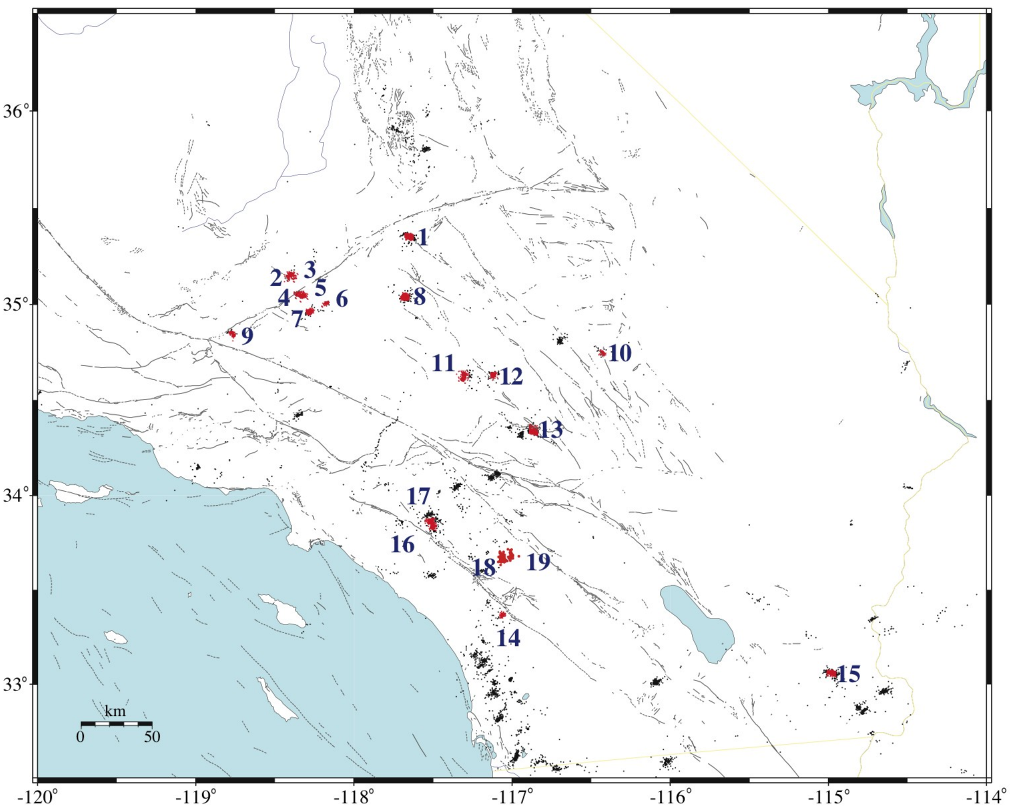

Figure 3.1. Map view of the 23,478 quarry blasts flagged by the Southern California Seismic Network (SCSN) between 1984 and 2002 in southern California plotted at their SHLK catalog locations. The red dots represent the seismicity clusters that we are able to relocate using airphoto or satellite images. Also shown are the numbers used to identify the respective clusters in our study. Gray lines denote active Quaternary faults.

activity. However, we find that the quarry blast list from the SCSN catalog is more complete than that derived from a simple analysis of the diurnal seismicity patterns. We therefore use the SCSN-defined blast data in this study. The red dots in Figure 3.1 represent the 16,574 events that we are able to relocate. For other events, we could not find suitable airphoto images or identify unambiguous source locations. In many cases, the corresponding events represent distributed explosions associated with road construction or military bombing ranges.

We estimate the true locations of the quarry blasts from airphoto images provided by AirPhoto USA (available at http://terraserver.com/). AirPhoto USA's catalog consists of recent, true-color, high-resolution aerial photography of many regions in the United States. The resolution of the images used in this study is typically 8 m but can be as small as 0.6 m. Figure 3.2 illustrates our method as applied to cluster 11 in Figure 3.1. Figure 3.2a is a closeup of the cluster events as seismically located in the SHLK catalog. Figure 3.2b shows the corresponding airphoto image in the same coordinate frame. The ground resolution of this image is 8 m. The disturbed terrain near the top right corner shows a quarry that is the obvious source of seismicity, but the quarry location is about 0.8 km southwest of the seismicity cluster.

To verify that the quarry is indeed the source of seismic activity, we have analyzed changes in the Earth's topography using digital elevation model (DEM) data from the National Elevation Dataset (NED, http://ned.usgs.gov) and the Shuttle Radar Topography Mission (SRTM) (Farr and Kobrick, 2000). The SRTM data were collected in 2000, whereas the NED data represent a compilation from various measurements conducted between 1925 and 1999. The vertical accuracy of both DEMs is of the order of 10 m. Therefore a systematic difference between the two DEMs that exceeds 10 m is indicative of changes in the surface elevation that occurred between the acquisition dates of the respective DEMs. Figure 3.2c shows a differential DEM for the same area as in Figure 3.2a and b. White regions in Figure 3.2c denote areas where the elevation has decreased by more than 20 m, presumably because of ground excavation. The location of the area of a decrease in surface elevation agrees with the quarry location inferred from the optical imagery (Figure 3.2b). The horizontal resolution of the digital topography data is 30 m. Our approach is to use the airphoto images to locate probable quarries and differential DEM to confirm that

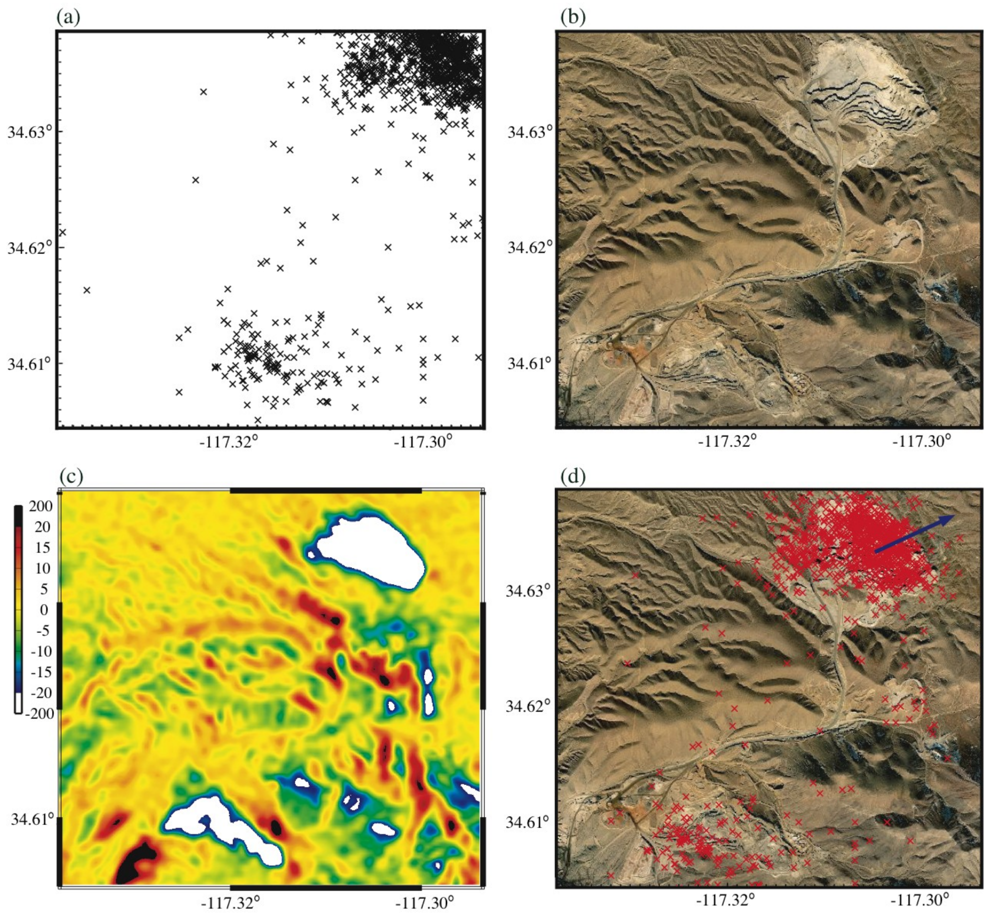

Figure 3.2. Details of relocation method for cluster 11 in Figure 3.1. (a) The starting SHLK seismicity clusters. (b) The airphoto image corresponding to the clusters in (a). (c) The differential DEM data plot for the same area. Positive changes (red) represent topography increases and negative changes (blue) represent topography decreases. The most extreme changes are shown in black and white. The white spots are likely quarries, confirming their locations as shown in (b). (d) The shifted clusters together with the airphoto image. The arrow shows the mislocation vector from the estimated true locations to the starting SHLK locations.

these features are associated with the removal of a significant volume of material. The remote sensing data alone cannot determine when the quarries were active, but it seems likely that the observed events (flagged in the SCSN catalog as quarry blasts) are caused by explosions at these sites.

Next, we compare Figure 3.2a and b and shift the entire seismicity cluster to align with the imaged quarry as shown in Figure 3.2d. The blue arrow gives the mislocation vector for the cluster, the location shift from our estimated true location to the SHLK location. Note that this is opposite to the direction that we shift the SHLK cluster to align with the quarry image. Notice that the $\sim$1 km width of the quarry indicates that most of the scatter shown in the SHLK locations is real; this is consistent with the relative event location accuracy among nearby events being much better than the absolute location accuracy of the entire cluster. There is some subjectivity in determining the best shift of the seismicity clusters; in general, we attempt to visually align the cluster centroid with the center of the quarry shown in the airphoto but in some cases irregularities in the quarry shape provide a better alignment method. Further refinements might be possible by studying the time evolution of the quarries by examining airphotos at different dates and comparing them with the seismic results, but we do not attempt this here.

Notice that several smaller quarries are visible to the southwest of the main quarry, one of which is associated with its own seismicity cloud. In this case, the alignment obtained for the main quarry appears to also roughly align the secondary quarry, so we do not perform a separate alignment of the secondary quarry. This is again consistent with the much smaller relative relocation error, even between different clusters, compared with absolute location error for the SHLK catalog. In other cases, however, nearby quarries appear to have significantly different mislocation vectors, even when the quarries are only a few kilometers apart. Thus, we perform separate alignments for the cluster pairs 2–3, 4–5, 16–17, and 18–19.

Additional examples of our method are included in Figure 3.3 and Figure 3.4 for clusters 3 and 5 (see Figure 3.1), respectively. In these examples, secondary quarries visible in the same images are used to separately locate clusters 2 and 4 in Figure 3.1. Figure 3.5 presents all 19 clusters that we relocated using the optical images in our study. The arrows show the directions of the mislocation vectors with the size proportional to the distance from the true locations (red dots) to the initial SHLK locations (black

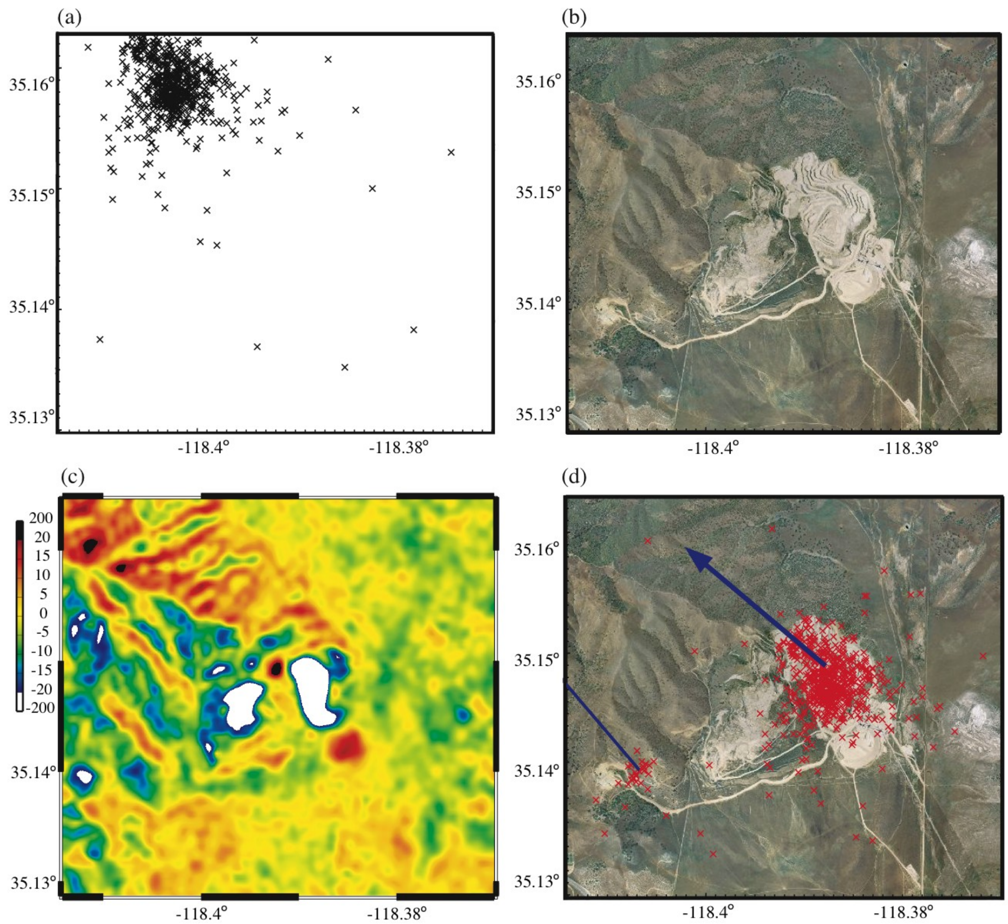

Figure 3.3. Application of relocation method for cluster 3. Notation is the same as in Figure 3.2. There is a small cluster on the left side of (d) with the mislocation vector, which is cluster 2 in Figure 3.5. These two clusters are relocated separately because the mislocation vectors are different. (For more details, please refer to the text.)

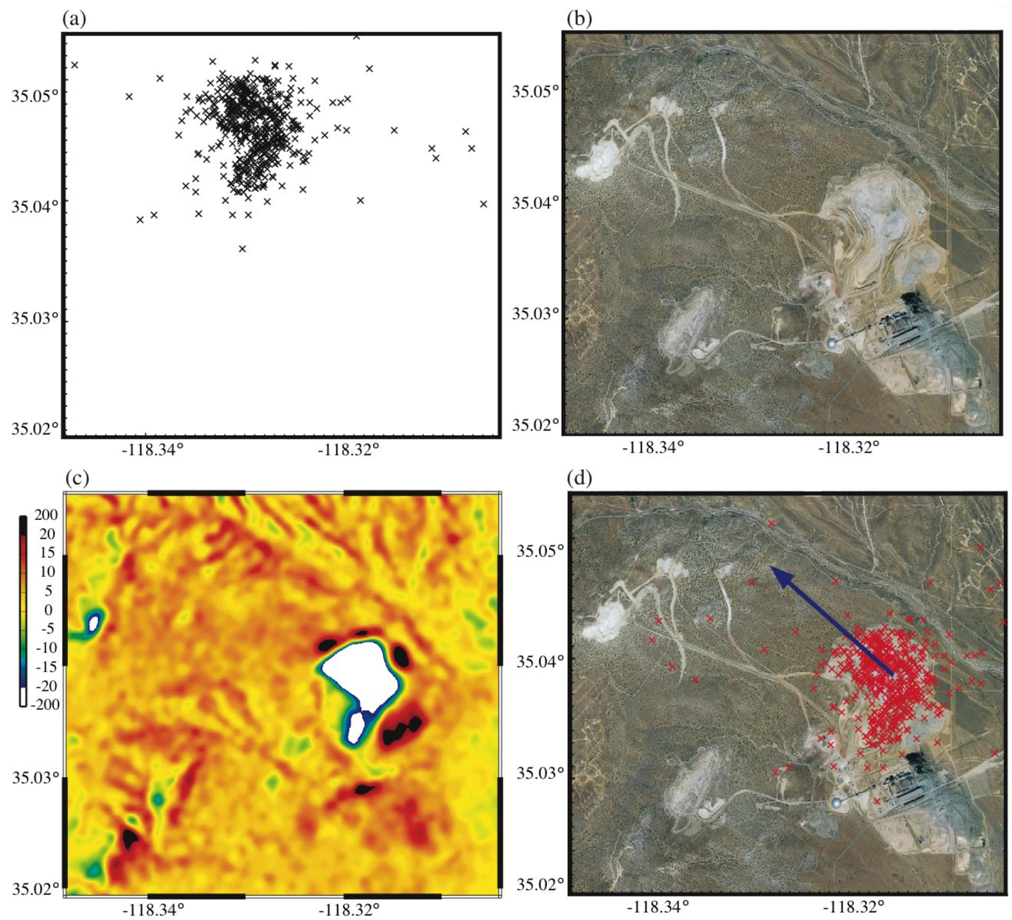

Figure 3.4. Application of relocation method for cluster 5. Notation is the same as in Figure 3.2.

dots). Figure 3.6 shows the mislocation vectors mapped onto the quarry locations. Note that the scale for the arrow length is increased compared with the map scale to make the arrows visible. The location errors for all the clusters in our study are less than 2.1 km, with most errors being less than 1 km. This implies that the absolute horizontal location error of the SHLK catalog is generally less than 1 km but can be as much as 2 km. Depth errors can also be evaluated because the SCSN restricts the quarry blasts to be at the surface, whereas the SHLK locations for all event types are allowed to have nonzero depths. The SHLK catalog median depths for the mining-induced clusters in this study range from 0.7 to 3.6 km, with most between 1.2 and 2.4 km. This implies that the SHLK catalog depth errors for shallow events are greater than their horizontal errors, but, in general, are less than 2.5 km.

3.3 Discussion

These results provide additional ground-truth events that can be used to test the accuracy of the catalog locations and remove some of the trade-offs between the event locations and 3D velocity structure in tomographic inversions. The bias in seismically located quarry blasts compared with their true locations exhibits some spatial coherence. For example, clusters 2 to 7 are all biased northwest of their true locations, whereas clusters 1 and 8 are biased eastward of their true locations. Additional information on the location bias is provided by the controlled-source data. Figure 3.7 shows that the controlled-source mislocation vectors are generally consistent with the new mislocation vectors obtained in this study; they typically have a magnitude of 1 to 2 km and roughly agree in direction among nearby clusters.

Significant variability occurs in the results, however, even among clusters separated by only a few kilometers, implying that the near-surface velocity structure is a substantial contributor to the location error. Thus, direct removal of location bias by using calibration events of known location is guaranteed to work well only when the calibration event is quite close to the target events. Even with our new results, the calibration event coverage is too sparse to provide reliable mislocation bias estimates for many regions. Details of the mislocation bias will also be hard to completely resolve with 3D velocity inversions because of their limited spatial resolution compared with the length scale of the variations shown in Figure 3.7.

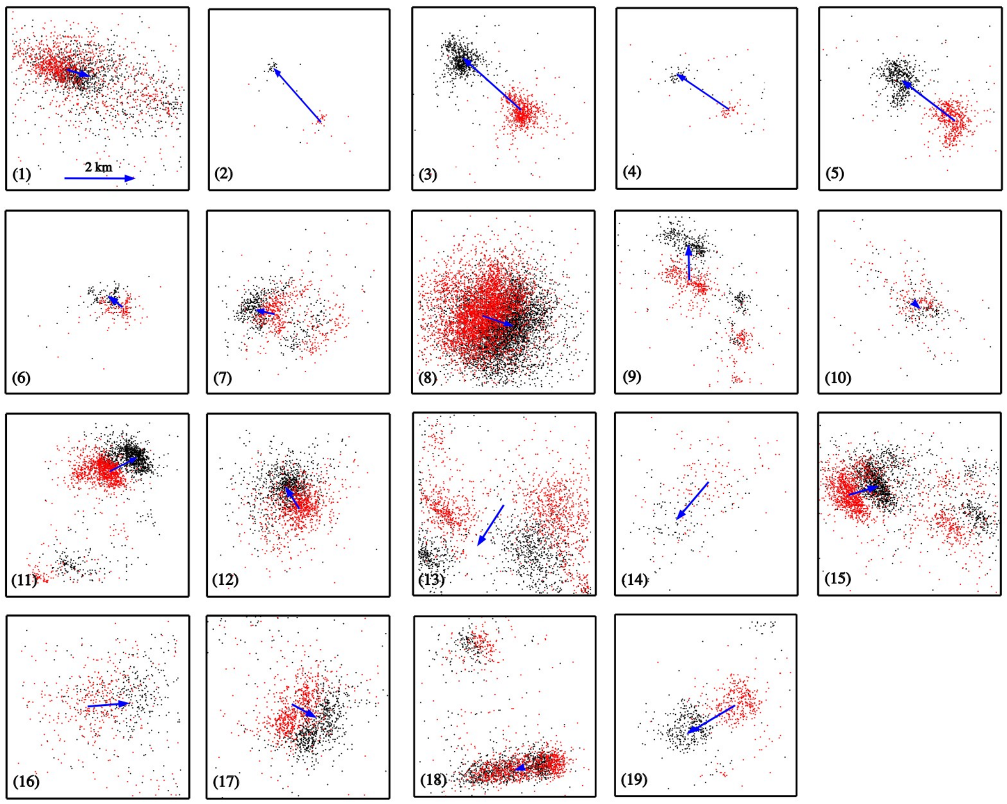

Figure 3.5. The 19 quarry blast clusters examined in our study. The black dots represent the starting SHLK catalog locations, and the red dots represent the improved (shifted) locations. The arrows show the mislocation vectors with the size proportional to the distance from the estimated true locations to the starting SHLK locations. The magnitude of the location changes for all the clusters in our study is less than 2.1 km, implying that the absolute location errors in the SHLK catalog are roughly 1 to 2 km.

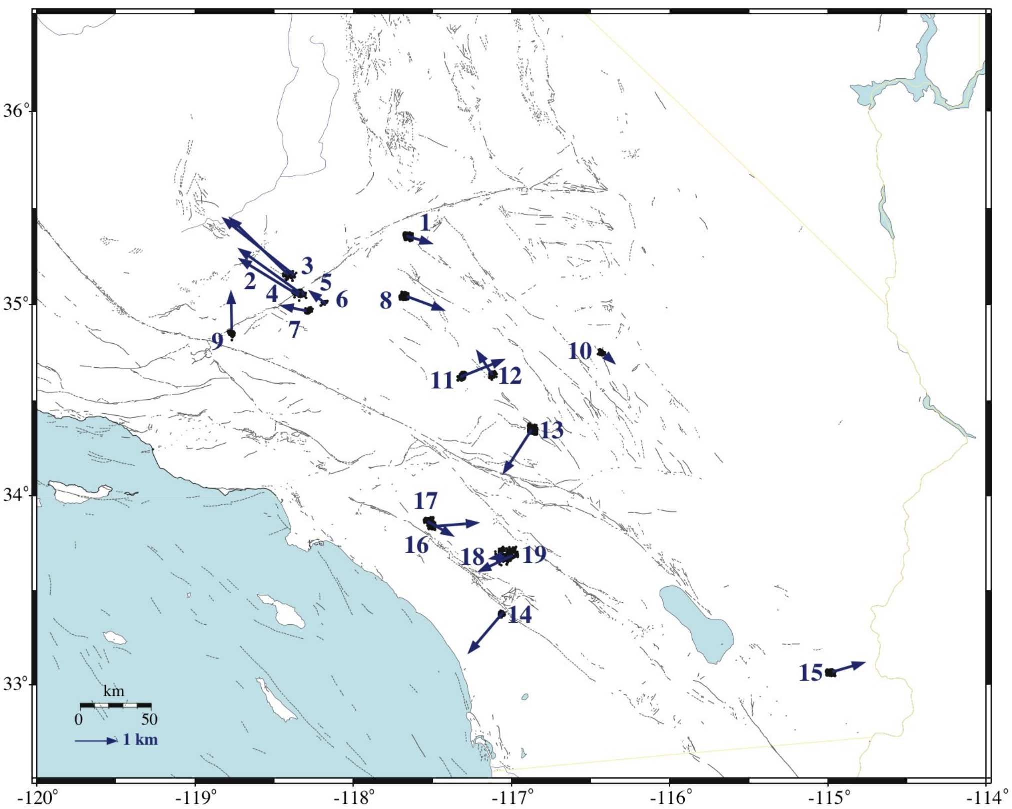

Figure 3.6. The locations of the 19 quarry blast clusters in southern California used in our study. The arrows show the mislocation vectors with the size proportional to the distance from the estimated true locations to the starting SHLK locations. Note the difference between the arrow scale and the map scale.

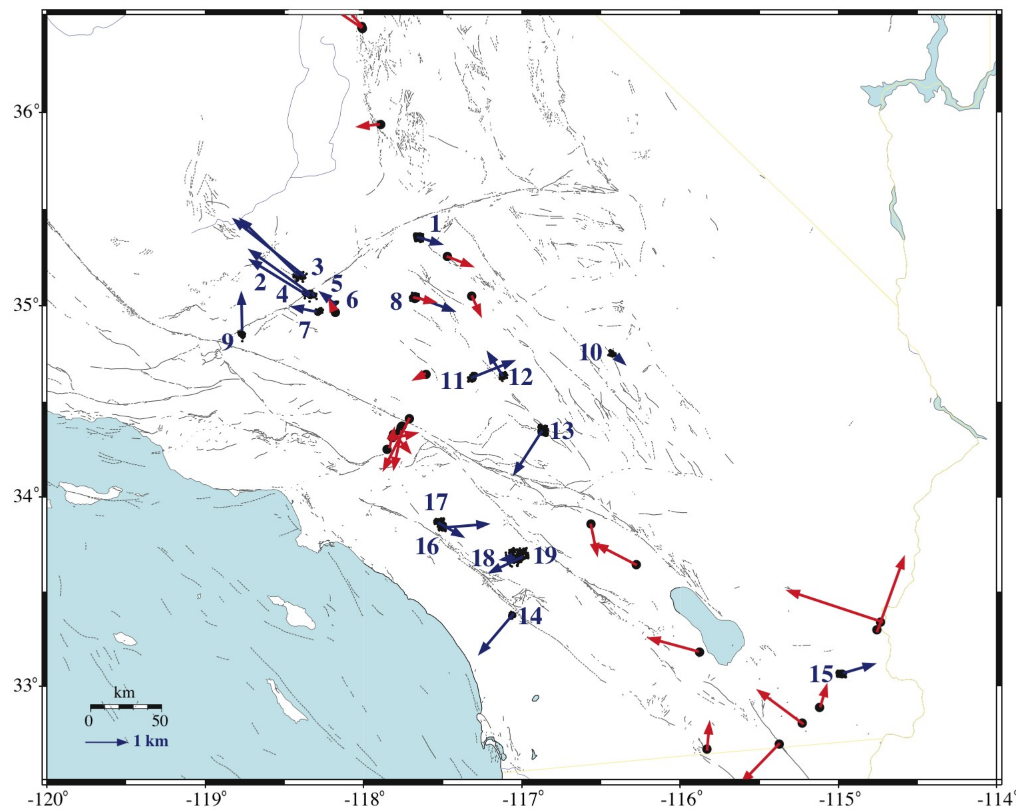

Figure 3.7. The locations of both the 19 quarry seismicity clusters used in our study (blue arrows) and some controlled sources with known locations (red arrows). The arrows show the mislocation vectors with the size proportional to the distance from the estimated true locations to the starting SHLK locations. Note the difference between the arrow scale and the map scale.

Despite these limitations, our new results represent a substantial improvement over existing controlled-source information for southern California and should help to provide better constrained tomography models and absolute earthquake locations. Note that most of the quarries that we study are active operations, for which detailed information could probably be obtained by contacting the quarry operators. The advantage of our approach is that quarry locations can be obtained directly from freely available remote sensing data sets, without the need for any other research, correspondence, or site visits.

3.4 Acknowledgments

We thank Egill Hauksson who provided the controlled-source locations and times and Duncan Agnew for useful suggestions. We also thank Paul Wessel and Walter Smith for developing and supporting the GMT mapping tools (http://gmt.soest.hawaii.edu/). Funding for this research was provided by National Earthquake Hazards Reduction Program/U.S. Geological Survey (USGS) grant 03HQPA0001. This research was also supported by the Southern California Earthquake Center, which is funded by National Science Foundation Cooperative Agreement EAR-0106924 and USGS Cooperative Agreement 02HQAG0008. The Southern California Earthquake Center contribution number for this article is 914.

3.5 References

Agnew, D. C. (1990). The use of time-of-day seismicity maps for earthquake/explosion discrimination by local networks, with an application to the seismicity of San Diego County. *Bull. Seismol. Soc. Am.*, **80**, 747–750.

Farr, T. G. and M. Kobrick (2000). Shuttle Radar Topography Mission produces a wealth of data. *AGU Eos*, **81**, 583–585.

Richards-Dinger, K. B. and P. M. Shearer (2000). Earthquake locations in southern California obtained using source-specific station terms. *J. Geophys. Res.*, **105**, 10,939–10,960.

Shearer, P. M., J. L. Hardebeck, L. Astiz and K. B. Richards-Dinger (2003). Analysis of similar event clusters in aftershocks of the 1994 Northridge, California, earthquake. *J. Geophys. Res.*, **108**, B1, 2035, doi 10.1029/2001JB000685.

Shearer, P. M., E. Hauksson and G. Lin (2005). Southern California hypocenter relocation with waveform cross-correlation, Part 2: results using source-specific station terms and cluster analysis. *Bull. Seismol. Soc. Am.*, **95**, 904–915.

Wiemer, S. and M. Baer (2000). Mapping and removing quarry blast events from seismicity catalogs. *Bull. Seismol. Soc. Am.*, **90**, 525–530.

The text of this chapter, in full, is a reformatted version of the material as it appears in Lin, G., P. Shearer and Y. Fialko, Obtaining Absolute Locations for Quarry Seismicity Using Remote Sensing Data, *Bulletin of the Seismological Society of America, v. 96, No. 2*, 722-728, 2006. The dissertation author was the primary researcher and author. The co-authors directed and supervised the research which forms the basis of this chapter.

Chapter 4

The COMPLOC Earthquake Location Package

4.1 Introduction

This article describes the programs included in the COMPLOC computer program package that are designed to apply the source-specific station term (SSST) method to solve for local earthquake locations using P- and S-wave phase data. These programs can greatly improve the relative location accuracy of nearby events by applying empirical corrections for the biasing effects of three-dimensional velocity structure. They have been tested on data from both the Southern California Seismic Network (SCSN) and Northern California Seismic Network (NCSN).

The SSST method (Richards-Dinger and Shearer, 2000; Lin and Shearer, 2005) works by assigning each station a travel-time correction that varies as a function of source position. This approach provides relative location accuracy comparable to master event or hypocentroidal decomposition (Jordan and Sverdrup, 1981) methods within compact event clusters, but is applicable to distributed seismicity. It has some similarities to the double-difference algorithm (Waldhauser and Ellsworth, 2000, 2002) and can be shown to give comparable results in tests on synthetic data (Lin and Shearer, 2005). However, the SSST approach has computational advantages for big data sets because the location and station term parts of the computation are separate so that large matrix inversions are not necessary. In addition, our implementation of SSST provides the option to use L1-norm misfit measures, which are more robust than least squares in the case of occasional timing errors or bad phase picks.

We implement the SSST approach by selecting nearby events located within a sphere of specified radius $r_{\max}$ around the target event. The station term for the target event is then computed as the median (or mean) residual of these events. Different results will be obtained depending upon the size of the cutoff distance $r_{\max}$. If $r_{\max}$ is set to a large enough distance, then the SSST method will give the same result as the static station term method (in which there is only a single timing correction term for each station). However, if $r_{\max}$ is set to a very small distance, the number of events may not be sufficient to obtain a reliable estimate of the true station term. Thus selection of the cutoff distance is a key factor in the application of the SSST method.

When Richards-Dinger and Shearer (2000) applied an SSST algorithm to locate southern California earthquakes, they obtained their initial locations using the static station term method and then used these station terms as a starting point for the SSST calculation. In this way, they achieved some improvement in the absolute locations of the events before focusing on the relative locations among closely spaced events. A generalization of this approach, adopted in COMPLOC, is to continuously shrink the SSST cutoff distance $r_{\max}$ between the first and final iterations. In other words, we start the cutoff distance with a large value to include all the events from which we calculate station terms, then decrease it to some specified minimum distance to calculate station terms using only the closest events.

More details about the shrinking-box SSST algorithm are contained in Lin and Shearer (2005). The method was also used to relocate 340,000 southern California earthquakes by Shearer *et al.* (2005), a study that went on to relocate events within similar event clusters using waveform cross-correlation times. The COMPLOC package does not include an option to use differential times from waveform cross-correlation, but we hope to add this in a future release.

This paper will describe the programs in COMPLOC, which is available as a UNIX tar file at *http://igpphome.ucsd.edu/∼glin/COMPLOC*. We also will present plots of some of the example data sets contained in the package.

4.2 Program Descriptions

COMPLOC is a Fortran77 computer program package for relocating earthquakes. The program has been tested on both MAC and Sun systems, but it is made available without warranty.

Before beginning the location process, it is necessary to have the following:

1. A one-dimensional velocity versus depth model for the region;

2. A list of station names, their locations and station timing corrections, if available;

3. P and/or S phase pick data and initial locations for the events to be located.

4.2.1 vzfillin

vzfillin.f is a utility program that reads (z, v_p, v_s) model files and resamples them at any desired finer depth interval. This is done with linear interpolation of parameters between depth points so that models with velocity gradients are easily included. It also permits generation of S velocities that are a specified fraction of the P velocities.

4.2.2 deptable

deptable.f is a Fortran77 program that computes tables of travel time, ray angle, ray parameter, and vertical slowness at the source as a function of source depth and source-receiver distance. It can be used for both local and global seismic models because an earth-flattening transformation is applied to the velocity model prior to the ray tracing. The output tables are designed to be read with the GET_TTS subroutine in the main program. deptable.f will give results only for source depths that correspond to a specified depth in the input model file. If necessary, the vzfillin.f program should be used to resample the input model to a finer depth sampling before running deptable.f. The maximum depth input can be used if a reflected phase, such as PmP or PcP, is desired. Source depths either can be specified exactly or as a range of equally spaced depths. All of these depths must correspond to a line in the input velocity model.

The minimum ray parameter is always set to zero so that vertically traveling rays from events at depth are included. The maximum value is set to the reciprocal of the surface velocity in the model.

Unless speed is important, a large number of rays should be used, up to a maximum of 40,000 rays. If desired, the ray table output file gives the surface-to-surface distance and time results for all values of the ray parameter. This may be useful in some cases for debugging and other purposes.

The ray angle and slowness tables are not used by COMPLOC but are included for use in focal mechanism or other studies that require the ray takeoff angle at the source. The output ray angles at the source are from vertical: $0°$ is upgoing vertical, $90°$ is horizontal, $135°$ is downgoing at a $45°$ angle, etc. The output values of ray parameters are negative for upgoing rays from the source and positive for downgoing rays from the source.

The program only outputs the first-arriving branches of triplicated phases. Because Pn and Sn are so weak in most local earthquake data sets, these phases can be suppressed by giving a suitable value for the minimum ray parameter at long range. This results in tables that include Pg out to ranges beyond the Pg/Pn crossover distance. The results are only approximate for layer cake (constant velocity layer) models because the results are interpolated between adjacent values of ray parameter p. However, when a large number of rays are used, the inaccuracies are relatively small.

4.2.3 getstlist

getstlist.f converts the station lists from the SCSN and NCSN web sites into the format needed by comploc.f, which consists of station names, their locations and station corrections (if available).

For example:

CI BAR EHZ 32.68005 -116.67215 496.0 0.00 0.00

where CI is the network identification, BAR is the station name, EHZ is the component, 32.68005 is the station latitude, -116.67215 is the station longitude, 496.0 is the station elevation in meters, and 0.00 and 0.00 are the P and S timing corrections (if available). This is a fixed column format; users must put everything in the correct columns. comploc.f uses only the network identifications and station names to identify and locate stations.

4.2.4 phase2bed3

We recommend converting the phase data file from the network into our binary BED3 format, which is much faster to read than ASCII phase formats, especially for large data sets. We provide phase2bed3.f, which is a Fortran77 program that can convert SCSN STP phase data and NCSN HYPOINVERSE phase data into the BED3 format.

4.2.5 comploc

comploc.f is the Fortran77 program that implements the source-specific location method. Before running comploc.f, the P and S travel time table files, the station location file, and the phase pick file must be available.

First, the program asks for the required input file names. The phase data are permitted in one of the three different formats: (1) our binary BED3 format, (2) SCSN STP format, and (3) HYPOINVERSE format. Five different output formats for the locations are permitted: (1) SCSN format, (2) HYPOINVERSE format, (3) NCEDC readable format, (4) HYPO71 format, and (5) our own special format.

The distance cutoff permits rejection of phase data from stations beyond a maximum distance (km) from the event. Often data at longer distances are less reliable due to Pg/Pn ambiguities or defects in the velocity model. We have generally used a 100-km cutoff for our California location work. Comparing results using different distance cutoffs is a good test of the velocity model. If the event depths change significantly when a 50-km cutoff is used compared with a 100-km cutoff, then the mid- to lower- crustal velocities in the model likely are too fast or too slow. A clue that this may be happening is when a mainshock locates at a different depth from its aftershocks; larger events typically have phase picks extending to larger distances than smaller events.

A minimum number of phase picks is required in order to locate an event. Obviously at least four picks are required to solve for (x, y, z, t). We recommend setting this to five or more. Larger numbers will restrict the locations to only the better-recorded events. A lat/lon window option permits locating a geographic subset of your dataset. Units are decimal degrees, with negative numbers for west longitudes, *i.e.*, California is at $-120°$ longitude.

If desired, the locations can be fixed to their starting locations. Normally, this option should not be used as it does not produce new locations. The fixed location kluge option permits keeping the location fixed at the (x, y, z) location given in the phase file. The program will then only vary the origin time of the events to achieve the best fit. This option can be useful to compute station terms for a given set of locations with respect to a particular 1-D velocity model. For example, if one has locations available from a joint-hypocenter velocity (JHV) inversion that are believed to be accurate, this option can be used to compute a set of station terms that will yield similar absolute locations using the comploc.f program for a 1-D model (this will require a separate run of comploc.f using the station terms as input). The advantage is that additional events (not in the JHV catalog) can be located and the SSST method should improve the relative location accuracy of all of the events.

The starting reference depth is the center point for the grid search method. If a fixed depth is used, then another input line is required to specify the depth. In general the locations are not sensitive to the starting depth, but we have found some dependence for a small fraction of the events, which apparently have complicated misfit functions with multiple local minima. A good starting depth for most crustal seismicity is 10 km, because the grid search method starts with a box of ± 10 km.

For testing purposes, the user can locate fewer than the total number of events by specifying a maximum number of events to locate, or specifying a random fraction of the total events to locate. For example, entering 0.1 for the random fraction would cause the program to randomly select 10$\%$ of the input events.

The user can select either the L1- or L2-norm for the residual misfit function. We have found that the L1-norm gives somewhat better results for real data, presumably because of its robustness with respect to outliers. The program works by performing a number of iterations of event location and station term calculations. There are two types of station terms. Static station terms are a single number for each station and phase (P or S). They are computed as the mean (or median in the case of the L1-norm option), of the residuals for each station. The source-specific station terms (SSST) are specific to each event and are computed by smoothing the residuals over adjacent events. The best results generally are obtained by first solving for static station terms and then solving for source-specific station terms using a residual smoothing box that decreases in size with each iteration. The program permits the user to vary the number of iterations used at each step and the size of the smoothing box for the SSST calculation.

An example data set from the Vallecitos Valley region of California (see Figures 3 and 4 from Shearer *et al.* 2005) also is included with the package. Because of the number of required inputs, we recommend always running comploc.f using a UNIX script, which is included as a "do" file in the example. In Figure 4.1 and 4.2, we show the map-view and cross section of the different locations for the Vallecitos Valley region from COMPLOC. Figure 4.1a and 4.2a are the SCSN catalog locations. Figure 4.1b and 4.2b are the single event locations when we set the number of iterations for both the static station terms and the source-specific station terms to zero. Figure 4.1c and 4.2c are the static station term locations where the number of iterations for the source-specific station terms is zero and the station term for each station is a constant. Figure 4.1d and 4.2d are the shrinking box location where we shrink the size of the smoothing box from 20 km at the first iteration to 8 km at the last iteration. The locations are slightly better than the static station term locations, although because this example is for a compact cluster, most of the location improvement compared to the single event locations is seen using the static station terms alone. When the method is applied to more distributed seismicity, the static station term locations are significantly less accurate than the SSST locations.

In the cross-section location plot, some events are stuck at 6 km even in the shrinking box location. This is probably due to the linear interpolation we use to compute travel times, which may result in slight second-order discontinuities (*i.e.*, changes in slope) at points in our travel-time tables. It is possible that higher-order interpolation algorithms could solve this problem (Richards-Dinger and Shearer, 2000).

The recommended user sequence for our COMPLOC package is:

1. Create v_z model and run vzfillin.f to resample to 1-km (or 0.5-km) depth intervals;

2. Run deptable.f to create the tables necessary for comploc.f;

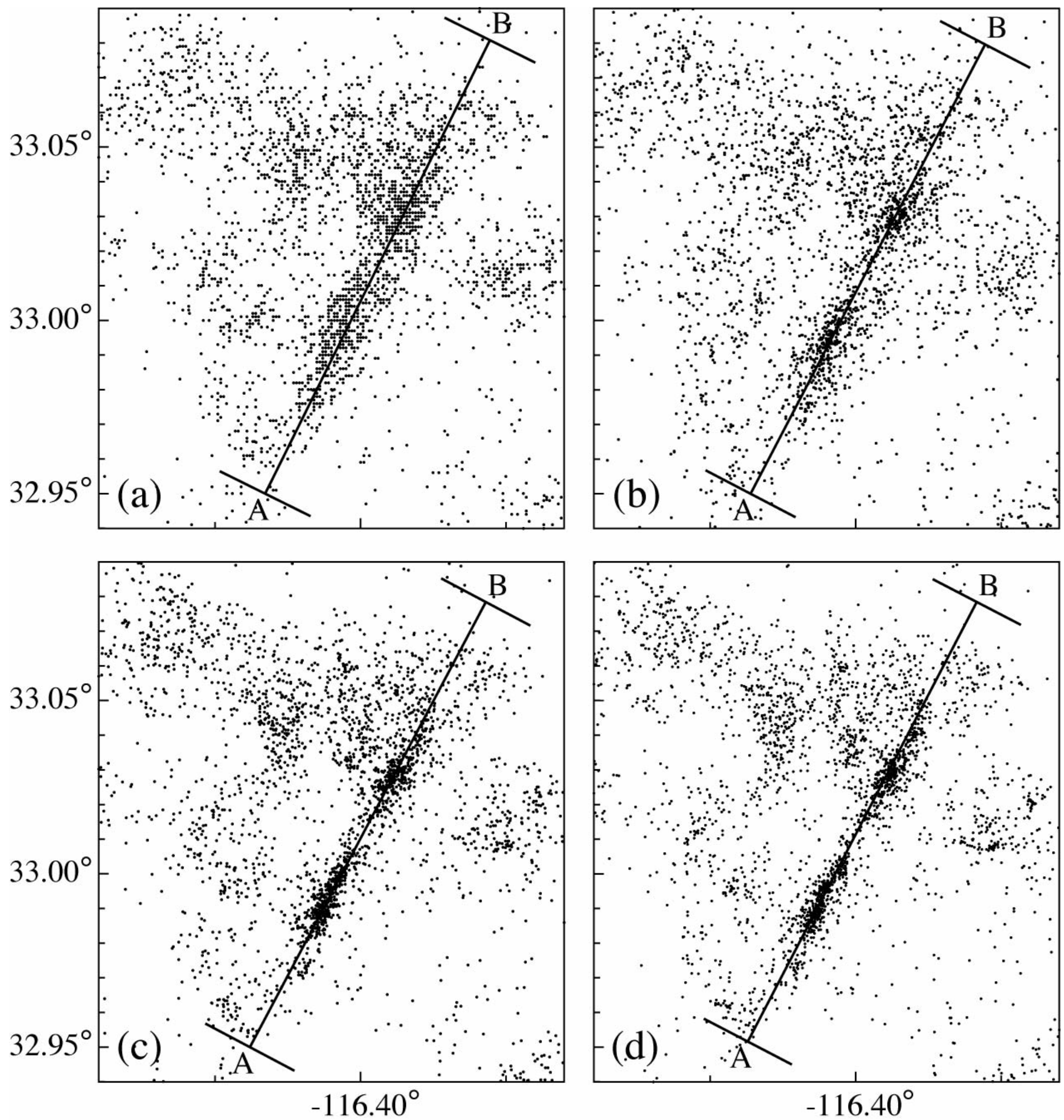

Figure 4.1. Map view of the relocated seismicity near Vallecitos Valley, comparing: (a) SCSN catalog locations, (b) single event locations, (c) static station term locations, and (d) shrinking box SSST locations. The line AB shows the cross section for Figure 4.2.

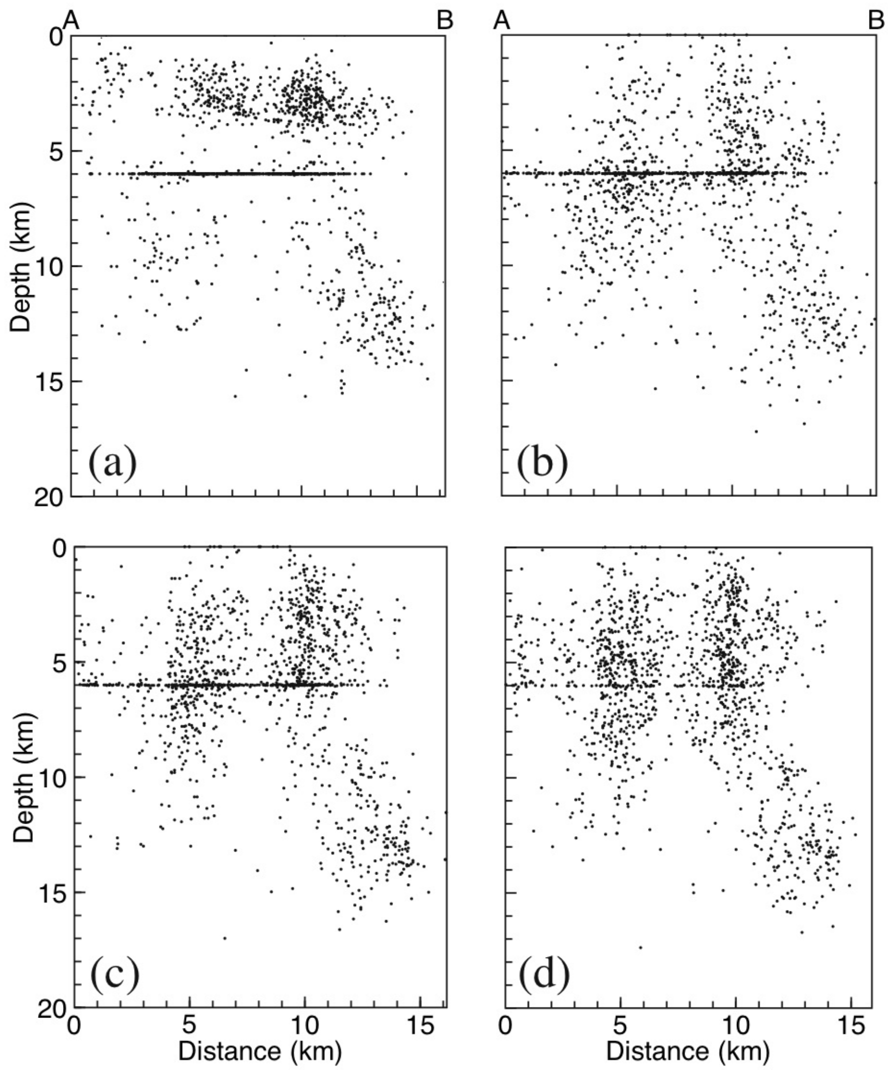

Figure 4.2. Cross-sections of the relocated seismicity along the profile AB (shown in Figure 4.1) near Vallecitos Valley, comparing: (a) SCSN catalog locations, (b) single event locations, (c) static station term locations, and (d) shrinking box SSST locations.

3. Use phase2bed3.f to convert phase pick data to BED3 format;

4. Run comploc.f to compute locations.

4.3 Summary

The advantages of COMPLOC include:

1. The grid search approach allows application of more-robust norms than least squares, which are less sensitive to gross picking or timing errors.

2. The input 1-D velocity model is parameterized in terms of continuous gradients between depth points rather than being restricted to “layer cake” models with constant velocity layers.

3. Large data sets can be rapidly input using the binary BED3 option. However, ASCII STP and HYPOINVERSE phase formats also are supported.

4. The shrinking-box source-specific station term (SSST) method (Lin and Shearer, 2005) greatly improves the relative location accuracy among nearby events. It achieves results comparable to the double-difference method but runs faster for large data sets.

The limitations of COMPLOC include:

1. Starting location estimates must be provided.

2. The current release does not permit use of waveform cross-correlation differential times.

The initial and future releases of the COMPLOC package are available at:

http://igpphome.ucsd.edu/∼glin/COMPLOC

4.4 Acknowledgments

We thank Editor Susan E. Hough for constructive comments. Funding for this research was provided by NEHRP/USGS grant 03HQPA0001. This research was also supported by the Southern California

Earthquake Center, which is funded by NSF Cooperative Agreement EAR-0106924 and USGS Cooperative Agreement 02HQAG0008. The SCEC contribution number for this paper is 974.

4.5 References

Jordan, T. H. and K. A. Sverdrup (1981). Teleseismic location techniques and their application to earthquake clusters in the south-central Pacific. *Bull. Seismol. Soc. Am.*, **71**, 1105–1130.

Lin, G. and P. M. Shearer (2005). Tests of relative earthquake location techniques using synthetic data. *J. Geophys. Res.*, **110**, B04304, doi: 10.1029/2004JB003380.

Richards-Dinger, K. B. and P. M. Shearer (2000). Earthquake locations in southern California obtained using source-specific station terms. *J. Geophys. Res.*, **105**, 10,939–10,960.

Shearer, P. M., E. Hauksson and G. Lin (2005). Southern California hypocenter relocation with waveform cross-correlation, Part 2: results using source-specific station terms and cluster analysis. *Bull. Seismol. Soc. Am.*, **95**, 904–915.

Waldhauser, F. and W. L. Ellsworth (2000). A double-difference earthquake location algorithm: method and application to the Northern Hayward Fault, California. *Bull. Seismol. Soc. Am.*, **90**, 1353–1368.

Waldhauser, F. and W. L. Ellsworth (2002). Fault structure and mechanics of the Hayward Fault, California, from double-difference earthquake locations. *J. Geophys. Res.*, **107**, 2054, doi: 10.1029/2000JB000084.

The text of this chapter, in full, is a reformatted version of the material as it appears in Lin, G. and P. M. Shearer, The COMPLOC Earthquake Location Package, *Seismological Research Letter, v. 77, No. 4*, 2006. The dissertation author was the primary researcher and author. The co-author directed and supervised the research which forms the basis of this chapter. The original paper is copyrighted by the Seismological Society of America, and the material is included here by permission of SSA.

Chapter 5

Estimating Local V_p/V_s Ratios Within Similar Earthquake Clusters

Abstract. We develop and test a method to estimate local V_p/V_s ratios for compact similar earthquake clusters using the precise P and S differential times obtained using waveform cross-correlation. We demonstrate how our technique works using synthetic data and evaluate likely errors arising from near-source takeoff angle differences between P and S waves. We use a robust misfit function method to compute V_p/V_s ratios for both synthetic data sets and several similar event clusters in southern California, and use a bootstrap resampling approach to estimate standard errors for real data. Our technique has higher resolution for near-source V_p/V_s ratios than typical tomographic inversion methods and provides constraints on near-fault rock properties.

5.1 Introduction

Recently, waveform cross-correlation has become an increasingly important tool for improving relative earthquake locations, characterizing event similarity and studying earthquake source properties (e.g., Nakamura, 1978; Poupinet *et al.*, 1984; Got *et al.*, 1994; Dodge *et al.*, 1995; Nadeau *et al.*, 1995; Gillard *et al.*, 1996; Shearer, 1997, 1998; Rubin *et al.*, 1999; Waldhauser *et al.*, 1999; Astiz *et al.*, 2000; Astiz and Shearer, 2000; Shearer, 2002; Shearer *et al.*, 2003; Hauksson and Shearer, 2005; Schaff and Waldhauser, 2005; Shearer *et al.*, 2005). Relative earthquake locations have been remarkably improved by using the very precise differential travel times obtained from waveform cross-correlation, which can often be measured to millisecond precision for similar events, allowing relative earthquake location to be precise to a few meters. In most of these studies, the relative locations are obtained by using a fixed seismic velocity model, although recently the differential times have also been used to constrain tomographic inversions (Zhang and Thurber, 2003).

Here we show that when both P- and S-wave differential times are available, it is possible to estimate the local P-to-S velocity ratio within individual similar event clusters in addition to improving the relative locations among the events. Phillips *et al.* (1992) presented a similar technique for microearthquake cluster structure studies but have not yet published the details of their method. We demonstrate that in many cases reasonable V_p/V_s estimates can be obtained even given uncertainties in the P- and S- takeoff angles. Finally, we use a robust fitting method to handle the outliers that are often present in real data and apply bootstrap resampling to evaluate likely errors. We test our approach on both synthetic data and waveform cross-correlation data for similar event clusters in southern California.

5.2 Theory

We begin by considering an idealized example of a single pair of events and then systematically add the complexities associated with more realistic geometries.

5.2.1 Obtaining the V_p/V_s Ratio for a Single Pair of Events

Consider a pair of nearby events, event 1 and event 2, recorded at n stations. If the event separation is small enough compared with the source-receiver distances, the differential P-wave travel time δT_p^i between these two events at station i can be expressed as

$$\delta T_p^i = T_{p_2}^i - T_{p_1}^i = \frac{\delta l_p^i}{V_p} \tag{5.1}$$

where $T_{p_2}^i$ and $T_{p_1}^i$ are the source-receiver travel times for events 2 and 1, respectively, δl_p^i is the difference in the ray-path distances between the two events, and V_p is the local P-wave velocity (see Figure 5.1). Note that because of source-receiver reciprocity this travel-time difference is identical with that resulting from a source at the station generating a wavefront that is recorded at the two event locations. We assume that the events are sufficiently close together that the seismic velocity is locally constant and that the P- reciprocal wavefront from each station may be approximated as planar. Because the stations are in different directions, the δl_p^i values will vary among the stations.

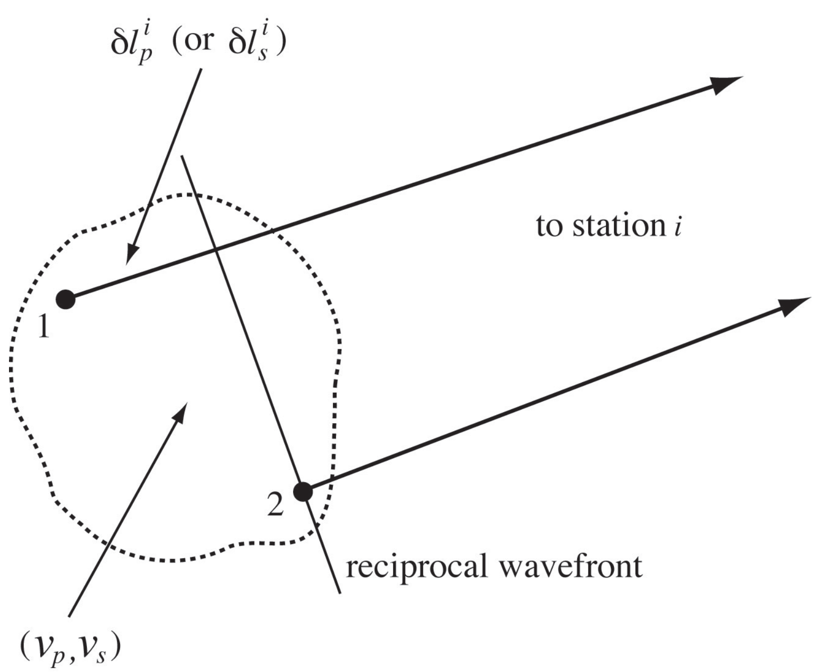

Figure 5.1. The ray geometry for a pair of events recorded by a distant station.

Under similar assumptions, the differential S travel time may be expressed as

$$\delta T_s^i = T_{s_2}^i - T_{s_1}^i = \frac{\delta l_s^i}{V_s} \tag{5.2}$$

Provided that the P- and S- ray paths are coincident (we will discuss this assumption in greater detail in a later section), then $\delta l_p^i = \delta l_s^i$ and

$$\frac{V_p}{V_s} = \frac{\delta T_s^i}{\delta T_p^i} \tag{5.3}$$

and we could estimate the local V_p/V_s ratio near the events separately from the δT_s^i and δT_p^i times. Given a number of different stations, the $(\delta T_p^i, \delta T_s^i)$ points ($i = 1, 2, 3, ..., n$) should all lie on the $\delta T_s = (V_p/V_s)\delta T_p$ line.

However, we do not normally measure the travel times, T, because we do not know the event origin times. Instead, we measure the arrival times, t. Let δt_0 be the difference in origin times between these two events, that is,

$$\delta t_0 = t_{0_2} - t_{0_1} \tag{5.4}$$

where t_{0_2} is the origin time of event 2 and t_{0_1} is the origin time of event 1. Then for station i, $t_{p_1}^i = t_{0_1} + T_{p_1}^i$, $t_{p_2}^i = t_{0_2} + T_{p_2}^i$, and

$$t_{p_2}^i - t_{p_1}^i = (t_{0_2} + T_{p_2}^i) - (t_{0_1} + T_{p_1}^i) \tag{5.5}$$

$$= (t_{0_2} - t_{0_1}) + (T_{p_2}^i - T_{p_1}^i) \tag{5.6}$$

and we have $\delta t_p^i = \delta t_0 + \delta T_p^i$ or $\delta T_p^i = \delta t_p^i - \delta t_0$. Similarly for the S-waves we have $\delta T_s^i = \delta t_s^i - \delta t_0$, and thus

$$\frac{V_p}{V_s} = \frac{\delta t_s^i - \delta t_0}{\delta t_p^i - \delta t_0} \tag{5.7}$$

The effect of the difference in origin times, δt_0, is to shift the $(\delta T_p^i, \delta T_s^i)$ points in both coordinates by δt_0 or along a 45° line. Figure 5.2 shows the relation between $(\delta t_p^i, \delta t_s^i)$ and $(\delta T_p^i, \delta T_s^i)$.

Equation (5.7) can be rewritten in the slope-intercept form

$$\delta t_s^i = (\frac{V_p}{V_s})\delta t_p^i + \delta t_0(1 - \frac{V_p}{V_s}) \tag{5.8}$$

and we see that the $(\delta t_p^i, \delta t_s^i)$ points are on a line with slope V_p/V_s and *y* intercept $\delta t_0(1 - V_p/V_s)$ (shown in Figure 5.2). Notice that the $\delta t_0(1 - V_p/V_s)$ term does not contain additional constraints on the V_p/V_s ratio because δt_0 is not known *a priori*. Thus, the $(\delta t_p, \delta t_s)$ points for a single pair of events recorded by many stations should form a line with a slope that provides the V_p/V_s ratio and a *y* intercept that gives the differential origin time. If noise or picking errors are present, then some kind of fitting procedure will be necessary to determine the best-fitting slope and estimate the V_p/V_s ratio. Note that this method can only be used to solve for local V_p/V_s ratios, not the absolute P- or S-wave velocity, unless δl_p^i or δl_s^i is independently known (e.g., Fitch, 1975). In general, these event separation distances and the overall size of an event cluster trade off with the local P or S velocity. However, in principle the V_p/V_s ratio can be recovered even without accurate event locations as we demonstrate here.

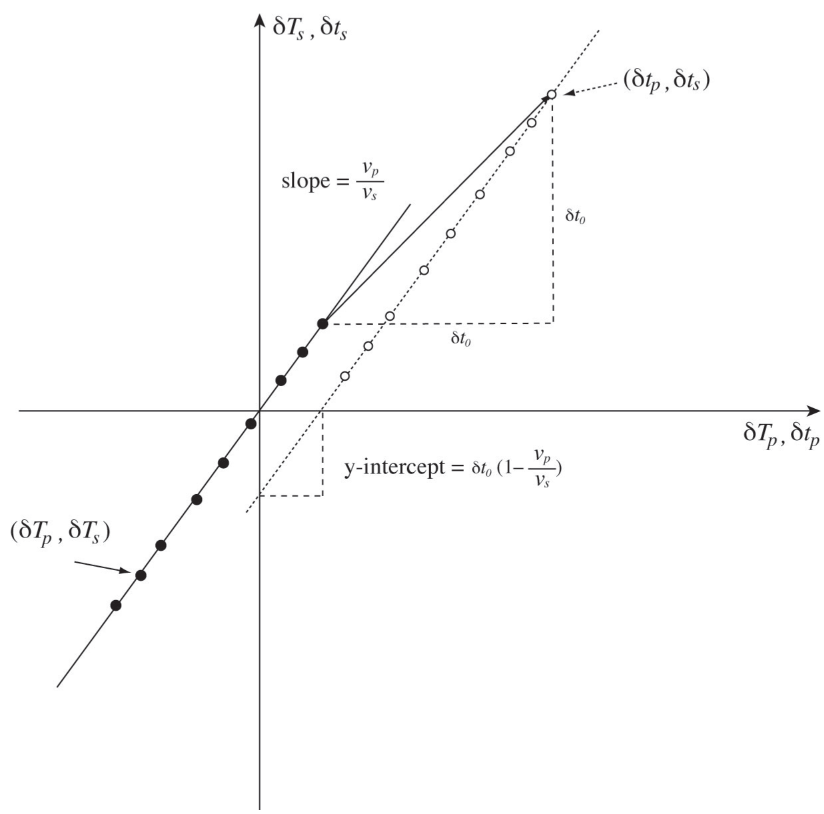

Figure 5.2. The filled circles show the differential P and S *travel* times and the open circles indicate the differential P and S *arrival* times, which are shifted δt_0 in both coordinates from the P and S travel-time line. The slopes of both lines are the local V_p/V_s ratio. The travel-time line passes through the origin $(0, 0)$, and the arrival-time line has a *y* intercept of $\delta t_0(1 - V_p/V_s)$.

Next, we use synthetic data to illustrate the technique. We perform our synthetic tests in a $64 \times 64 \times 32$ km uniform half-space with a P-wave velocity of 6 km/s and a V_p/V_s ratio of 1.732. We generate a single pair of events separated by 0.2 km with their center at 10 km depth and 20 random station locations on the surface of the half-space. We compute the differential times from this event pair to all 20 stations and use these differential times to estimate the local V_p/V_s ratio. For simplicity, we do not add any noise for this example. Figure 5.3 shows the synthetic differential times, which, as expected define a line of slope 1.732.

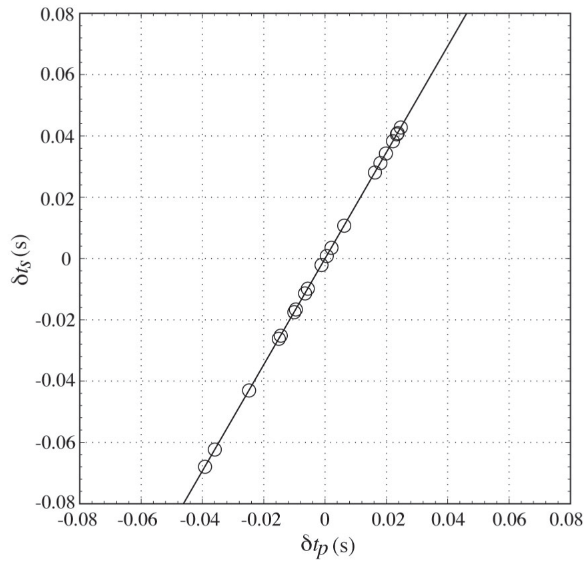

Figure 5.3. P differential arrival times versus S differential arrival times for a single pair of events recorded by 20 random stations on the surface. The straight line passing through the points is the best-fitting line from our iterative total least-squares method. The slope of the line is 1.732, which is the true V_p/V_s ratio in our test.

5.2.2 V_p/V_s Ratio for a Cluster of Events

For a single pair of events, equation (5.8) works directly because the *y* intercept, $\delta t_0(1 - V_p/V_s)$, is a constant for all the records. But for different pairs of events, it is not appropriate to use equation (5.8) because the differential origin times are not the same. In other words, for all pairs of events in a compact cluster, assuming they all have the same local V_p/V_s ratios, if we plot all the (δt_p, δt_s) points on one single plot, they will lie on different straight lines parallel to each other at slope V_p/V_s, but with different *y* intercepts.

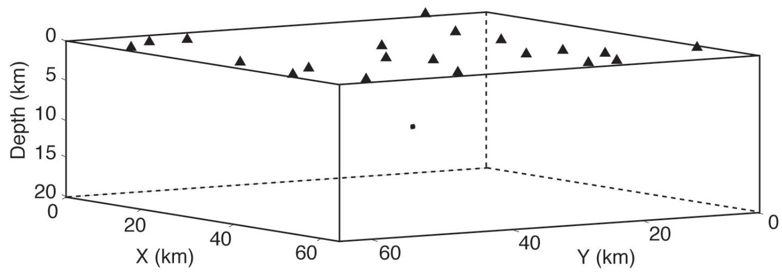

Figure 5.4. Event and station distributions for the 27 synthetic events in a cube and 20 stations on the surface. The small dot in the middle of the half-space is the cube of events, which is hard to distinguish because the size of the cube is $0.2\times0.2\times0.2$ km. The triangles are the stations.

This is illustrated in another synthetic example. In this case, we continue using a uniform half-space model with a P-wave velocity of 6 km/s and a V_p/V_s ratio of 1.732. We generate 20 random station locations on the surface of the half-space and 27 events with random origin times in a compact $0.2\times0.2\times0.2$ km cube with the center at 10 km depth. Figure 5.4 shows the event and station distributions for this test. We compute all possible differential times from each pair of events to the 20 stations (at this stage we still do not include any noise). Figure 5.5a shows the (δt_p, δt_s) points for different pairs of events. For plotting purposes, we only plot the points with absolute values less than 0.05 s. These points are on different lines parallel to each other at the slopes of the true V_p/V_s ratio (1.732) for the cube, but different *y* intercepts, which are due to the differing differential origin times between event pairs.

To estimate the local V_p/V_s ratio for the compact cube using the differential times from all available event pairs, we can use equation (5.8) to write a series of equations for each station that records the pair of events 1 and 2:

$$\delta t_s^1 = (\frac{V_p}{V_s})\delta t_p^1 + \delta t_0(1 - \frac{V_p}{V_s}) \qquad \text{for station 1} \tag{5.9}$$

$$\delta t_s^2 = (\frac{V_p}{V_s})\delta t_p^2 + \delta t_0(1 - \frac{V_p}{V_s}) \qquad \text{for station 2} \tag{5.10}$$

$$\vdots$$

$$\delta t_s^n = (\frac{V_p}{V_s})\delta t_p^n + \delta t_0(1 - \frac{V_p}{V_s}) \qquad \text{for station n} \tag{5.11}$$

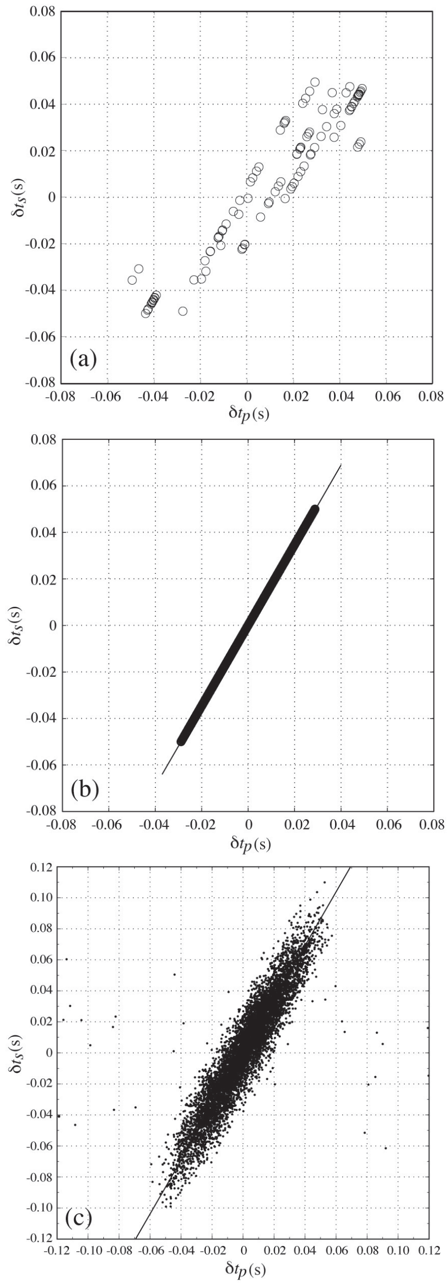

Figure 5.5. (a) P differential arrival times δt_p versus S differential arrival times δt_s for different pairs of events in a compact cluster. These points are on different lines parallel to each other, with the same slope as the true V_p/V_s ratio for the cluster, but with different y intercepts, which are due to the varying differential origin times. (b) Demeaned δt_p versus demeaned δt_s in (a). These points align on a straight line at slope V_p/V_s and through the origin $(0, 0)$. (c) Demeaned δt_p versus δt_s for 27 synthetic events using the uniform half-space velocity model. We add Gaussian distributed picking errors in both P and S differential times and also uniform distributed errors in P times to simulate the outliers in real data. The slope of the best-fitting straight line is 1.730, which is very close to the true V_p/V_s ratio for the cube.

If we sum these equations and divide by the number of stations n, we then have

$$\bar{\delta t_s} = (\frac{V_p}{V_s})\bar{\delta t_p} + \delta t_0(1 - \frac{V_p}{V_s}) \tag{5.12}$$

where $\bar{\delta t_s}$ and $\bar{\delta t_p}$ are the mean values of the differential S and P times from all the stations.

Subtracting (5.12) from (5.8), we obtain

$$(\delta t_s^i - \bar{\delta t_s}) = (\frac{V_p}{V_s})(\delta t_p^i - \bar{\delta t_p}) \tag{5.13}$$

$$\hat{\delta t}_s^i = (\frac{V_p}{V_s})\hat{\delta t}_p^i \tag{5.14}$$

where $\hat{\delta t}_s^i$ and $\hat{\delta t}_p^i$ are the demeaned differential S- and P- arrival times. In this way we can estimate the V_p/V_s ratio using the $\hat{\delta \mathbf{t}}_\mathbf{p}$ and $\hat{\delta \mathbf{t}}_\mathbf{s}$ vectors from all event pairs in the compact cluster. Because equation (5.14) is not a function of differential origin times, if we assume all pairs of events are in a compact cluster, all the ($\hat{\delta t}_p$, $\hat{\delta t}_s$) points in the cluster should align on a straight line at slope V_p/V_s and through the origin $(0, 0)$, as shown in Figure 5.5b. This makes it possible to fit all of the points simultaneously for the best-fitting V_p/V_s ratio for the entire cluster.

5.2.3 Fitting Method for Noisy Data

In the preceding synthetic examples we have not included any noise, so the data points directly define the line that gives the V_p/V_s ratio. However, real data will have some degree of error, which will require the use of a fitting method to compute the best-fitting line. In addition, our differential time data often have obvious outliers — extreme values that would severely bias any conventional least-square approach. We thus apply a more robust method, which measures distance using the L_2 norm for data misfits below some specified value, d_{max} (which in general will depend on the observations), and an L_1 norm for larger values. This hybrid $l_1 - l_2$ error measure was proposed by Huber (1973) and can be used to compute what we will term the *robust mean* of a distribution. For data with outliers, we use the robust mean to demean the differential S- and P- arrival times for each station as described previously.

In the classical least-squares (LS) line-fitting approach, one of the two measurements is assumed to be exact and free of error and a regression is performed to find the best-fitting line to the second measurement. For example, if the the data are given as (x, y) pairs and the error is assumed to be entirely in y, then we find the slope and y intercept that minimize the sum of the squares of the vertical (y) distances between the line and the data. In our case, however, we likely have errors in both the δt_s^i and δt_p^i values. If the x and y errors are assumed equal, then the optimal solution is given by the line with the minimum perpendicular distance to each point. Least-squares solutions to this problem are described in, for example, Jefferys (1981), Press *et al.* (1992), and Van Huffel (1997). In the case of unequal x and y errors, the problem can be rescaled to be equivalent to the equal error case. To account for outliers in our differential time measurements, we modify this method to be more robust. We perform a grid search for lines of different slopes, computing the best-fitting y intercept for each line from the robust mean of the perpendicular distances to each data point, after first scaling the δt_s^i values so that their expected variance matches that of the δt_p^i values.

As we will discuss subsequently, biases resulting from angular differences in the local P- and S- ray paths near the events will cause errors in the δt_s points to be R times greater than the errors in the δt_p points, where R is the V_p/V_s ratio. We thus multiply the data δt_s values by $1/R$ so that their expected error is similar in size to the δt_p error. Note, however, that any desired rescaling could be applied at this point if the relative variance of δt_p and δt_s measurements is known *a priori*. Because our method is solving for R, an iterative method is necessary. We assume a starting value for R, find the best-fitting line, and then replace R with its updated value ($R = R \times slope$) for the next iteration. This iterative algorithm converges after several (3 to 5) iterations, and the final R value is our estimate for the V_p/V_s ratio. For our synthetic tests with noise, we use 1.0 as an initial value for R to test the robustness of our method; but for real data, 1.732 would be a more reasonable starting value for the V_p/V_s ratio, and is used in our analysis of waveform cross-correlation results.

To test our fitting method, we generate a synthetic data set for the 27 events in a cube and 20 stations on the surface using the same uniform half-space velocity model in the previous example. We add Gaussian distributed noise with zero mean and a standard deviation of 5 msec, which is comparable to the size of the scatter in real cross-correlation data, for the P differential times and scaled by 1.732 (the true V_p/V_s ratio) for the S differential times. To simulate the outliers in real data, we also add uniform distributed noise in 1% of the P differential times. To show that our iterative method works correctly even if the initial R estimate is incorrect, we assume $R=1$ in the first iteration. We test different initial values for R (between 0.1 and 10) in our study and find they all converge to the same V_p/V_s ratio for this synthetic example. Figure 5.5c shows the resulting data points and our V_p/V_s ratio estimate of 1.730. If we used the classical least-squares approach rather than our robust method, the estimated V_p/V_s ratio is 1.583. If the errors in the δt_p and δt_s points are assumed to be equal, then the robust total least-squares result is biased and we obtain a V_p/V_s ratio of 1.784 for this example.

5.2.4 Effect of Different Takeoff Angles for P and S

So far we have been assuming that the P and S waves are coincident so that they have the same takeoff angles. Now we consider the possible errors that may result if the P- and S- takeoff angles are different. This might be caused by depth-varying V_p/V_s differences or by local V_p/V_s variations near the source pair.

First, let us consider the effect that ray-path deviations will have on our δt_p and δt_s measurements. The ray-angle geometry at the event pair is shown in Figure 5.6. Let $\hat{\mathbf{a}}_p$ be the P-ray unit direction vector, $\hat{\mathbf{a}}_s$ be the S-ray unit direction vector, 2ε be the angle between $\hat{\mathbf{a}}_p$ and $\hat{\mathbf{a}}_s$, and $\hat{\mathbf{e}}$ be the unit direction vector from event 1 to event 2. Without loss of generality we may assume that $\hat{\mathbf{a}}_p$ and $\hat{\mathbf{a}}_s$ are in the x-z plane and symmetric about the z-axis. We can then write

$$\hat{\mathbf{a}}_p = (-\sin\varepsilon, 0, \cos\varepsilon) \tag{5.15a}$$

$$\hat{\mathbf{a}}_s = (\sin\varepsilon, 0, \cos\varepsilon) \tag{5.15b}$$

$$\hat{\mathbf{e}} = (\sin\theta\cos\phi, \sin\theta\sin\phi, \cos\theta) \tag{5.15c}$$

where the event vector $\hat{\mathbf{e}}$ has an arbitrary orientation defined by the polar angle θ and the azimuthal angle

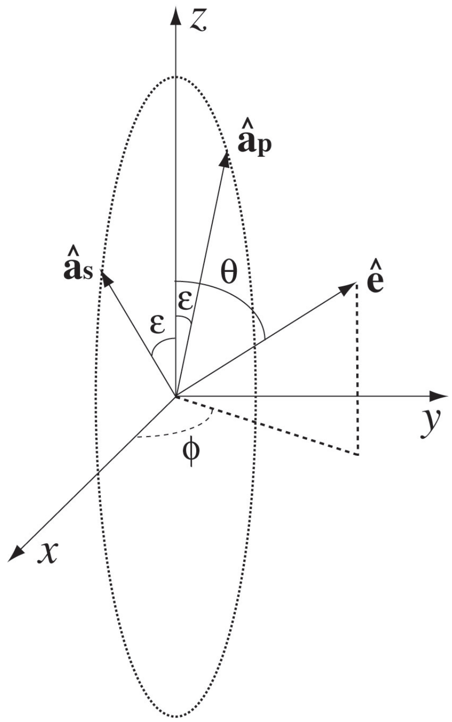

Figure 5.6. The spherical coordinate system that we use to show the bias in δt_p and δt_s due to ray path deviations.

ϕ. Let β_p be the angle between $\hat{\mathbf{a}}_p$ and $\hat{\mathbf{e}}$, and β_s be the angle between $\hat{\mathbf{a}}_s$ and $\hat{\mathbf{e}}$. We then have

$$\cos\beta_p \;=\; \hat{\mathbf{a}}_p\cdot\hat{\mathbf{e}} = -\sin\varepsilon\sin\theta\cos\phi + \cos\varepsilon\cos\theta \tag{5.16a}$$

$$\cos\beta_s \;=\; \hat{\mathbf{a}}_s\cdot\hat{\mathbf{e}} = \quad\sin\varepsilon\sin\theta\cos\phi + \cos\varepsilon\cos\theta \tag{5.16b}$$

We can express the differential P and S travel times as

$$\delta t_p \;=\; (\hat{\mathbf{a}}_p\cdot\mathbf{e})/V_p = (\|\mathbf{e}\|\,\hat{\mathbf{a}}_p\cdot\hat{\mathbf{e}})/V_p = (\|\mathbf{e}\|\,\cos\beta_p)/V_p \tag{5.17a}$$

$$\delta t_s \;=\; (\hat{\mathbf{a}}_s\cdot\mathbf{e})/V_s = (\|\mathbf{e}\|\,\hat{\mathbf{a}}_s\cdot\hat{\mathbf{e}})/V_s = (\|\mathbf{e}\|\,\cos\beta_s)/V_s \tag{5.17b}$$

where $\|\mathbf{e}\|$ is the distance between event 1 and event 2 (i.e., $\mathbf{e} = \|\mathbf{e}\|\,\hat{\mathbf{e}}$). Thus, each $(\delta t_p, \delta t_s)$ point can be written as

$$\begin{aligned}(\delta t_p, \delta t_s) \;&=\; \|\mathbf{e}\|\left(\frac{\cos\beta_p}{V_p}, \frac{\cos\beta_s}{V_s}\right)\\ &=\; \|\mathbf{e}\|\left(\frac{\cos\varepsilon\cos\theta}{V_p} - \frac{\sin\varepsilon\sin\theta\cos\phi}{V_p}, \frac{\cos\varepsilon\cos\theta}{V_s} + \frac{\sin\varepsilon\sin\theta\cos\phi}{V_s}\right)\end{aligned} \tag{5.18}$$

When the P and S-ray paths are coincident (i.e., $\varepsilon = 0$), then the slope of the $(\delta t_p, \delta t_s)$ points is equal to V_p/V_s ratio. When ε is small but nonzero, then $\cos\varepsilon \approx 1$, so that δt_p and δt_s are biased from their $\varepsilon = 0$ values by $(\sin\varepsilon \sin\theta \cos\phi)/V_p$ and $(\sin\varepsilon \sin\theta \cos\phi)/V_s$, respectively. Thus, we see that the bias introduced into the δt_s differential times by ray-path deviations will be a factor V_p/V_s times larger than the bias in the δt_p times.

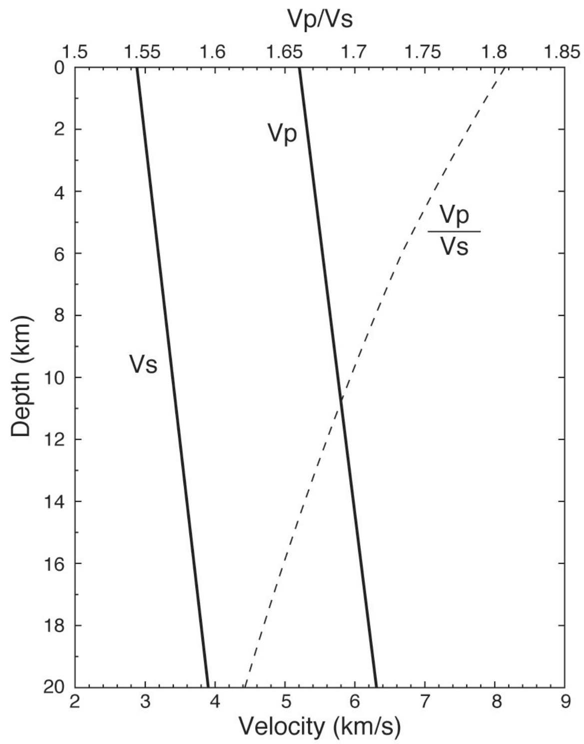

Figure 5.7. The velocity model that we use to test the effect of different P- and S-wave takeoff angles.

To show the effect of different P- and S-wave takeoff angles, we generate a velocity model in which both V_p and V_s increase, but the V_p/V_s ratio decreases with depth (see Figure 5.7). At 10 km source depth and 30 km epicentral distance, the P-takeoff angle at the source is $80.13°$ (from vertical) and the S-takeoff angle is $85.03°$. We use the depth-varying velocity model to generate differential times for a single pair of events separated by 0.2 km at 10 km depth with the event separation vector perpendicular to the surface, and recorded by 20 random stations at the surface. The epicentral distances range between 5 km and 38 km, most of which are about 30 km. In Figure 5.8, we plot (δt_p, δt_s) points for this pair of events. For the purpose of this test, we do not add any random noise to the differential times. The true local V_p/V_s ratio at the center of the events is 1.697, whereas the estimated slope is 1.830. The points are biased from the true straight line because the takeoff angles for P and S from each station are different.

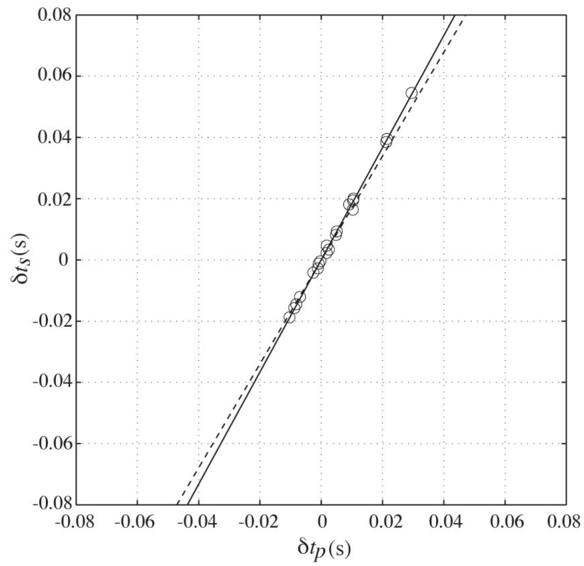

Figure 5.8. δt_p versus δt_s for a single pair of events recorded by 20 stations at the surface using the depth-varying velocity model of Figure 5.7. The estimated slope is 1.830, shown by the solid line, while the true local V_p/V_s ratio is 1.697, shown by the dashed line.

The bias in the estimated V_p/V_s ratio will vary depending on the orientation of the event pair with respect to the incoming rays. To illustrate this, we use the same depth-varying velocity model and station distribution, but rotate the relative location vector of the pair of events every 5° uniformly in three-dimensions while keeping the center of the events fixed. In this way, the P- and S-takeoff angles from each station to the pair of events change in all possible directions. We then use the (δt_p, δt_s) points from all these rotated pairs of events to estimate the slope.

Figure 5.9 shows all these points from the rotated event pairs and the best-fitting straight line. The slope of the best-fitting line is 1.697, which is the true V_p/V_s ratio at the center of the events. Thus, although P- versus S-takeoff angle differences will bias results for individual event pairs, this bias will tend to average out when a large number of random event orientations are present. This can be seen from symmetry considerations in Figure 5.6 and equation (5.18); for every $\hat{\mathbf{e}}_1$ vector with a positive V_p/V_s

bias, there will also exist a corresponding $\hat{\mathbf{e}}_2$ vector with negative bias at $\phi_2 = \phi_1 + \pi$.

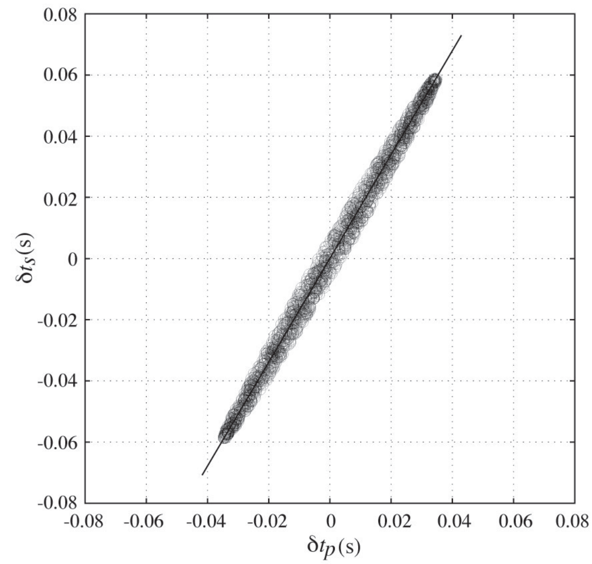

Figure 5.9. δt_p versus δt_s for the same station distribution and velocity model used in Figure 5.8. In this case, we rotate the pair of events every $5°$ uniformly in three-dimensions so that the ray paths from the stations change in all possible directions. For plotting purposes, we only plot a random 5% of the points. The estimated slope is 1.697, which is the true V_p/V_s ratio at the cluster depth.

For real data it is not possible to do the three-dimensional rotations. However, if an event cluster is small and contains event pairs of varying orientations and the station distribution is good enough, the ray paths for all the events in the cluster may form a random distribution of directions, as in the three-dimensional rotations, so that the local V_p/V_s ratio may be accurately recorded. To show this, we generate the synthetic differential times for the 27 events in the cube and 20 stations in the previous section using the same depth-varying velocity model. The V_p/V_s ratio at the center of the cube is 1.697. The event and station distributions are shown in Figure 5.4. The (δt_p, δt_s) points for this small cube are shown in Figure 5.10. The slope of the best-fitting straight line is 1.697, which is the true V_p/V_s ratio at the center of the cube.

However, it should be recognized that the bias may not be completely removed in the case of event clusters with a more limited distribution of events. For example, if the 27 events in this synthetic example are restricted to a horizontal plane, then the V_p/V_s ratio estimate is 1.716. If the events are located within a vertical plane, then the computed V_p/V_s ratio will vary between 1.677 and 1.689, depending on the azimuth of the plane. This suggests that the most accurate results for real data clusters will be obtained for clusters with a three-dimensional distribution of events.

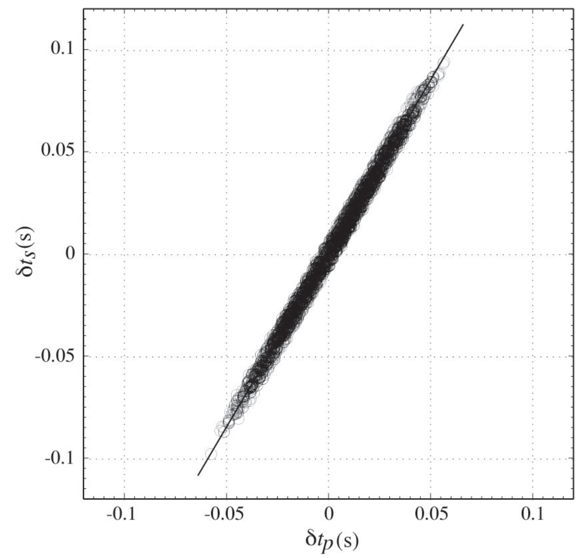

Figure 5.10. δt_p versus δt_s for 27 synthetic events using the velocity model shown in Figure 5.7. The slope of the best-fitting straight line is 1.697, which is the true V_p/V_s ratio for the cube.

As a final test of our V_p/V_s ratio estimate approach, we generate a synthetic data set for the 27 events in a cube and 20 stations on the surface using the same depth-varying velocity model in the previous example. We add Gaussian distributed noise with zero mean and standard deviations of 5 msec for the P differential times and scaled by 1.697 (the true V_p/V_s ratio) for the S differential times. To simulate the outliers in real data, we also add uniform distributed noise in 5$\%$ of the P differential times. Our V_p/V_s ratio estimate for this cube is 1.692 (shown in Figure 5.11), very close to the true value of 1.697. Note that the outliers in our test are very strong, which would significantly bias the ratio estimate if we used simple least-squares rather than our robust approach. The V_p/V_s ratio estimate from simple least-squares is 1.243 for this example. If the errors in the δt_p and δt_s points are assumed to be equal, then the robust total least-squares result is biased and we obtain a V_p/V_s ratio of 1.752.

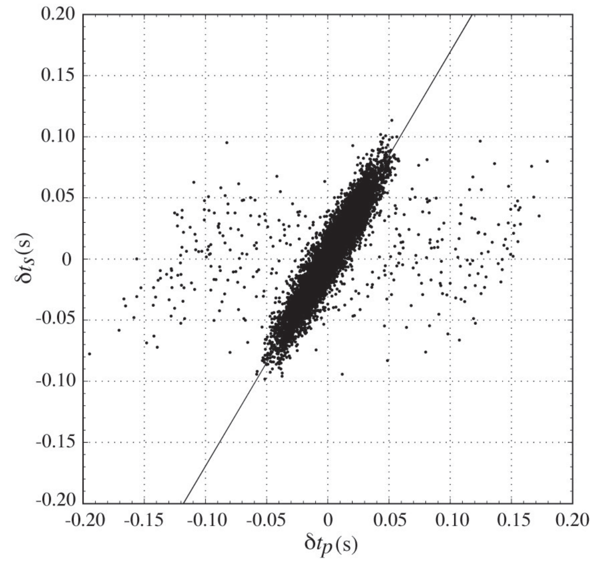

Figure 5.11. δt_p versus δt_s for 27 synthetic events using the velocity model shown in Figure 5.7. We add Gaussian distributed picking errors in both P and S differential times and also uniform distributed errors in P times to simulate the outliers in real data. The slope of the best-fitting straight line is 1.692, which is very close to the true V_p/V_s ratio for the cube.

5.3 Examples for Southern California Earthquake Clusters

We apply this V_p/V_s ratio estimate method to differential times from waveform cross-correlation for two similar event clusters in southern California taken from Shearer *et al.* (2005). To estimate the V_p/V_s ratio for each event cluster accurately, we use event pairs with at least five differential P-S times and require more than 100 differential P-S time pairs for the entire cluster.

5.3.1 Estimating Standard Errors

For real data, the event and station distributions may not be as good as in our synthetic data, so it is desirable to estimate standard errors in our V_p/V_s ratios. Since the true values are unknown, certain assumptions are necessary to obtain error estimates. The classical least-squares method can be used to compute error ellipses based upon χ^2 misfit criteria and is optimal for the case of uncorrelated Gaussian random errors. These methods are not easily generalized to other model norms, such as the robust least-squares method that is used here. As an alternative, we have applied a bootstrap approach (Efron and Gong, 1983; Efron and Tibshirani, 1991), in which each pair of suitable differential P and S times in the same cluster may be sampled multiple times or not sampled at all. This process is repeated for 100 subsamples for each cluster and we estimate the standard deviation of these 100 subsamples as the standard error of the V_p/V_s ratio. However, note that these formal statistical uncertainties (which can be quite small when the number of data points is large) represent a minimum error because they do not include the possible biases resulting from P and S takeoff angle differences in nonisotropic event distributions.

5.3.2 V_p/V_s Ratio Estimates Using Waveform Cross-Correlation Results

Here we present two examples of V_p/V_s ratio estimates using the waveform cross-correlation results for clusters in southern California taken from Shearer *et al.* (2005). Figure 5.12 shows the 7265 demeaned (δt_p, δt_s) points for cluster 99 (in the POLY5 subset of events) in southern California from Shearer *et al.* (2005). The centroid of this cluster is at (33.511°N, -116.555°E, 10.1 km). The slope of the best-fitting straight line is 1.782 and the standard deviation of our V_p/V_s ratio estimate from bootstrap resampling is 0.006. Figure 5.13 shows the 5520 demeaned (δt_p, δt_s) points for cluster 427 in POLY5. The centroid of this cluster is at (33.478°N, -116.495°E, 10.5 km). The resolved V_p/V_s ratio for this cluster is 1.713 and the standard deviation from bootstrap resampling is 0.010. In principle, these observed V_p/V_s ratios could be used to constrain the lithology of the rock in the source regions. As noted by Tatham (1982), laboratory and well-log data suggest a V_p/V_s ratio near 1.8 for dolomite and in the range of 1.6 to 1.75 for sandstones. However, the presence of cracks and the degree of pore fluid saturation can also be important factors in determining the V_p/V_s ratio.

5.4 Discussion

In general, variations in V_p/V_s ratios may be determined by using tomographic methods. However, the resolution of local V_p/V_s ratios from tomography is usually limited due to the coarse grid sizes, although Zhang and Thurber (2005) showed that the adaptive mesh tomography scheme has the ability to resolve the velocity structure near the source region. In this study, we develop a method to estimate

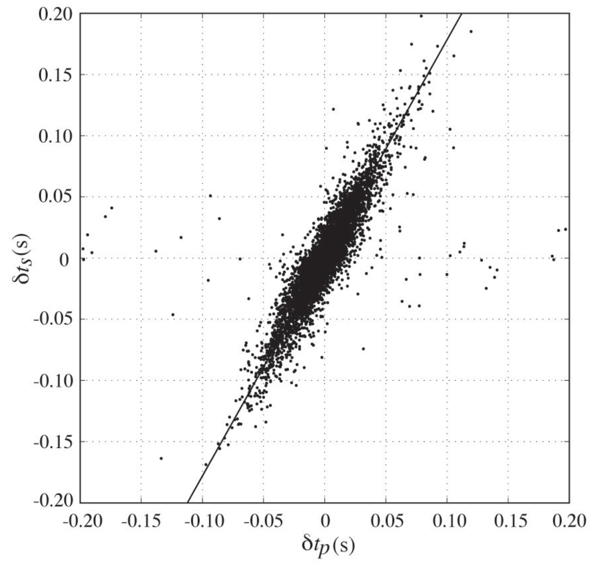

Figure 5.12. Demeaned δt_p versus δt_s for the 74 events in cluster 99 from the SHLK catalog (Shearer *et al.*, 2005). The slope of the best-fitting straight line is 1.782±0.006.

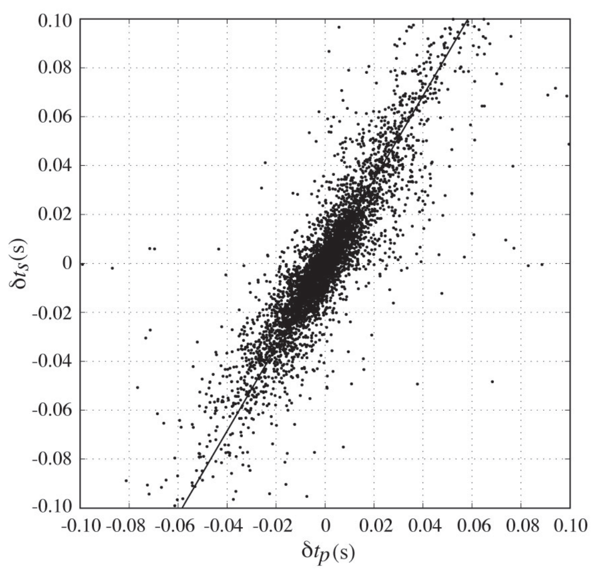

Figure 5.13. Demeaned δt_p versus δt_s for the 81 events in cluster 427 from the SHLK catalog (Shearer *et al.*, 2005). The slope of the best-fitting straight line is 1.713±0.010.

local V_p/V_s ratios for event clusters by using precise differential times derived from the waveform cross-correlation technique. Our method is simple to execute and does not require much computer power. The uncertainty is typically small since the precision of differential times from waveform cross-correlation can be as small as a millisecond and the V_p/V_s ratio can be recovered even without accurate event locations.

For real data, the $l_1 - l_2$ misfit measure is useful to reduce the effects of outliers. Due to possible differences in P- and S-wave takeoff angles, the estimated V_p/V_s ratios could be biased from their true values. However, as shown in our synthetic data tests, if the seismic ray coverage for a cluster of events is good enough, the true V_p/V_s ratio can still be recovered. We find that the resolved V_p/V_s ratios are very sensitive to the differential times, especially at short hypocentral distances where the P and S arrivals are very close to each other. In this case, the S waveforms should be windowed very carefully, because otherwise the V_p/V_s ratios will likely be underestimated because part of the P wavetrain may be included in the S-wave cross-correlation.

In this study, we assume that the scale length of changes in V_p/V_s ratios is greater than the size of the similar event clusters. Our method could be biased if there are significant variations in the V_p/V_s ratio within the cluster, although given a good distribution of events we should still obtain a reasonable value for the average V_p/V_s ratio. It is possible that spatial and/or temporal variations in V_p/V_s ratios could be identified by analyzing subsets of similar event clusters, but we do not attempt this here. Given recent applications of waveform cross-correlation to large earthquake catalogs (e.g., Hauksson and Shearer, 2005; Schaff and Waldhauser, 2005), widespread computation of near-source V_p/V_s ratios appears practical and should provide a useful complement to tomographic methods. In addition, these local V_p/V_s measurements should permit computing more accurate relative locations of events within each similar event cluster. We will defer discussing details of how this can be done to a later study.

5.5 Acknowledgments

We thank Egill Hauksson for his involvement in the waveform cross-correlation calculations and Jose Pujol, Nick Rawlinson, and Cliff Thurber for their detailed and constructive reviews. Funding for this research was provided by NEHRP/USGS grant 03HQPA0001. This research was also supported by the Southern California Earthquake Center, which is funded by NSF Cooperative Agreement EAR-0106924 and USGS Cooperative Agreement 02HQAG0008. The SCEC contribution number for this paper is 995.

5.6 References

Astiz, L. and P. M. Shearer (2000). Earthquake locations in the inner continental borderland, offshore southern California. *Bull. Seismol. Soc. Am.*, **90**, 425–449.

Astiz, L., P. M. Shearer and D. C. Agnew (2000). Precise relocations and stress change calculations for the Upland earthquake sequence in southern California. *J. Geophys. Res.*, **105**, 2937–2953.

Dodge, D. A., G. C. Beroza and W. L. Ellsworth (1995). Foreshock sequence of the 1992 Landers, California, earthquake and its implications for earthquake nucleation. *J. Geophys. Res.*, **100**, 9865–9880.

Efron, B. and G. Gong (1983). A leisurely look at the bootstrap, the jackknife and cross-validation. *Am. Statist.*, **37**, 36–48.

Efron, B. and R. Tibshirani (1991). Statistical data analysis in the computer age. *Science*, **253**, 390–395.

Fitch, T. J. (1975). Compressional velocity in source regions of deep earthquakes: an application of the master earthquake technique. *Earth Planet. Sci. Lett.*, **26**, 156–166.

Gillard, D., A. M. Rubin and P. Okubo (1996). Highly concentrated seismicity caused by deformation of Kilauea's deep magma system. *Nature*, **384**, 343–346.

Got, J.-L., J. Fréchet and F. W. Klein (1994). Deep fault plane geometry inferred from multiplet relative relocation beneath the south flank of Kilauea. *J. Geophys. Res.*, **99**, 15,375–15,386.

Hauksson, E. and P. Shearer (2005). Southern California hypocenter relocation with waveform cross-correlation, Part 1: results using the double-difference method. *Bull. Seismol. Soc. Am.*, **95**, 896–903.

Huber, P. J. (1973). Robust regression: asymptotics, conjectures and monte carlo. *Ann. Statist.*, **1**, 799–821.

Jefferys, W. H. (1981). On the method of least squares. II. *Astr. J.*, **86**, 149–155.

Nadeau, R. M., W. Foxall and T. V. McEvilly (1995). Clustering and periodic recurrence of microearthquakes on the San Andreas Fault at Parkfield, California. *Science*, **267**, 503–507.

Nakamura, Y. (1978). A_1 moonquakes: source distribution and mechanism. *Proc. Lunar Planet. Sci. Conf.*, **9**, 3589–3607.

Phillips, W. S., L. S. House and M. C. Fehler (1992). Vp/Vs and the structure of microearthquake clusters. *Seism. Res. Lett.*, **63**, 56–57.

Poupinet, G., W. L. Ellsworth and J. Frechet (1984). Monitoring velocity variations in the crust using earthquake doublets: an application to the Calaveras Fault, California. *J. Geophys. Res.*, **89**, 5719–5732.

Press, W. H., S. A. Teukolsky, W. T. Vetterling and B. Flannery (1992). *Numerical Recipes in Fortran 77: The Art of Scientic Computing*. Second Ed., Cambridge University Press, Cambridge.

Rubin, A. M., D. Gillard and J.-L. Got (1999). Streaks of microearthquakes along creeping faults. *Nature*, **400**, 635–641.

Schaff, D. P. and F. Waldhauser (2005). Waveform cross-correlation-based differential travel-time measurements at the Northern California Seismic Network. *Bull. Seismol. Soc. Am.*, **95**, 2446–2461.

Shearer, P. M. (1997). Improving local earthquake locations using the L1 norm and waveform cross correlation: application to the Whittier Narrows, California, aftershock sequence. *J. Geophys. Res.*, **102**, 8269–8283.

Shearer, P. M. (1998). Evidence from a cluster of small earthquakes for a fault at 18 km depth beneath Oak Ridge, southern California. *Bull. Seismol. Soc. Am.*, **88**, 1327–1336.

Shearer, P. M. (2002). Parallel fault strands at 9-km depth resolved on the Imperial Fault, southern California. *Geophys. Res. Lett.*, **29**, doi: 10.1029/2002GL015302.

Shearer, P. M., J. L. Hardebeck, L. Astiz and K. B. Richards-Dinger (2003). Analysis of similar event clusters in aftershocks of the 1994 Northridge, California, earthquake. *J. Geophys. Res.*, **108**, B1, 2035, doi 10.1029/2001JB000685.

Shearer, P. M., E. Hauksson and G. Lin (2005). Southern California hypocenter relocation with waveform cross-correlation, Part 2: results using source-specific station terms and cluster analysis. *Bull. Seismol. Soc. Am.*, **95**, 904–915.

Tatham, R. H. (1982). V_p/V_s and lithology. *Geophysics*, **47**, 336–344.

Van Huffel, S. (1997). Recent advances in total least squares techniques and errors-in-variables modeling. *Society for Industrial and Applied Mathematics*, Philadelphia, Pennsylvania.

Waldhauser, F., W. L. Ellsworth and A. Cole (1999). Slip-parallel seismic lineations on the northern Hayward Fault, California. *Geophys. Res. Lett.*, **26**, 3525–3528.

Zhang, H. and C. Thurber (2005). Adaptive mesh seismic tomography based on tetrahedral and Voronoi diagrams: application to Parkfield, California. *J. Geophys. Res.*, **110**, B04303, doi:10.1029/2004JB003186.

Zhang, H. and C. H. Thurber (2003). Double-difference tomography: the method and its application to the Hayward Fault, California. *Bull. Seismol. Soc. Am.*, **93**, 1875–1889.

The text of this chapter, in full, is a reformatted version of the material as it appears in Lin, G. and P. M. Shearer, Estimating Local V_p/V_s Ratios Within Similar Earthquake Clusters, *Bulletin of the Seismological Society of America*, in press, 2007. The dissertation author was the primary researcher and author. The co-author directed and supervised the research which forms the basis of this chapter. The original paper is copyrighted by the Seismological Society of America, and the material is included here by permission of SSA.

Chapter 6

A 3-D Crustal Seismic Velocity Model for Southern California from a Composite Event Method

Abstract. We present a new crustal seismic velocity model for southern California derived from P and S arrival times from local earthquakes and explosions. To reduce the volume of data and ensure a more uniform source distribution, we compute "composite event" picks for 2597 distributed master events that include pick information for other events within spheres of 2 km radius. The approach reduces random picking error and maximizes the number of S-wave picks. To constrain absolute event locations and shallow velocity structure, we also use times from controlled sources, including both refraction shots and quarries. We implement the SIMULPS tomography algorithm to obtain 3-D V_p and V_p/V_s structure and hypocenter locations of the composite events. Our new velocity model in general agrees with previous studies, resolving low velocity features at shallow depths in the basins and some high velocity features in the mid-crust. Using our velocity model and 3-D ray tracing, we relocate about 450,000 earthquakes from 1981 to 2005. We observe a weak correlation between seismic velocities and earthquake occurrence, with shallow earthquakes mostly occurring in high P velocity regions and mid-crustal earthquakes occurring in low P velocity regions. In addition, most seismicity occurs in regions with relatively low V_p/V_s ratios, although aftershock sequences following large earthquakes are often an exception to this pattern.

6.1 Introduction

Local Earthquake Tomography or LET (Thurber, 1993) has been widely used to obtain high resolution crustal images while simultaneously improving earthquake locations (Thurber, 1983). The resulting models are useful in resolving the geological structure of the crust, performing path and site effect studies, and computing strong ground motion simulations. In addition, the relocated hypocenters provide added information on crustal structure and tectonics. Most studies have used ray theoretical methods to model P and S arrival time data because of the proven effectiveness of this approach, although in principle additional information is contained in other parts of the seismic waveforms.

We apply LET to southern California P- and S-wave arrival time data from local earthquakes and explosions in order to derive a new crustal velocity model and improve absolute earthquake locations by correcting for the biasing effects of 3-D structure. To reduce the volume of data used in the tomographic inversions while preserving as much of the information in the original picks as possible, we apply a technique we term the "composite event" method. We simultaneously solve for the locations of the composite events and the velocity structure in our study area using Thurber's SIMULPS algorithm (Thurber, 1983, 1993; Eberhart-Phillips, 1990; Evans *et al.*, 1994). Our velocity model is similar to models from previous studies but also has some new features. The model can be used as a starting point for structural studies, earthquake locations, and ground motion calculations.

6.2 Data and Processing

Our initial data are the phase arrival times of *P* and *S* waves from 452,943 events, consisting of local events, regional events and quarry blasts, from 1981 to 2005 recorded at 783 stations in southern California and picked by the network operators. Figure 6.1 shows the station locations in our study area.

6.2.1 1-D Relocation

To obtain initial locations for these events, we apply the shrinking box source-specific station term (SSST) earthquake location method (Richards-Dinger and Shearer, 2000; Lin and Shearer, 2005) to the

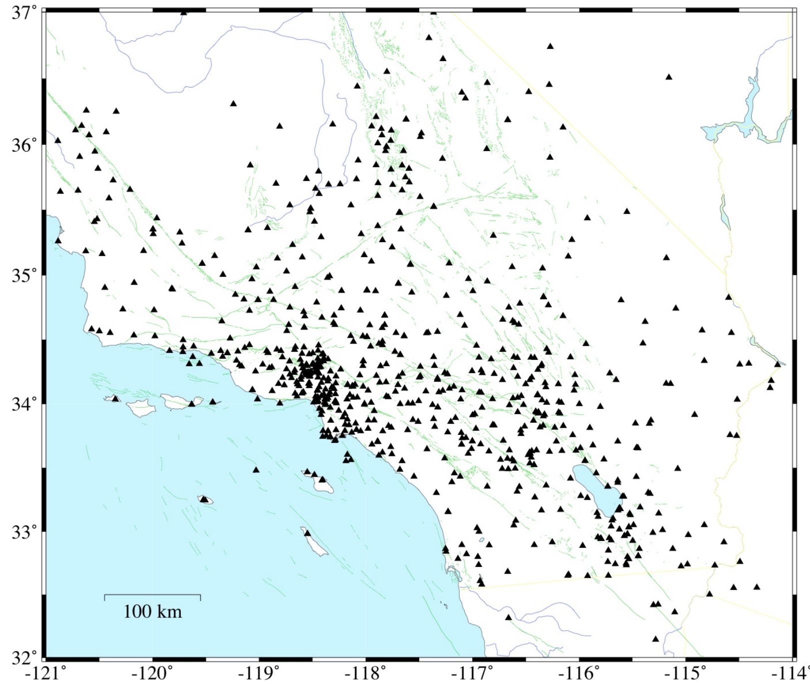

Figure 6.1. Locations of the 783 stations used in the study area.

452,943 catalog events using a 1-D velocity model that was used for the SHLK catalog presented by Shearer *et al.* (2005). To avoid P_g/P_n and S_g/S_n ambiguities, we use only arrivals with source-receiver ranges of 100 km or less. We minimize the robust least squares (Lin and Shearer, 2007) of the arrival time residuals to relocate the events with at least five picks. The distance cutoff for the station term calculation is reduced gradually during the iterations from 100 km to 8 km. This implements the shrinking box SSST method described in Lin and Shearer (2005). Figure 6.2 shows the relocated 428,871 events. Although the absolute location accuracy of this initial catalog is limited by the use of a 1-D model, the relative location accuracy is sufficient for us to use these locations to examine residual statistics and for the "composite event" calculations that we describe below.

6.2.2 Error Estimates

Before we start the tomographic inversions, we estimate the random picking errors and the scale-length of 3-D heterogeneity in our study area by analyzing differential residuals for pairs of events

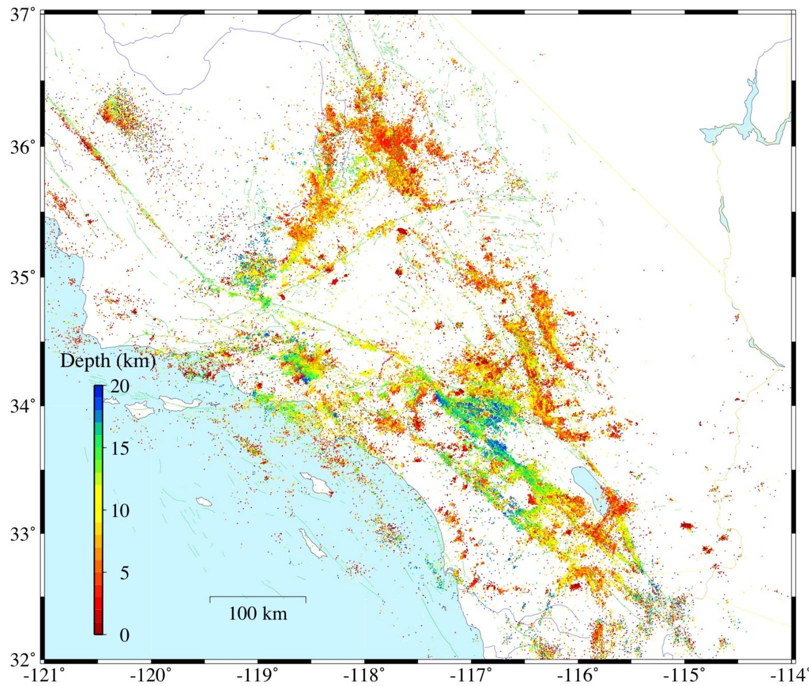

Figure 6.2. Locations of the 428,871 1-D relocated events using only the arrival time data in southern California from 1981 to 2005.

recorded at the same station. For a given pair of events, event i and event j, we compute the differential arrival time residual at a common station k after relocation as

$$dr_{ij} = r_i - r_j \tag{6.1a}$$

$$= (T_i^o - T_i^p - t_{0i}) - (T_j^o - T_j^p - t_{0j}) \tag{6.1b}$$

where T_i^o and T_j^o are the observed arrival times for event i and j, T_i^p and T_j^p are the predicted travel times from the 1-D velocity model, and t_{0i} and t_{0j} are the origin times of the events after relocation. Figure 6.3 shows the median absolute deviation (MAD) of the differential residuals as a function of event separation distance. By plotting how differential residual variance changes as a function of event separation distance, it is possible to characterize random picking error compared to the correlated signals caused by 3-D velocity structure (e.g., Gudmundsson *et al.*, 1990). In addition, these plots provide constraints on the scale-length of the heterogeneity and the appropriate distances to use in smoothing residuals for computing source-specific station terms. In principle, as the event separation distance shrinks to zero, the

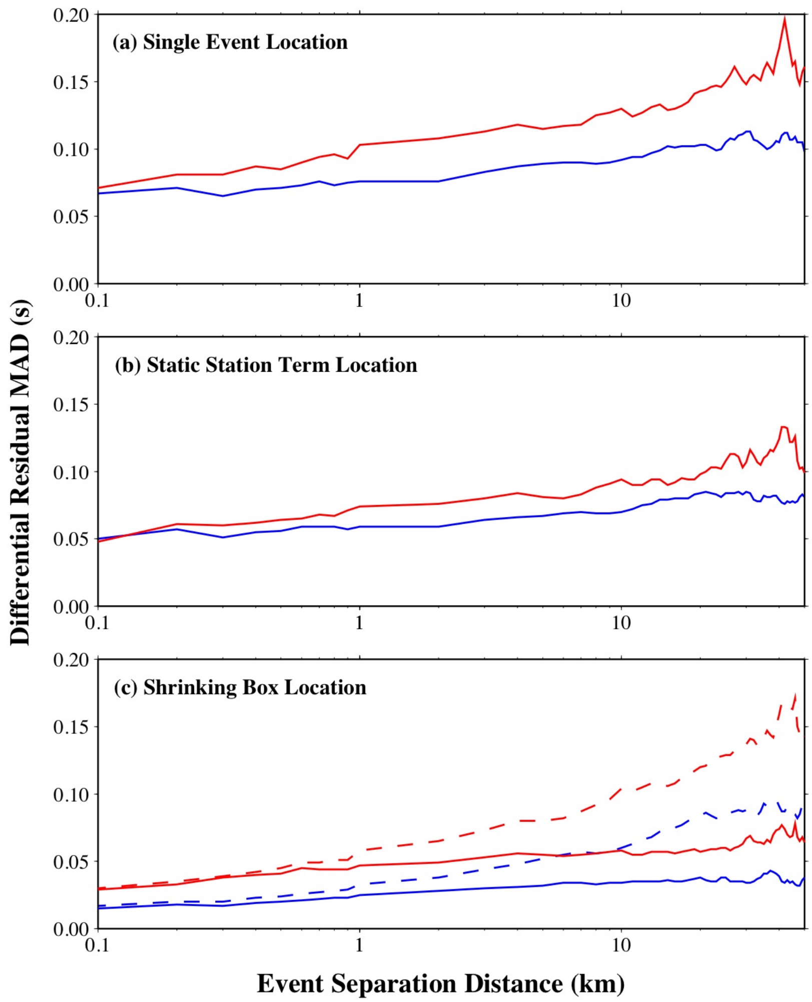

Figure 6.3. Differential residual MAD (Median Absolute Deviation) for *P* picks (blue) and *S* picks (red) as a function of event separation distance for: (a) single event location residuals, (b) static station term location residuals, and (c) shrinking box SSST location residuals. The dashed curves in (c) are the sums of the differential residuals and the source specific station terms, for P and S, respectively.

differential residual will reflect random picking error alone. However, this is true only if the locations and origin times are perfectly accurate. In Figure 6.3 the smallest differential residuals are achieved for the source-specific station term locations, consistent with random individual picking errors of 0.02 s for *P* (blue curve) and 0.03 s for *S* (red curve). The differential residuals show minimal growth with event separation in (c), indicating the effectiveness of the source-specific station terms in canceling the effects of 3-D structure. The dashed curves in (c) show the results when the SSSTs are added to the residuals; as expected the residuals grow significantly with event separation, and behave very similarly to the single event location residuals. Figure 6.3 also shows that the differential residual MAD increases with event separation distance, which implies that there exists some small-scale heterogeneity. This will be considered in the tomographic inversions presented below.

6.3 Composite Event Method

In principle, we would like to use all available events and pick information in tomographic inversions, but this is computationally intensive. To reduce the volume of data, as well as to make the event distribution more uniform, it is common to select a spatially diverse set of master events (e.g., Hauksson, 2000). However, this approach often discards the vast majority of the available picks. Here we present an approach, which we term the "composite event" method, that attempts to preserve as much of the original pick information as possible. The idea is similar to the summary ray method of Dziewonski (1984) and the grid optimization approach of Spakman and Bijwaard (2001). We exploit the fact that closely spaced events will have highly correlated residuals in which random picking error dominates, whereas residual decorrelation caused by 3-D structure will occur mainly at much larger event separation distances.

We use the 1-D shrinking box SSST locations for this method, since they provide good relative earthquake locations. Figure 6.4 shows how our composite event algorithm works. The triangles are the stations and the small squares are the target events. Composite events are derived from the residuals for all events within a radius of r_1 of the target event. The number of composite events is limited by requiring them to be separated from each other by a radius, r_2. We select the first target event as the one from our

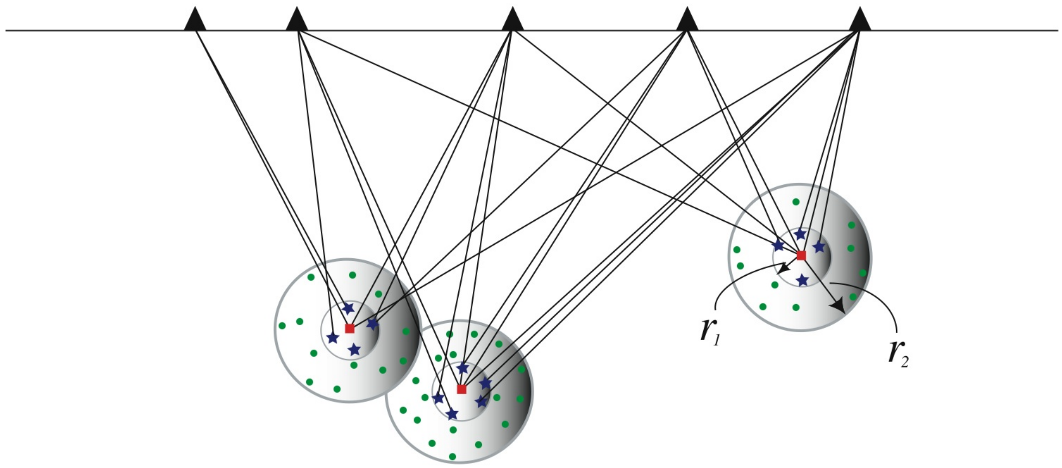

Figure 6.4. A cartoon showing how our composite event algorithm works. The triangles are the stations. The squares represent the target events and stars are the nearby events around the targeted composite event in a given radius r_1, which provide additional travel time information for the composite events. The dots are the events excluded from consideration as future composite events after we choose each composite event. See text for more details.

entire data set that has the greatest number of contributing picks from all the nearby events, shown by the stars in Figure 6.4 in the sphere with radius r_1 centered at the target event. The location of the composite event is the centroid of all the events in the sphere r_1. Arrival time picks for the composite event to each station that recorded any events within the sphere r_1 are the robust mean (Lin and Shearer, 2007) of the arrival time residuals from the individual events added to the calculated travel time from the composite event location to the station, using the same 1-D velocity model used to locate the events and compute the residuals.

This process results in composite event picks that preserve the pick information of the contributing events, and which are relatively insensitive to the assumed 1-D velocity model. Next, the events within the sphere with radius r_2 centered at this event, shown by the dots, are flagged so that they will not be treated as candidates for additional composite events. The second target event is the one among all the remaining events that has the greatest number of contributing picks from all the nearby events in the sphere with radius r_1, then again the events within the sphere with radius r_2 centered at this event are flagged, and so on.

The total number of composite events depends on the size of r_2, and the number of contributing picks on the size of r_1. In our study, considering the computational requirements of our planned tomographic inversions, the scale length of 3-D heterogeneity in our study area, and the desired composite event distribution, we use 2 km for r_1, 6 km for r_2 and constrain each composite event to have more than 20 picks with at least 5 S-picks. This results in 2,597 composite events consisting of 110,913 composite P picks and 54,303 composite S picks, while the number of total contributing P picks is 2,293,728 and S picks is 575,769. In other words, 0.6% of the total events—the 2,597 composite events—preserve most of the information of 38% of the original picks (7.75 million picks). The composite events are shown in Figure 6.5a by the dots.

We have found that the resulting composite event picks are not very sensitive to changes in the 1-D velocity model used to compute the individual event locations and that their residuals are highly correlated to the residual patterns from single events. In Figure 6.6, we show residual comparisons between single events and composite events at common stations for 2 randomly chosen events. The patterns of both P and S residual distributions are very similar between the single and composite events. This confirms that the arrival time picks of our composite events carry the same information as the contributing events, which we will solve for in our tomographic inversions. The advantage of using composite events rather than single master events is that the random picking error is reduced by averaging picks from many nearby events and that the maximum possible number of stations can be included for each event (i.e., generally no single event has picks for all of the available stations). This is particularly valuable for maximizing the number of S picks, which are picked relatively infrequently by the network operators and total only about 26% of the number of P picks in the complete data set.

6.4 Controlled Sources

Because of the trade-off between earthquake locations and velocity structure in the tomography problem, controlled sources are often used in velocity inversions to provide absolute reference locations

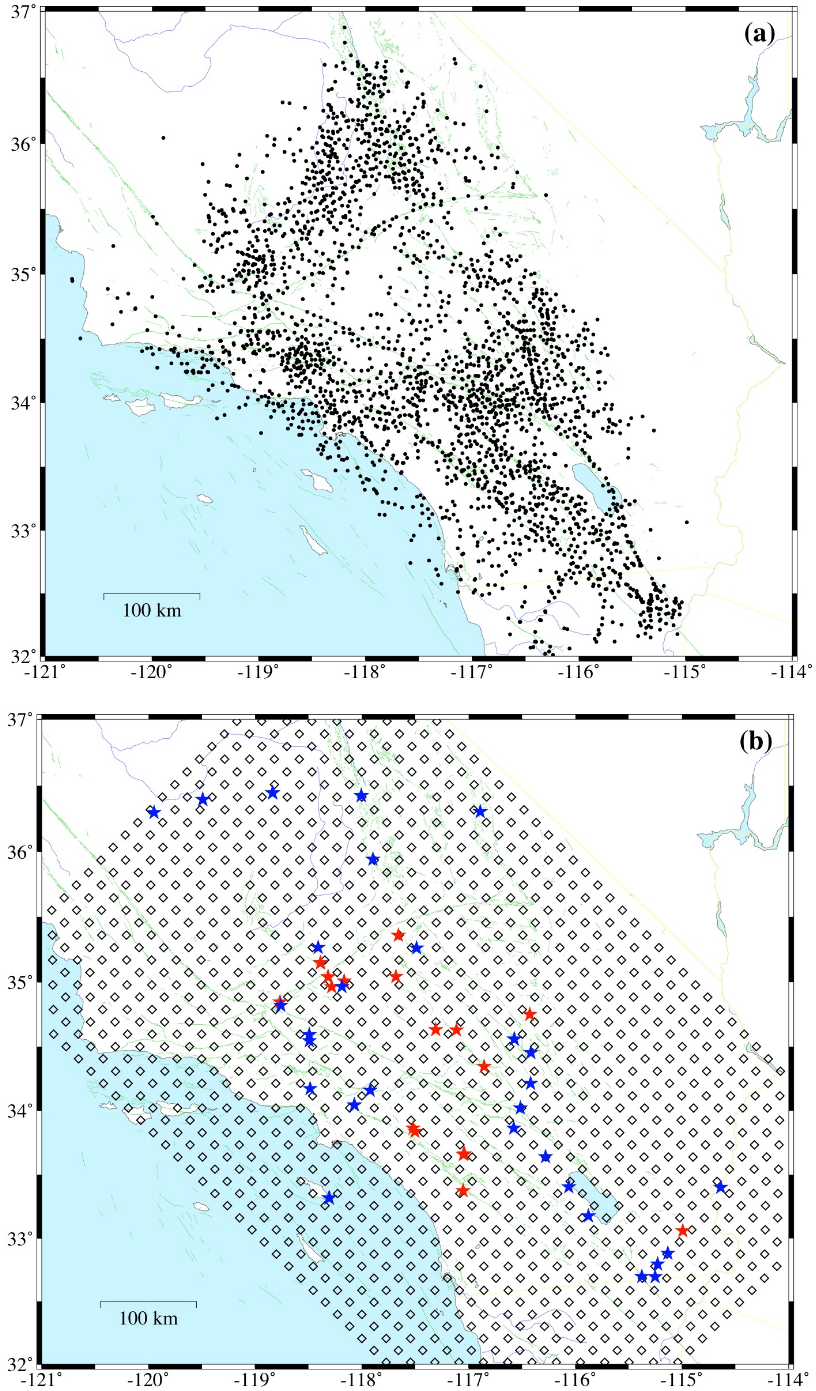

Figure 6.5. (a) The 2,597 composite events are shown by the dots. (b) The diamonds are the 15-km grid points for our tomographic inversion. The red stars are the 19 quarries and the blue stars are the 36 shots, which are used in the tomographic inversion to constrain absolute event locations and shallow velocity structure.

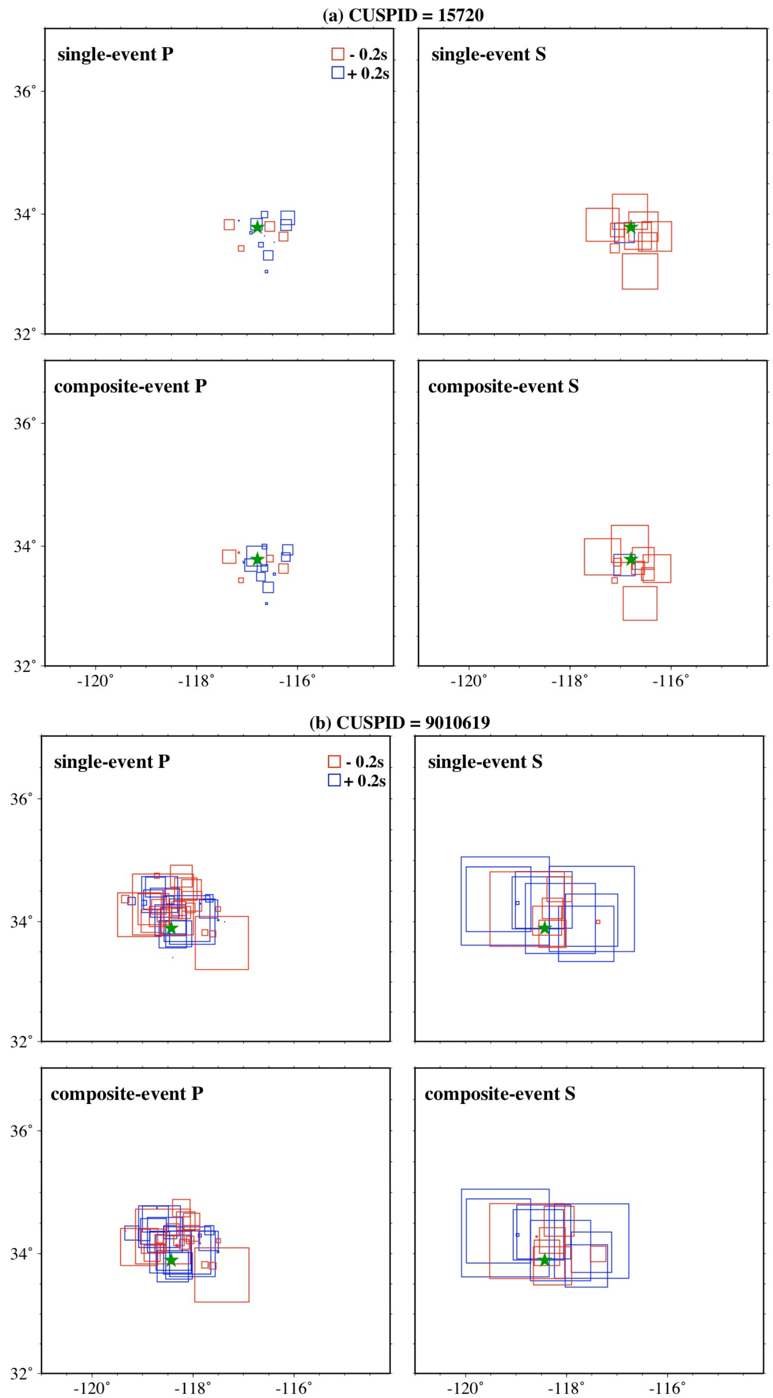

Figure 6.6. Arrival time residual comparison between single events and composite events. We show residuals from both the catalog event and the composite event for 2 randomly chosen events at common stations. The similar residual patterns confirm that the arrival time data of our composite events carry the same information as the contributing events, which we will solve for in our tomographic inversions.

for 3-D velocity models and to constrain the shallow crustal structure. Two types of controlled sources are typically used: quarry blasts and shots. Quarry blasts are man-made explosions of known location but unknown origin time, while shots also have known origin times. Our study also includes arrival times from 36 shots recorded by the SCSN and 19 quarries (see Figure 6 in Lin *et al.*, 2006). The phase data for the 19 quarries are obtained using the composite event method from the pick information for 16,574 individual events flagged as quarry blasts by the SCSN. The controlled sources in our study are plotted as the inverted triangles and stars in Figure 6.5b.

6.5 3-D Simultaneous Earthquake Locations and Tomography

6.5.1 Inversion Method

We apply the inversion method and computer algorithm SIMULPS developed by Thurber (1983, 1993) and Eberhart-Phillips (1990) (documentation provided by Evans *et al.*, 1994). SIMULPS is a damped-least-squares, full matrix inversion method intended for use with natural local earthquakes, with (or without) controlled sources, in which P arrival times and S-P times are inverted for earthquake locations, V_p, and V_p/V_s variations. The algorithm uses a combination of parameter separation (Pavlis and Booker, 1980; Spencer and Gubbins, 1980) and damped least squares inversion to solve for the model perturbations. The appropriate damping parameters are found using a data variance versus model variance tradeoff analysis. The resolution matrix is computed in order to estimate the resolution of the model and the uncertainties in the model parameters.

6.5.2 Velocity Model Parametization

We find that the resulting 3-D models depend significantly on the 1-D starting model. Our strategy to reduce this dependence is to first use SIMULPS to derive a best-fitting 1-D model using our 1-D location velocity model as a starting model (shown by the blue line in Figure 6.7), and then use the resulting 1-D model (shown by the red line in Figure 6.7) as the starting model for the 3-D tomographic inversions. The depths of the grid points are 0, 3, 6, 10, 15, 17, 22, and 31 km. The 17-km point is selected to permit a relatively sharp velocity increase to occur near 16 km, which has been observed in some studies (e.g., Hadley and Kanamori, 1977) and which may correspond to the transition to a lower crust of predominantly mafic composition. The starting V_p/V_s ratio is 1.78, which is the average crustal V_p/V_s ratio in southern California (Zhu and Kanamori, 2000). In order to test the sensitivity of the velocity model to the initial V_p/V_s ratio, we also used 1.73 as the starting value of the V_p/V_s ratio and found that the model is very similar to the one using 1.78 and fits the data almost the same. We start with the horizontally uniform layered model (shown by the red line in Figure 6.7) to invert for a 3-D model using a 15-km horizontal grid. While in principle the 6-km spacing among our composite events would permit resolving features smaller than 15 km, we were limited by our available computer power to a 15-km grid spacing.

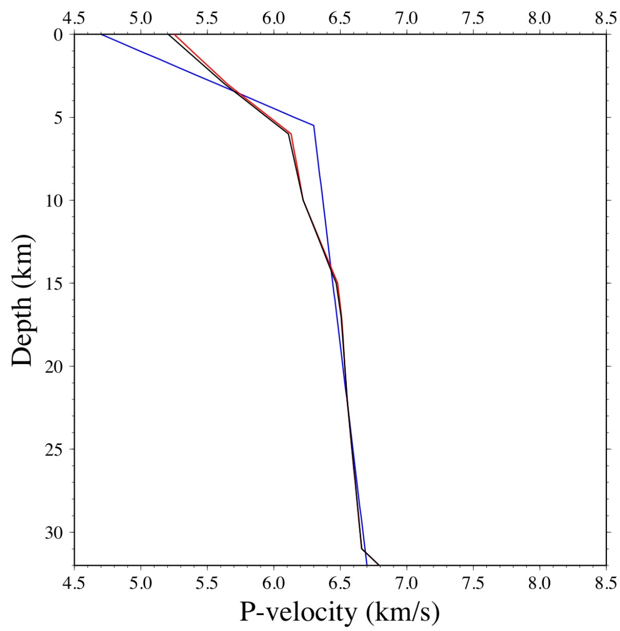

Figure 6.7. The P-velocity models as a function of depth: the 1-D starting model (blue line), the 3-D starting model (red line) and the final model (black line).

6.5.3 Misfit versus Model Variance Tradeoff Curve

In order to choose an optimal damping parameter for V_p and the V_p/V_s ratio, we ran a series of single-iteration inversions with a large range of damping values, and plotted data misfit versus model variance

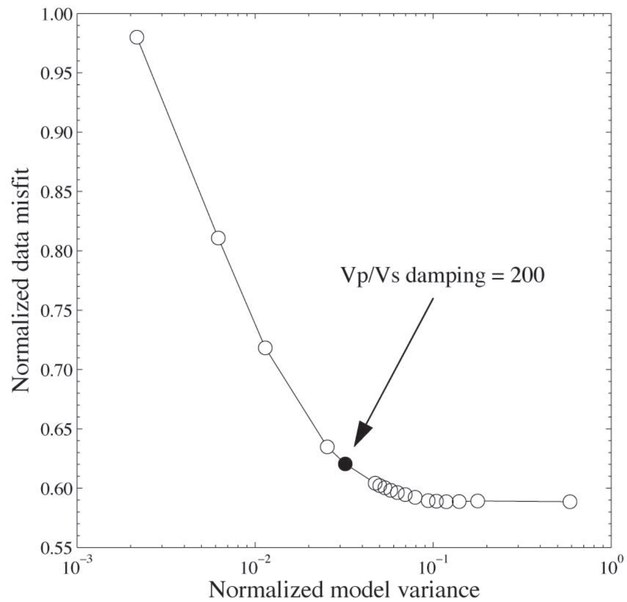

Figure 6.8. Tradeoff curve between data misfit and model variance for V_p/V_s while the SIMULPS damping parameter for V_p is held at 800.

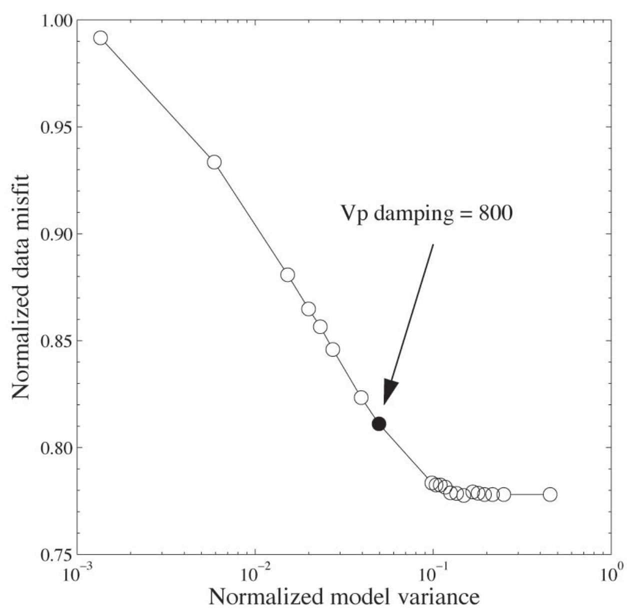

Figure 6.9. Tradeoff curve between data misfit and model variance for V_p while the SIMULPS damping parameter for V_p/V_s is held at 200.

for these runs (e.g., Eberhart-Phillips, 1986, 1993). We chose damping for V_p with a tradeoff curve while holding V_p/V_s damping fixed at a large value so that the effect of the S data would be as small as possible. We found that the data misfit is not as sensitive as the model variance to the damping parameter. We chose 800 as the SIMULPS damping value for V_p, which produced a good compromise between data misfit and model variance. Similarly, we chose damping for V_p/V_s while holding V_p damping fixed at 800. Figure 6.8 is the tradeoff curve for the V_p/V_s ratio. The value we use in our tomographic inversions is 200. In order to verify that 800 is an appropriate damping value for V_p, we ran another series of single iterations with a range of V_p damping values while keeping V_p/V_s damping as 200. Figure 6.9 shows this tradeoff curve, in which 800 is above the minimum misfit level, which means we have selected a relatively smooth model. But since the data variance is not very sensitive to the damping values, we prefer this conservative choice of damping for V_p.

6.6 3-D Velocity Model Results

We performed our inversions in two different stages, both with and without station terms. To avoid projecting resolvable shallow velocity structure into the station corrections, we solved for an initial model without using station terms in 4 iterations of the SIMULPS algorithm. We used this model as a starting point for 4 subsequent iterations in which we computed station terms with respect to the current 3-D model to limit the influence of rapid near-surface velocity variations (i.e., too sharp to be modeled with our 15-km grid and our damping parameters) on deeper parts of the model. Table 6.1 presents the parameters used in our tomographic inversions. Figure 6.10 shows the histograms of arrival time residuals for the composite events. The MAD residual value is reduced from 0.173 s for the 1-D starting model to 0.076 s after simultaneous tomography and relocation.

Table 6.1. Parameters for our 3-D velocity models.

Grid	V_p	V_p/V_s	Data Variance, s^2		Model Variance, km/s^2	
km	Damping	Damping	Initial	Final	V_p	V_p/V_s
15	800.0	200.0	0.13732	0.04620	0.02904	0.00137

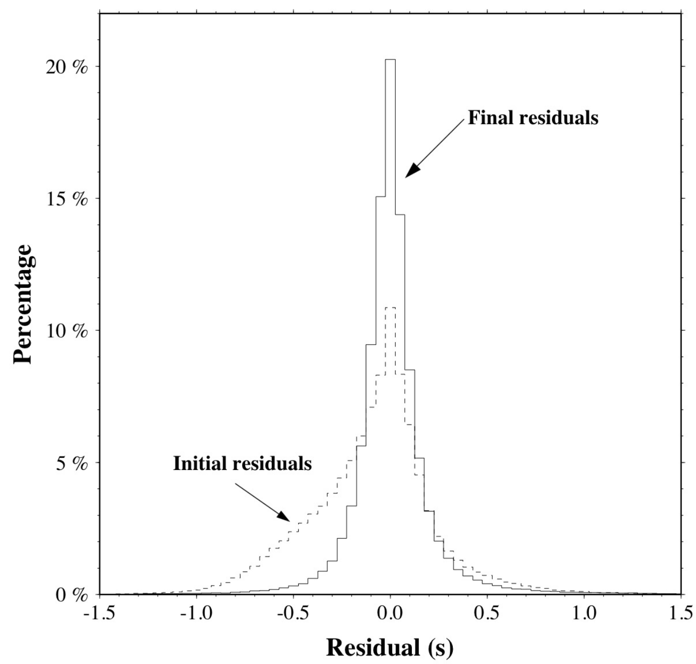

Figure 6.10. Histogram of arrival time residuals for the composite events, showing results before and after simultaneous location and tomography.

6.6.1 P Velocity Model

Figure 6.11 shows the V_p perturbations relative to the layer-averaged velocities in the first 6 layers. The SIMULPS algorithm provides the resolution matrix, which gives an indication of how well-resolved the velocity is at each gridpoint. The values of the resolution throughout the gridspace could be increased by decreasing the damping parameter, but the velocity results may be less reliable. The black contours in the mapviews enclose the resolved areas with the resolution diagonal element more than 0.1, while 1.0 represents the best resolution. The top two layers of our V_p model at 0 and 3 km depth have V_p changes of relatively small spatial length, reflecting the near-surface geology such as bedrock outcrops and late Quaternary sedimentary deposits. In particular, the velocities in these two layers are correlated with the surface geological features. The basin areas, such as the southern San Joaquin Valley, the Ventura Basin, the Los Angeles Basin and the Imperial Valley show low velocity anomalies, while the major mountain ranges, such as the Coast Ranges, the Transverse Ranges, the San Gabriel Mountains, and the Peninsular Ranges show higher velocities. In the 6 km-depth layer, the velocity anomalies seen at the surface are still visible but become less prominent. In the middle crust (10 km), some of the features seen at shallower depths are reversed. For example, the Imperial Valley shows high velocity anomalies and the Transverse Ranges are underlain by low velocity anomalies. In the lower crust (15 km and 17 km), although the resolved areas are small, the Ventura Basin, the Los Angeles Basin, the Imperial Valley, and the southern San Joaquin are dominated by high velocity anomalies, whereas the Transverse Ranges, the San Gabriel Mountains and the San Bernardino Mountains all show low velocities. The Peninsular Ranges, however, always show high velocity in each layer. Our V_p model is very similar to the one by Hauksson (2000) except that the low velocity anomalies in the basin areas extend to depths of about 10 km in our model (in particular, the Ventura Basin, the Los Angeles Basin, and the Imperial Valley), whereas the corresponding anomalies are present to only about 5 or 6 km in the Hauksson (2000) model.

We present two kinds of cross-section profiles of our model. These profiles are shown in Figure 6.12. One set is across the San Andreas fault from SW to NE shown by the straight lines marked with letters (e.g., A, B, ... , H) and the other set is parallel to the San Andreas fault from NW to SE shown by the numbers (e.g., 1, 2, ... , 6). Figure 6.12 also shows some geological features in our study area and the V_p perturbations in the first layer in our model (same as Figure 6.11(a)).

The cross-sections of our P-velocity model for the profiles A, B, C, D, E, F, G and H are shown in Figure 6.13. The values of distances decrease from the SW starting point to the NE ending point. The black contours enclose our resolved area with the SIMULPS resolution diagonal element above 0.1. We also plot the background seismicity within $\pm$10 km of the profiles shown by the black dots. It is apparent that the resolution is the best where earthquakes are well-distributed, and the resolution below 15 km depth is generally low except where there are deeper earthquakes. Again the correlations between the velocities in the shallower layers of our model with the surface geological features are seen in these cross-sections. Low velocity anomalies are pronounced in the basin regions, such as the Ventura Basin in profile C, the Los Angeles Basin in D and the Imperial Valley in H, whereas relatively higher velocities

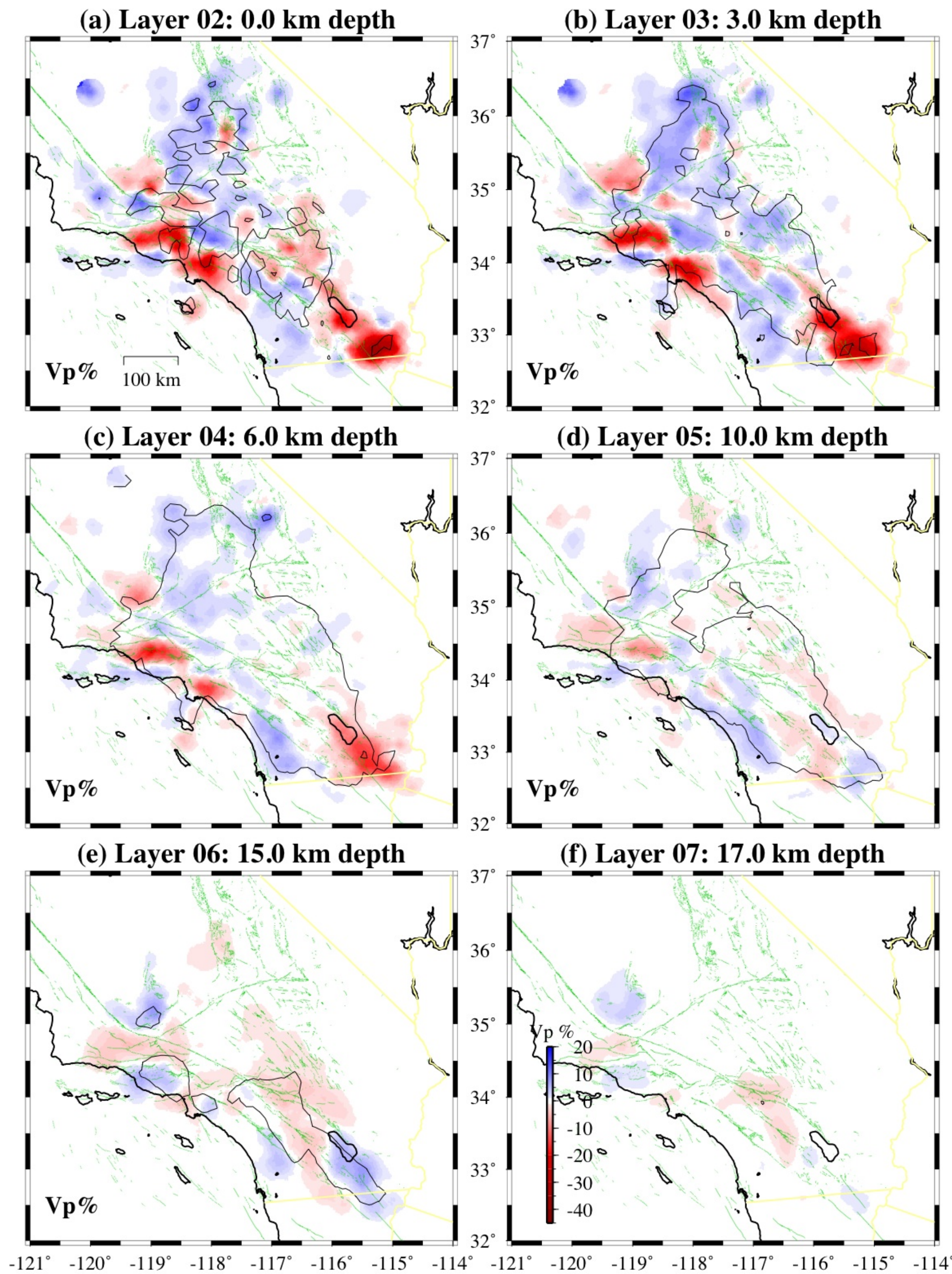

Figure 6.11. P velocity perturbations relative to the average velocity in each layer after smoothing. The black contours circle the area that we are able to resolve with the the SIMULPS resolution diagonal element above 0.1.

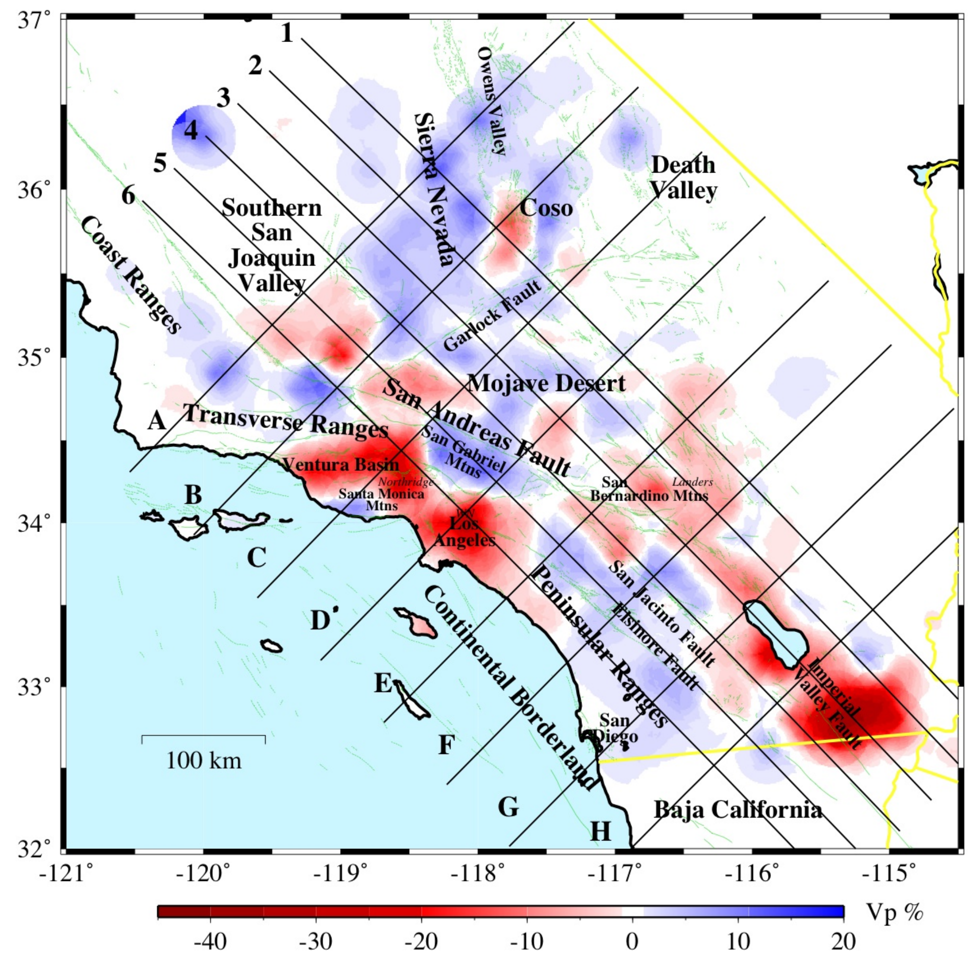

Figure 6.12. Some geological features in our study area and the depth profiles shown by the black straight lines for the following cross-section views. The SW-NE direction profiles (shown by the letters, A, B, C, D, E, F, G, and H) are across the San Andreas fault; and the NW-SE direction profiles (shown by the numbers, 1, 2, 3, 4, 5, and 6) are parallel to the San Andreas fault. The V_p perturbations in the first layer (0 km depth) are also shown in this figure.

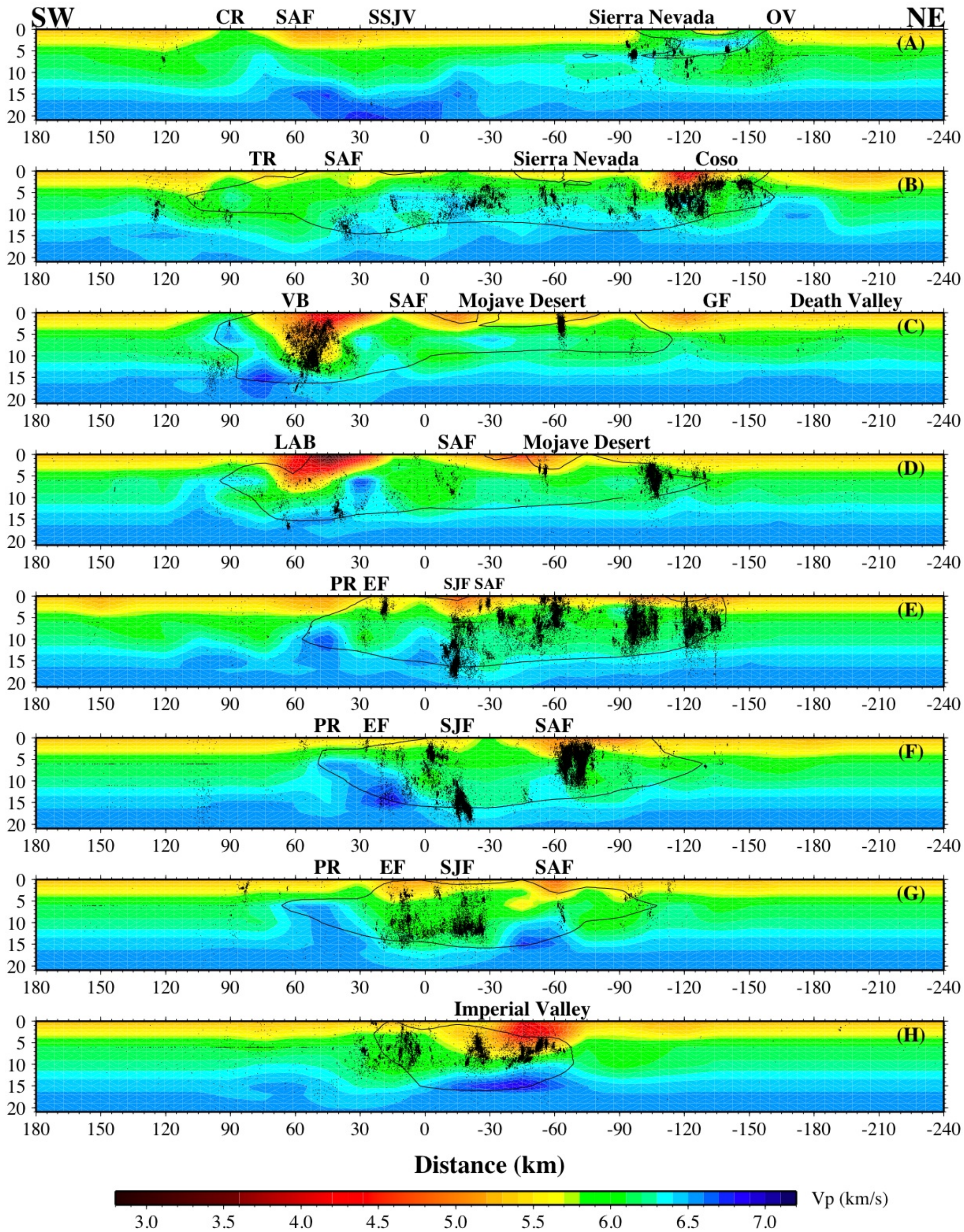

Figure 6.13. Cross-sections through our V_p model along the SW-NE profiles shown in Figure 6.12 by the letters, including the background seismicity (black dots) within ± 10 km distance of the profile line. The black contours enclose the regions with the SIMULPS resolution diagonal element above 0.1. The vertical exaggeration is 2. Abbreviations: CR, Coast Ranges; SAF, San Andreas Fault; SSJV, Southern San Joaquin Valley; OV, Owens Valley; TR, Transverse Ranges; VB, Ventura Basin; GF, Garlock Fault; LAB, Los Angeles Basin; PR, Peninsular Ranges; EF, Elsinore Fault; SJF, San Jacinto Fault.

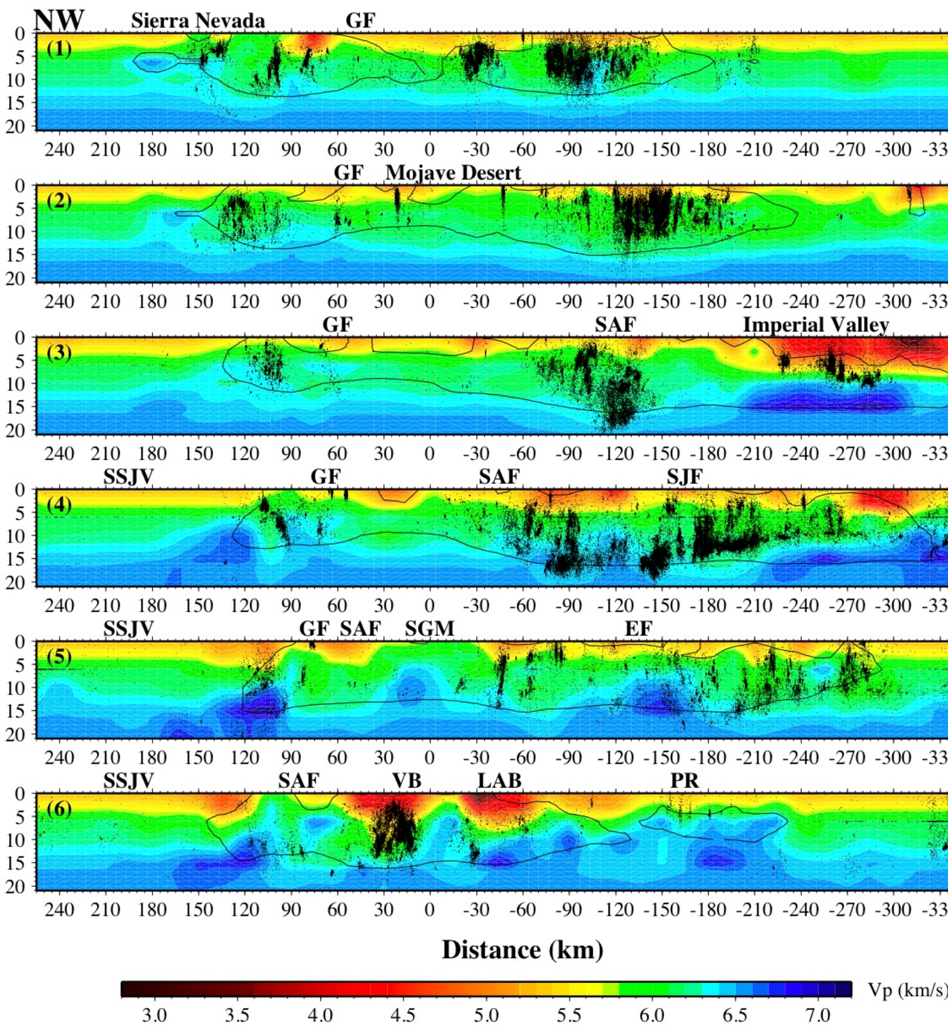

Figure 6.14. Cross-sections through our V_p model along the NW-SE profiles shown in Figure 6.12 by the numbers, including the background seismicity (black dots) within 10 km distance of the profile line. The black contours enclose the regions with the SIMULPS resolution diagonal element above 0.1. The vertical exaggeration is 3. SGM is short for San Gabriel Mountains. Other geographical and fault names are the same as in Figure 6.13.

are seen at the mountain ranges, such as the Coast Ranges in A and the Pennisular Ranges in E, F, and G. The very low velocities at depths to about 3 or 4 km are indicative of sediments. As shown in the mapviews, velocities are relatively low in many of the basin areas to about 10 km depth. We tend to image relatively fast regions in the deeper crust immediately below the lower velocity anomalies in the shallower layers. Similar features are seen in the Hauksson (2000) model, except that the low velocity anomalies only extend to about 5 or 6 km depth in that model. The Coso volcanic area in B is underlain by low velocities to about 5 km depth and the Southern Sierra Nevada is imaged by relatively high velocities. The Peninsular Ranges are always underlain by high velocities and the velocity increase with depth in the nearby regions is much faster relative to other areas.

Figure 6.14 shows the cross-sections of our V_p model for the profiles 1, 2, 3, 4, 5 and 6 in Figure 6.12, which are parallel to the San Andreas fault direction from NW to SE. The numbers of the profiles increase from the east side of the San Andreas fault to its west side and analogous features to those in Figure 6.13 are seen. These patterns are also very similar to those in the Hauksson (2000) model, except that the lowest velocity in the Imperial Valley occurs along profile 3 in our model, whereas it would be along profile 4 in Hauksson's model. This may be due to the different gridding scheme used in the two models.

6.6.2 V_p/V_s Model

We plot absolute V_p/V_s ratios at each layer depth in Figure 6.15. Because of the even distribution of our composite events and the constraints on the number of picks, the areal extent of our V_p/V_s model is nearly as good as the V_p model. Again the well-resolved parts are enclosed by the 0.1 SIMULPS resolution contours. Even though our SIMULPS damping parameter is 200, the V_p/V_s model has comparable resolution to the V_p model, indicating that our composite event method has succeeded in obtaining sufficient S picks over a large region.

The starting V_p/V_s model is 1.78, which is slightly higher than the common value, 1.73, for earthquake location studies in southern California. As we discussed in the previous section, this choice did not

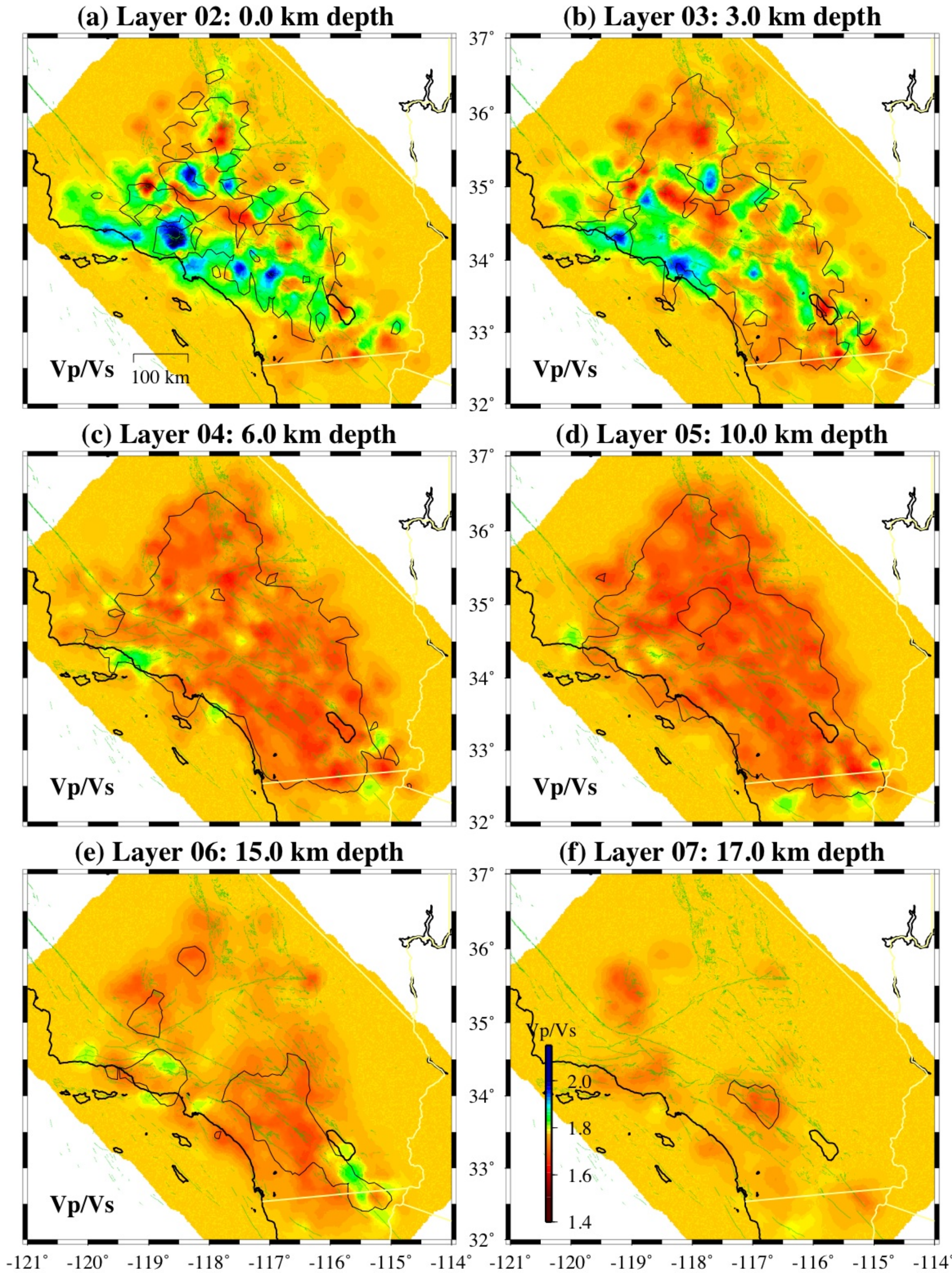

Figure 6.15. Absolute V_p/V_s values in each layer after smoothing. The black contours circle the area that we are able to resolve with the SIMULPS resolution diagonal element above 0.1.

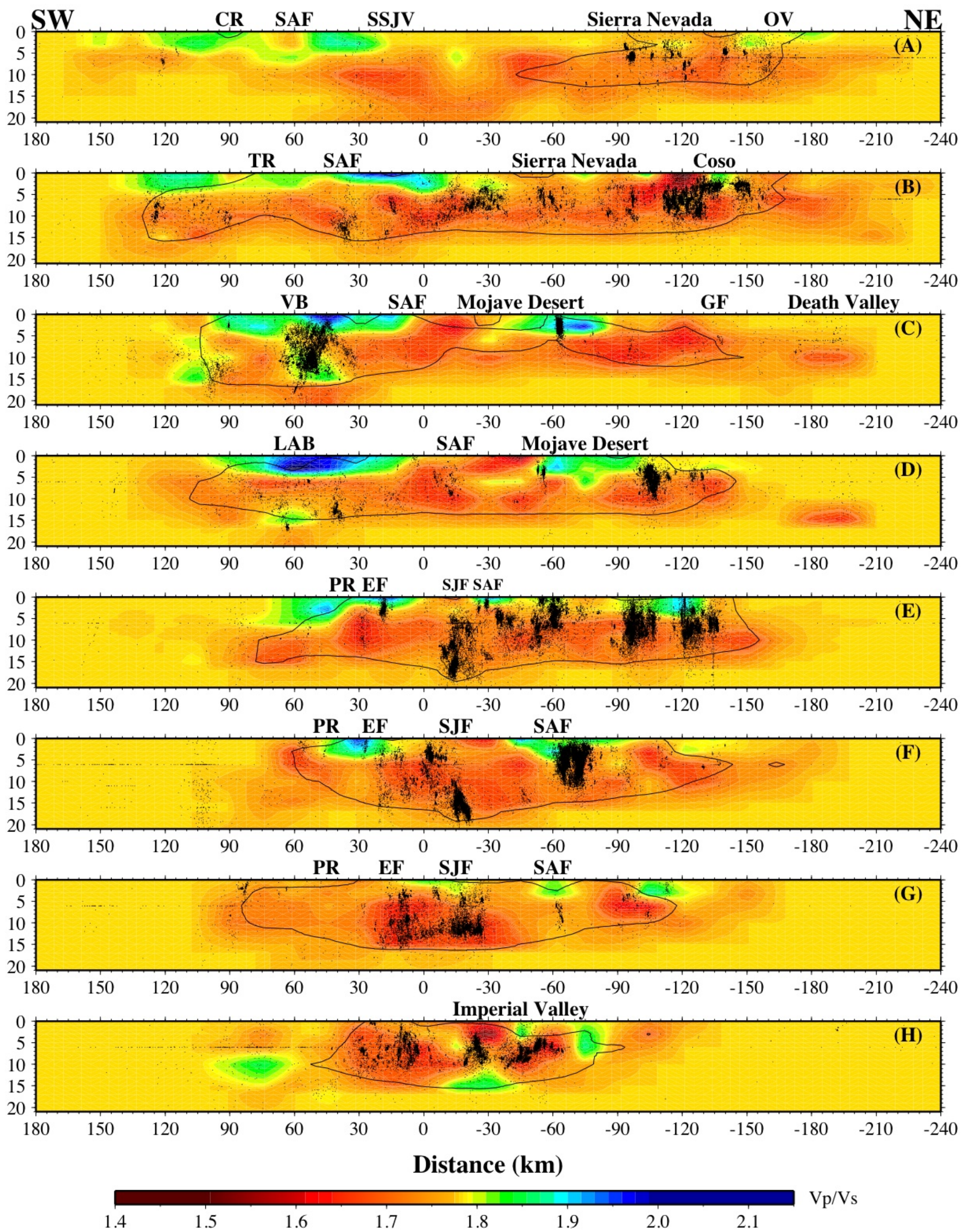

Figure 6.16. Cross-sections through our V_p/V_s model along the SW-NE profiles shown in Figure 6.12 by the letters, including the background seismicity (black dots) within 10 km distance of the profile line. The black contours enclose the regions with the SIMULPS resolution diagonal element above 0.1. The vertical exaggeration is 2. The geographical and fault names are the same as in Figure 6.13.

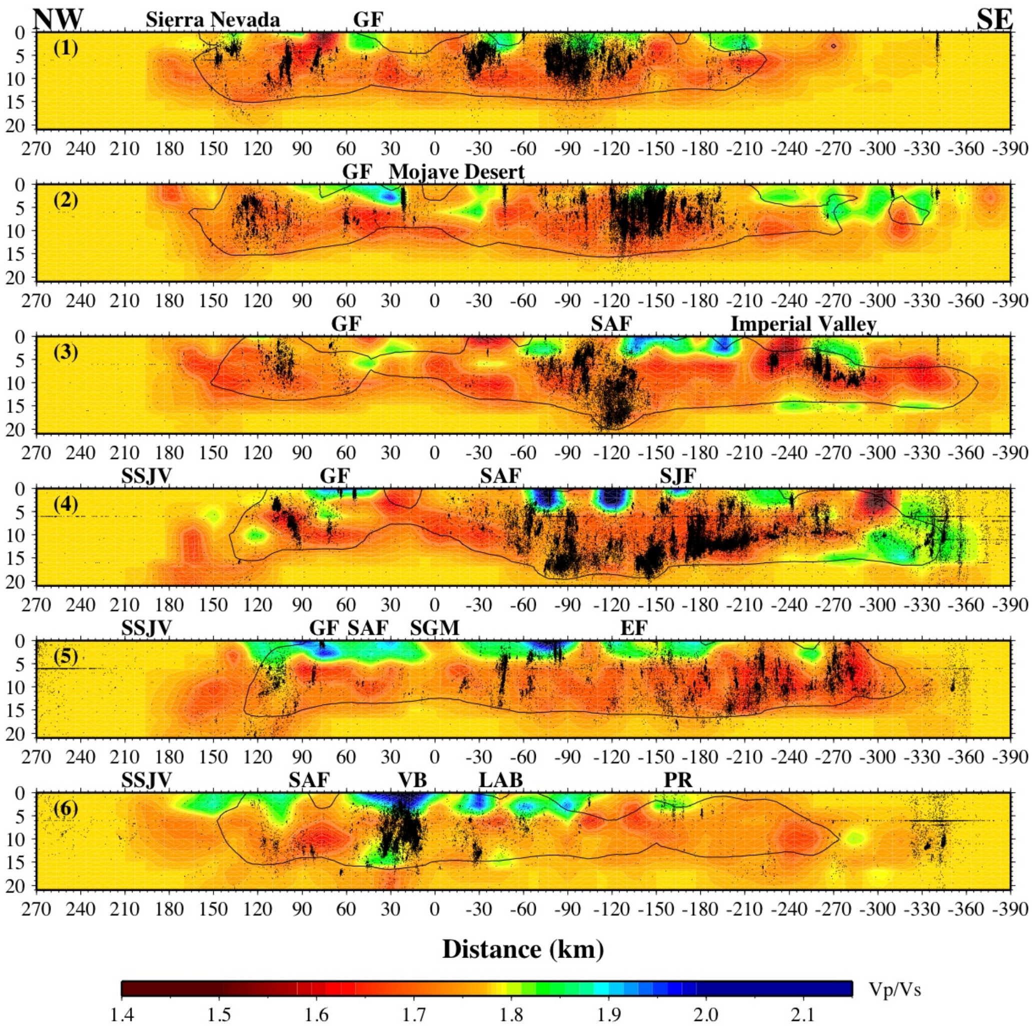

Figure 6.17. Cross-sections through our V_p/V_s model along the NW-SE profiles shown in Figure 6.12 by the numbers, including the background seismicity (black dots) within 10 km distance of the profile line. The black contours enclose the regions with the SIMULPS resolution diagonal element above 0.1. The vertical exaggeration is 3. The geographical and fault names are the same as in Figure 6.14.

affect our results. From the mapview in Figure 6.15, we observe both the short spatial length variations at shallower depth and a slight decrease in average V_p/V_s compared to the starting model. The overall V_p/V_s ratio in our model ranges from 1.2 to 2.3. Two grid points contain V_p/V_s ratios of about 1.2 (at 0 km depth in the Southern San Joaquin Valley region) and 1.3 (at 3 km depth in the Imperial Valley area), which are physically unrealistic and are probably due to artifacts in our data or velocity inversions. All the other grid points have V_p/V_s values above 1.4.

Our V_p/V_s model looks quite different than the Hauksson (2000) model, probably due to our higher starting V_p/V_s value, larger damping parameters and different data sets. In the first two shallow layers (0 and 3 km), we see relatively small-scale V_p/V_s anomalies. The basin areas, such as the Southern San Joaquin Valley, the Ventura Basin, the Los Angeles Basin, and the Imperial Valley, are imaged by higher anomalies in V_p/V_s values. With the corresponding lower P velocities in these regions, these features are consistent with water-satured sediments. In contrast, the San Gabriel Mountains and the Peninsular Ranges show low V_p/V_s values and high V_p anomalies. We do not see the higher V_p/V_s values around the Peninsular Ranges and in Baja California seen in the Hauksson (2000) model. For the 6 and 10 km depth layers, most parts of the well-resolved regions are underlain by lower V_p/V_s values of about 1.71, except that some higher V_p/V_s values are seen in areas along the coast. The resolved areas in the deeper model points (15 and 17 km) are small and have similar patterns as in the V_p model. In the Hauksson (2000) model, many high V_p/V_s anomalies are seen below 6 km rather than at the shallower depths where they often occur in our model. These differences are also seen in the cross-sections.

In Figure 6.16 and Figure 6.17, we plot the cross-sections of the V_p/V_s model, and see similar features as in the mapview. Although the starting model is 1.78, the resolved areas show average V_p/V_s around 1.73. The basin areas show very high V_p/V_s anomalies near the surface, such as the Ventura Basin, the Los Angeles Basin and the Imperial Valley. We also observe high V_p/V_s blobs beneath some basins in the lower crust, such as the Ventura Basin in profile C and 6, the Los Angeles Basin in D and the Imperial Valley in H and 3. These may be due to the presence of mafic rocks or fluids.

6.7 Seismicity and Velocity Structure

Figure 6.18 plots P velocity versus depth at the quake locations, compared to the median velocity within the resolved regions of the 3-D model. Focusing first on the velocity model alone, note that the size of the velocity perturbations generally decreases with depth. At shallow depths (< 8 km), the low anomalies (associated with the sedimentary basins) are larger in magnitude than the high anomalies. However, in the lower crust (> 14 km) the high velocity anomalies are larger in magnitude than the low velocity anomalies. The median velocity at the earthquake locations generally tracks the median velocity profile in the 3-D model. However, there are two depth ranges at which the median velocities are significantly different. Between about 1 and 5 km depth, the earthquakes tend to occur more often in rock with higher than average velocity, whereas between about 11 and 18 km, the earthquakes are more likely to occur in slower than average crust. This pattern can also be seen in Figure 6.19 and Figure 6.20, which map the velocity perturbations and the quake locations near 3 km and 15 km depth. Although there are some exceptions (e.g., the shallow Northridge aftershocks), quakes between 2 and 4 km depth tend to occur in the relatively fast hard rock between the sedimentary basins. In contrast, earthquakes between 14 and 16 km are relatively sparse in the highest P velocity parts of the model.

We also observe a correlation between earthquake occurence and lower V_p/V_s values in the mid-crust, as shown in Figure 6.21, which plots the V_p/V_s ratio versus depth at the quake locations, compared to the median value within the resolved regions of the 3-D model. The median V_p/V_s values in the model stay at the starting value of 1.78 in the poorly resolved uppermost 3 km and below 17 km, but approach 1.73 in the best resolved depth range between about 6 and 12 km. At these depths, the earthquakes tend to occur in regions with lower V_p/V_s, with median values of 1.70 to 1.71. There are very few earthquakes in parts of the model with V_p/V_s above about 1.83, an observation similar to results for the 1989 Loma Prieta rupture region (Thurber *et al.*, 1995). We experimented with using different starting V_p/V_s values for the tomographic inversion and found that the results within the well-resolved depths were relatively insensitive to the starting model, and that the correlation of low V_p/V_s regions with seismicity is a robust result. This correlation can be seen visually in Figure 6.22, which maps seismicity between 9 and 11 km

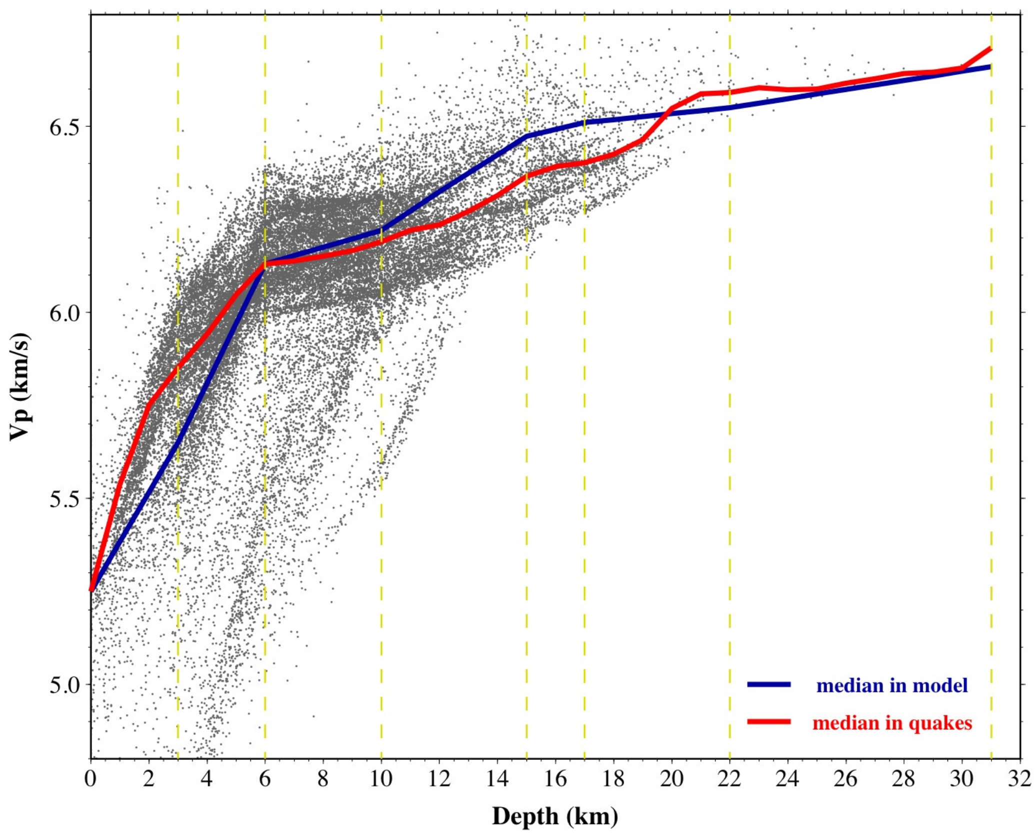

Figure 6.18. P velocity versus depth. The dots are a random 10% of the entire earthquake set. The red curve shows the median P velocity at the earthquake locations at 1 km depth intervals. For comparison, the blue curve shows the median of the tomography model over all well-resolved grid points.

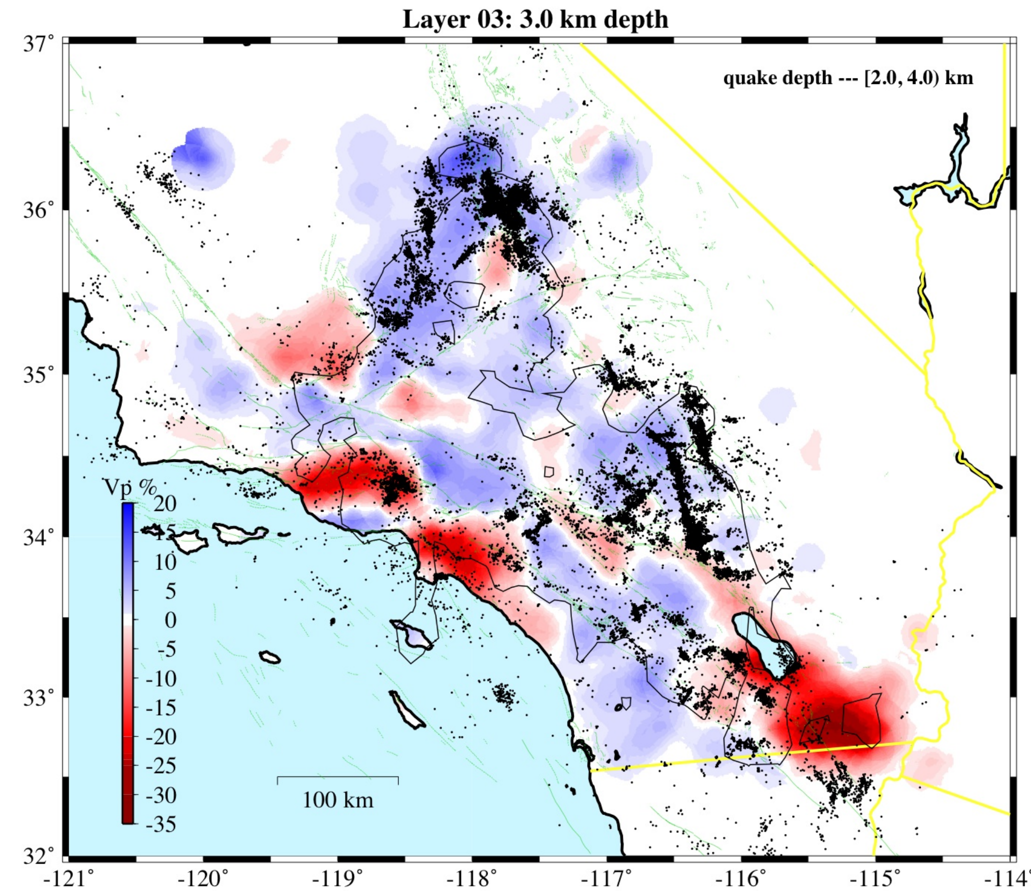

Figure 6.19. Seismicity between 2 and 4 km depth, compared to P velocity perturbations at 3 km. Fast regions are shown in blue and slow regions in red.

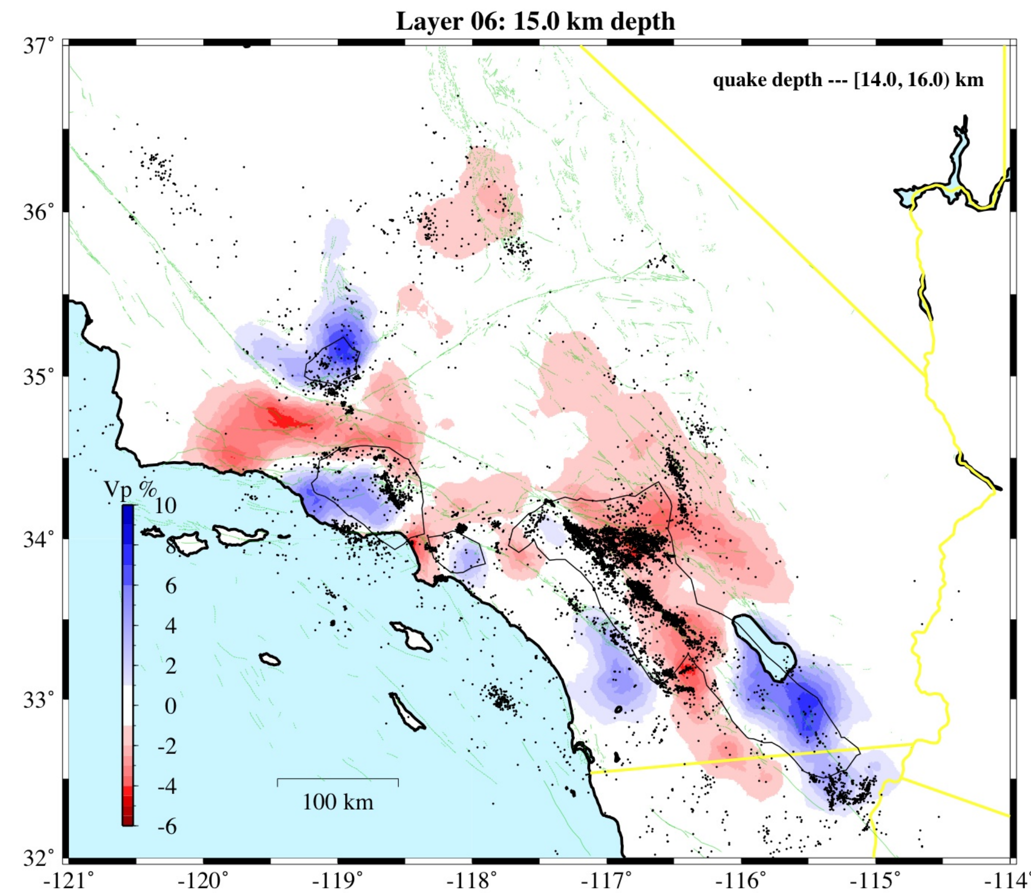

Figure 6.20. Seismicity between 14 and 16 km depth, compared to P velocity perturbations at 15 km. Fast regions are shown in blue and slow regions in red.

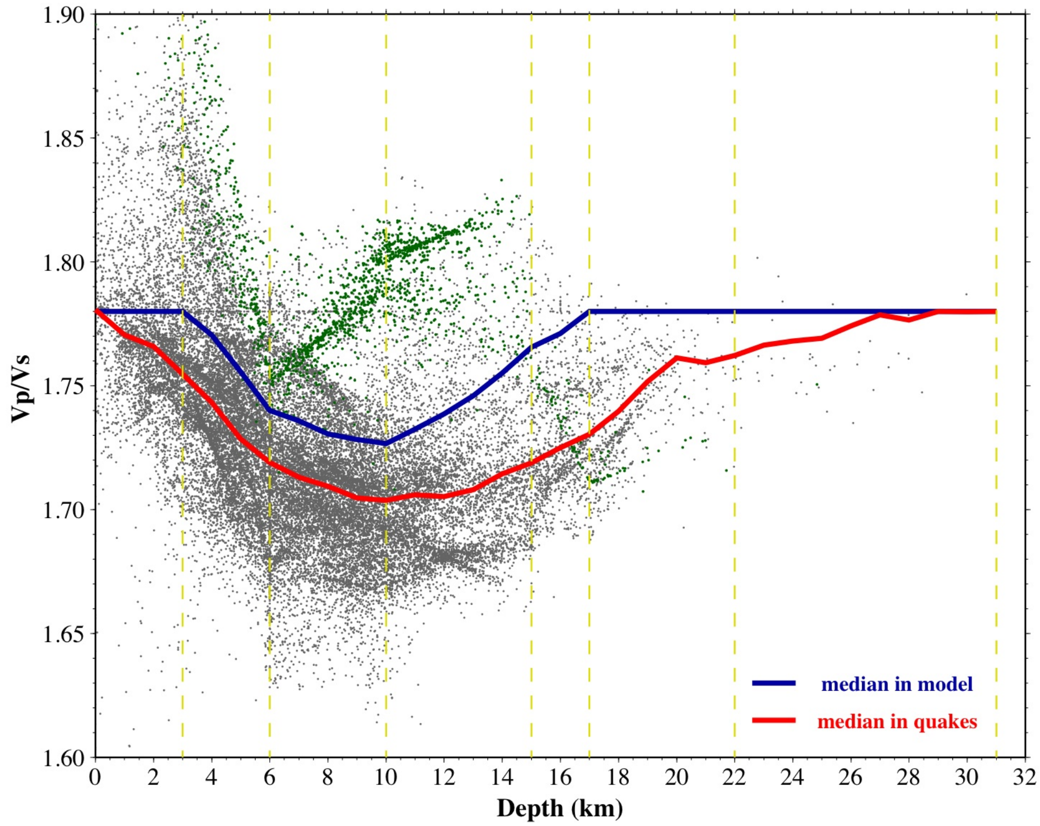

Figure 6.21. V_p/V_s versus depth. The dots are a random 10% of the entire earthquake set, with green indicating events from the 1994 Northridge aftershock sequence (see Figure 6.22). The red curve shows the median V_p/V_s values at the earthquake locations at 1 km depth intervals. For comparison, the blue curve shows the median of the tomography model over all well-resolved grid points.

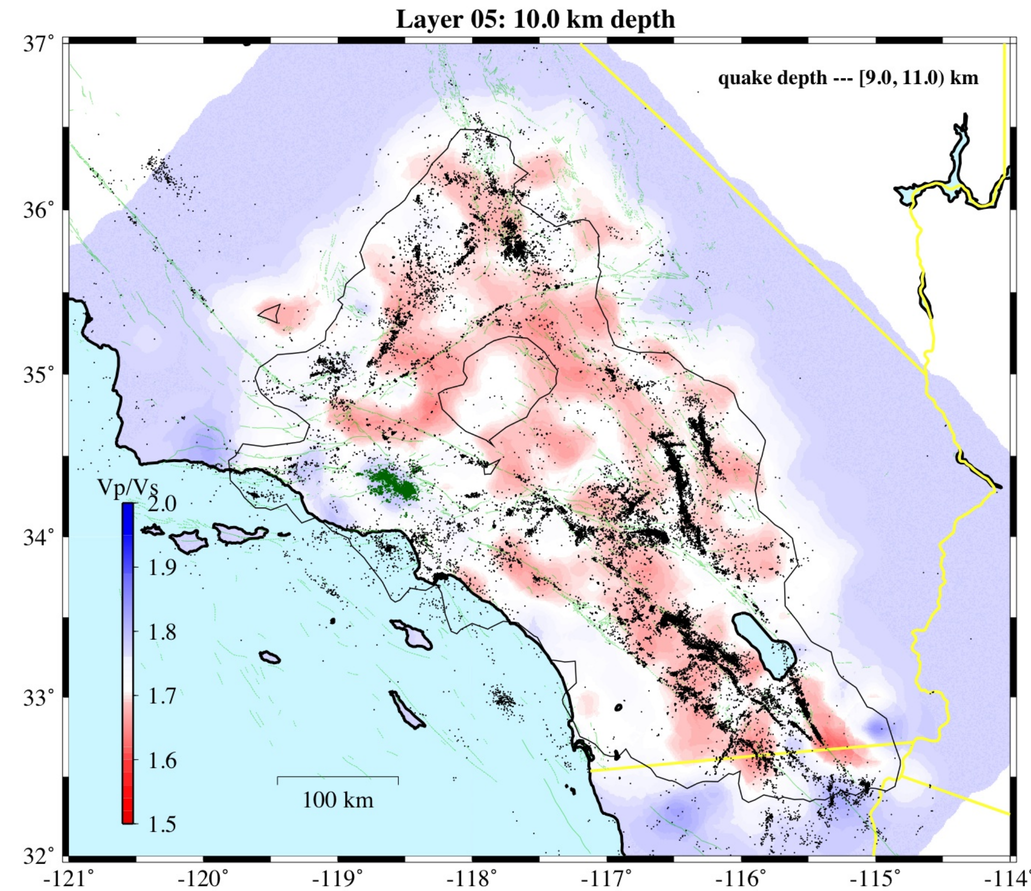

Figure 6.22. Seismicity between 9 and 11 km depth, compared to the V_p/V_s values at 10 km. High V_p/V_s regions are shown in blue and low V_p/V_s regions in red. The 1994 Northridge aftershock sequence is plotted in green.

depth, compared to the V_p/V_s perturbations in the tomography model. The earthquakes tend to avoid the regions with high V_p/V_s ratios, with the notable exception of the major aftershock sequences, such as that following the 1994 Northridge earthquake (shown as the green points in Figure 6.21 and Figure 6.22).

An association of seismically active regions with low V_p/V_s ratios is somewhat surprising because one might expect these regions to be more fractured and fluid filled than the surrounding crust, which would tend to increase the V_p/V_s ratio. However, because the resolution of our tomography model is very crude compared to the accuracy of the earthquake locations, it is possible that unresolved fine-scale structure in V_p/V_s may be present near seismically active areas that would yield very different V_p/V_s values near the earthquakes themselves. A promising way to study this possibility would be to directly estimate local V_p/V_s ratios within similar event clusters (Lin and Shearer, 2007).

6.8 Discussion

The main features in our model, in particular the low velocities in the sedimentary basins, have been seen in previous regional-scale tomographic models of the southern California crust (e.g. Magistrale *et al.*, 1992; Tanimoto and Prindle-Sheldrake, 2002; Zhou, 2004; Prindle-Sheldrake and Tanimoto, 2006). Our inversion method and the resulting model are most similar to the study by Hauksson (2000). The two models both resolve low velocity features at shallow depths in the basins and some high velocity features in the mid-crust. However, the lower crust P velocities in our model are slow relative to the values in Hauksson (2000). This is especially obvious in the cross-section plots (Figure 6.13 and Figure 6.14). Most of the velocities in our model are below 7.0 km/s, while in Hauksson (2000) almost all the profiles show high velocities (above 7.0 km/s) in the lower crust. These differences between the models may be a result of the damping parameters used in the tomographic inversions. We used SIMULPS damping parameters of 800 for the V_p model and 200 for the V_p/V_s model, which are higher than the values used in Hauksson (2000) (150 for V_p and 15 for V_p/V_s). As discussed earlier, we used larger damping parameters because we found the data misfit is not as sensitive as the model variance to the damping parameters. After we analyzed the tradeoff curves between the data misfits and model variances for both V_p and V_p/V_s, we found that relatively smooth models fit the data almost as well as much rougher models.

Another difference between our model and the Hauksson (2000) model is the resolution. We plot the resolution contours in both the map views and the cross-sections for our resolved regions with the SIMULPS resolution diagonal element above 0.1. This resolution is relatively low with respect to the 0.3 resolution contour in Hauksson (2000). In theory, the resolution can be increased by decreasing the damping parameters, but this may result in unreliable velocities. Considering the use of the composite event method, which maximizes the number of available stations for each event, we believe that our model is well-resolved. Different starting locations, initial velocity models and parameters used in the tomographic inversions could also cause the differences.

In some parts of southern California, the seismicity and station coverage is good enough that much higher resolution can be achieved in localized regions (e.g. Lees and Nicholson, 1993). The advantage of our model is that it provides uniform resolution across most of southern California and can be used for regional-scale analyses. Although we observe correlations between our model and some of the geological features on the surface, our model generally has poor resolution at shallow depths. In particular, the model overestimates the near-surface velocities in the sedimentary basins. For example, the slowest surface P velocity in our model is 3.6 km/s for the San Fernando Valley and 3.7 km/s in the Imperial Valley, whereas seismic refraction results (e.g. Lutter *et al.*, 2004; Fuis *et al.*, 1984) indicate surface velocities of 2.0 and 1.8 km/s, respectively. For earthquakes at depth, there is a tradeoff between the event origin times and the travel-time increase caused by slow near-surface layers. This tradeoff is removed to some extent by including the 36 calibration shots of known origin times in the inversion but we have too few of these events to fully cover southern California. In addition, shots often do not produce measurable S waves. We have 1349 P picks but only 19 S picks for the 36 shots. Thus, to obtain more accurate results for the shallow features, it is desirable to incorporate direct constraints on the velocity structure from other geophysical and geological data, an approach recently used by Magistrale *et al.* (2000) in southern California. However, these limitations in our model should not have a significant effect on the resolution of velocity anomalies at depth or for using the model to improve absolute earthquake locations.

6.9 Acknowledgments

All maps and cross-sections in this article were made using the GMT mapping tools. We thank Paul Wessel and Walter Smith for developing and supporting GMT. Funding for this research was provided by NEHRP/USGS grant 03HQPA0001 and the Southern California Earthquake Center, which is funded by NSF Cooperative Agreement EAR-0106924 and USGS Cooperative Agreement 02HQAG0008. The SCEC contribution number for this paper is 1050. Research is also supported in part by the U.S. Geological Survey, Department of the Interior, under USGS award numbers 06HQGR0055 and 07HQGR0050 to the University of Wisconsin-Madison. The views and conclusions contained in this document are those of the authors and should not be interpreted as necessarily representing the official policies, either expressed or implied, of the U.S. Government.

6.10 References

Dziewonski, A. M. (1984). Mapping the lower mantle: determination of lateral heterogeneity in P velocity up to degree and order 6. *J. Geophys. Res.*, **89**, 5929–5952.

Eberhart-Phillips, D. (1986). Three-dimensional velocity structure in the northern California Coast Ranges from inversion of local earthquake arrival times. *Bull. Seismol. Soc. Am.*, **76**, 1025–1052.

Eberhart-Phillips, D. (1990). Three-dimensional P and S velocity structure in the Coalinga region, California. *J. Geophys. Res.*, **95**, 15,343–15,363.

Eberhart-Phillips, D. (1993). Local earthquake tomography: earthquake source regions. *in: Seismic Tomography: Theory and Practice*, eds. H. M. Iyer and K. Hirahara, Chapman and Hall, London, 613–643.

Evans, J. R., D. Eberhart-Phillips and C. H. Thurber (1994). User's manual for SIMULPS12 for imaging Vp and Vp/Vs: A derivative of the "Thurber" tomographic inversion SIMUL3 for local earthquakes and explosions. *U. S. Geol. Surv. open-File Rep*, 94–431.

Fuis, G. S., W. D. Mooney, J. H. Healy, G. A. McMechan and W. J. Lutter (1984). A seismic refraction survey of the imperial valley region, california. *J. Geophys. Res.*, **89**, 1165–1190.

Gudmundsson, O., J. H. Davies and R. W. Clayton (1990). Stochastic analysis of global traveltime data: mantle heterogeneity and random errors in the ISC data. *Geophys. J. Int.*, **102**, 25–43.

Hadley, D. and H. Kanamori (1977). Seismic structure of the Transverse Ranges, California. *Geol. Soc. Am. Bull.*, **88**, 1469–1478.

Hauksson, E. (2000). Crustal structure and seismicity distribution adjacent to the Pacific and North America plate boundary in southern California. *J. Geophys. Res.*, **105**, 13,875–13,903.

Lees, J. M. and C. Nicholson (1993). Three-dimensional tomography of the 1992 southern California earthquake sequence: Constraints on dynamic earthquake rupture? *Geology*, **21**, 387–390.

Lin, G. and P. M. Shearer (2005). Tests of relative earthquake location techniques using synthetic data. *J. Geophys. Res.*, **110**, B04304, doi: 10.1029/2004JB003380.

Lin, G. and P. M. Shearer (2007). Estimating local Vp/Vs ratios within similar earthquake clusters. *Bull. Seismol. Soc. Am.*, in press.

Lin, G., P. M. Shearer and Y. A. Fialko (2006). Obtaining absolute locations for quarry seismicity using remote sensing data. *Bull. Seismol. Soc. Am.*, **96**, 722–728.

Lutter, W. J., G. S. Fuis, T. Ryberg, D. A. Okaya, R. W. Clayton, P. M. Davis, C. Prodehl, J. M. Murphy, V. E. Langenheim, M. L. Benthien, N. J. Godfrey, N. I. Christensen, K. Thygesen, C. H. Thurber, G. Simila and G. R. Keller (2004). Upper crustal structure from the Santa Monica Mountains to the Sierra Nevada, Southern Californnia: Tomographic results from the Los Angeles regional seismic experiment, phase II (LARSE II). *Bull. Seismol. Soc. Am.*, **94**, 619–632.

Magistrale, H., H. Kanamori and C. Jones (1992). Forward and inverse three-dimensional P wave velocity models of the southern California crust. *J. Geophys. Res.*, **97**, 14,115–14,135.

Magistrale, H., S. Day, R. W. Clayton and G. R. (2000). The SCEC southern California reference three-dimensional seismic velocity model version 2. *Bull. Seismol. Soc. Am.*, **90**, S65–S76.

Pavlis, G. L. and J. R. Booker (1980). The mixed discrete-continuous inverse problem: application to the simultaneous determination of earthquake hypocenters and velocity structure. *J. Geophys. Res.*, **85**, 4801–4810.

Prindle-Sheldrake, K. and T. Tanimoto (2006). Teleseismic surface wave study for S-wave velocity structure under an array: Southern California. *Geophys. J. Int.*, **166**, 601–621.

Richards-Dinger, K. B. and P. M. Shearer (2000). Earthquake locations in southern California obtained using source-specific station terms. *J. Geophys. Res.*, **105**, 10,939–10,960.

Shearer, P. M., E. Hauksson and G. Lin (2005). Southern California hypocenter relocation with waveform cross-correlation, Part 2: results using source-specific station terms and cluster analysis. *Bull. Seismol. Soc. Am.*, **95**, 904–915.

Spakman, W. and H. Bijwaard (2001). Optimization of cell parameterizations for tomographic inverse problems. *Pure and Applied Geophysics*, **158**, 1401–1423.

Spencer, C. and D. Gubbins (1980). Travel-time inversion for simultaneous earthquake location and velocity structure determination in laterally varying media. *Geophys. J. R. Astron. Soc.*, **63**, 95–116.

Tanimoto, T. and K. Prindle-Sheldrake (2002). Three-dimensional S-wave velocity structure in southern California. *Geophys. Res. Lett.*, **29**, 1223.

Thurber, C. H. (1983). Earthquake locations and three-dimensional crustal structure in the Coyote Lake area, central California. *J. Geophys. Res.*, **88**, 8226–8236.

Thurber, C. H. (1993). Local earthquake tomography: velocities and Vp/Vs-theory. *in: Seismic Tomography: Theory and Practice*, eds. H. M. Iyer and K. Hirahara, Chapman and Hall, London, 563–583.

Thurber, C. H., S. R. Atre and D. Eberhart-Phillips (1995). Three-dimensional Vp and Vp/Vs structure at Loma Prieta, California, from local earthquake tomography. *Geophys. Res. Lett.*, **22**, 3079–3082.

Zhou, H.-W. (2004). Multi-scale tomography for crustal P and S velocities in southern California. *Pure and Applied Geophysics*, **161**, 283–302.

Zhu, L. and H. Kanamori (2000). Moho depth variation in southern California from teleseismic receiver functions. *J. Geophys. Res.*, **105**, B2, 2969–2980.

The text of this chapter, in full, is a reformatted version of the material as it appears in Lin, G., P. Shearer, E. Hauksson and C. Thurber, A 3-D Crustal Seismic Velocity Model for Southern California from a Composite Event Method, submitted for publication in *Journal of Geophysical Research*, 2007. The dissertation author was the primary researcher and author. The co-authors directed and supervised the research which forms the basis of this chapter.

Chapter 7

Applying a 3D Velocity Model, Waveform Cross-Correlation, and Cluster Analysis to Locate Southern California Seismicity from 1981 to 2005

Abstract. We compute high-precision earthquake locations using southern California pick and waveform data from 1981 to 2005. Our latest results are significantly improved compared to our previous catalog (Shearer *et al.*, 2005) by the following: (1) We locate events with respect to a new crustal P and S velocity model using 3-D ray tracing, (2) We examine 6 more years of waveform data and compute cross-correlation results for many more pairs than our last analysis, (3) We compute locations within similar event clusters using a new method that applies a robust fitting method to obtain the best locations satisfying all the differential time constraints from the waveform cross-correlation. These results build on the relocated catalogs of Hauksson and Shearer (2005) and Shearer *et al.* (2005) and provide additional insight regarding the fine-scale fault structure in southern California and the relationship between the San Andreas Fault and nearby seismicity.

7.1 Introduction

Earthquake locations are fundamental parameters necessary for studies of earthquake physics and faulting and to map and quantify Earth's deformation. Studies of earthquake location improvements have been an important branch in seismology for the past few decades. To improve absolute location accuracy, we need knowledge of Earth's three dimensional velocity structure. For local earthquakes, this is usually done by simultaneously solving for a 3-D velocity model and earthquake locations (e.g., Thurber, 1983, 1992; Thurber and Eberhart-Phillips, 1999; Zhang and Thurber, 2003).

Recently, some techniques have been presented that are able to improve significantly the relative location accuracy among nearby events, even when the arrival times are biased by the effects of three-dimensional velocity structure (e.g., Richards-Dinger and Shearer, 2000; Waldhauser and Ellsworth, 2000; Nicholson *et al.*, 2004; Lin and Shearer, 2005). Improvements in relative location accuracy obtained using these methods often produce a dramatic sharpening of seismicity patterns. With the development of modern computers, waveform cross-correlation has also been an increasingly important tool for improving relative earthquake locations because of the great accuracy of differential times (Nakamura, 1978; Got *et al.*, 1994; Dodge *et al.*, 1995; Nadeau *et al.*, 1995; Gillard *et al.*, 1996; Rubin *et al.*, 1999; Waldhauser *et al.*, 1999; Hauksson and Shearer, 2005; Shearer *et al.*, 2005).

Improved earthquake locations help to improve resolution of fault structures and characterize the spatial and temporal characteristics of seismicity. High-resolution event catalogs in southern California have recently been used to study the decay of aftershock density with distance (Felzer and Brodsky, 2006), explore the spatial relationship between aftershocks and mainshock rupture planes (Liu *et al.*, 2003; Powers and Jordan, 2005), analyze the fractal dimension of seismicity (Kagan, 2006), and assess the mechanisms driving seismic swarms (Lohman and McGuire, 2006).

In this study, we build on our previous work with waveform cross-correlation location in southern California (Shearer, 1997, 1998; Astiz *et al.*, 2000; Astiz and Shearer, 2000; Shearer, 2002; Shearer *et al.*, 2003; Hauksson and Shearer, 2005; Shearer *et al.*, 2005) to process and relocate the complete southern California earthquake catalog from 1981 to 2005. This results in 6 more years of data than the 1984–2002

SHLK catalog (Shearer *et al.*, 2005). Although many of our methods are similar to our prior work, we have made some changes and developed several new algorithms to handle the larger number of events in the complete catalog. We now locate the events using a new 3-D P- and S- crustal velocity model for southern California and a new robust least-squares method to relocate events within similar event clusters using the waveform cross-correlation times. In addition, we include estimates of absolute and relative location errors. Our complete location procedure is outlined in the flow chart of Figure 7.1 and will be discussed in detail in the following sections.

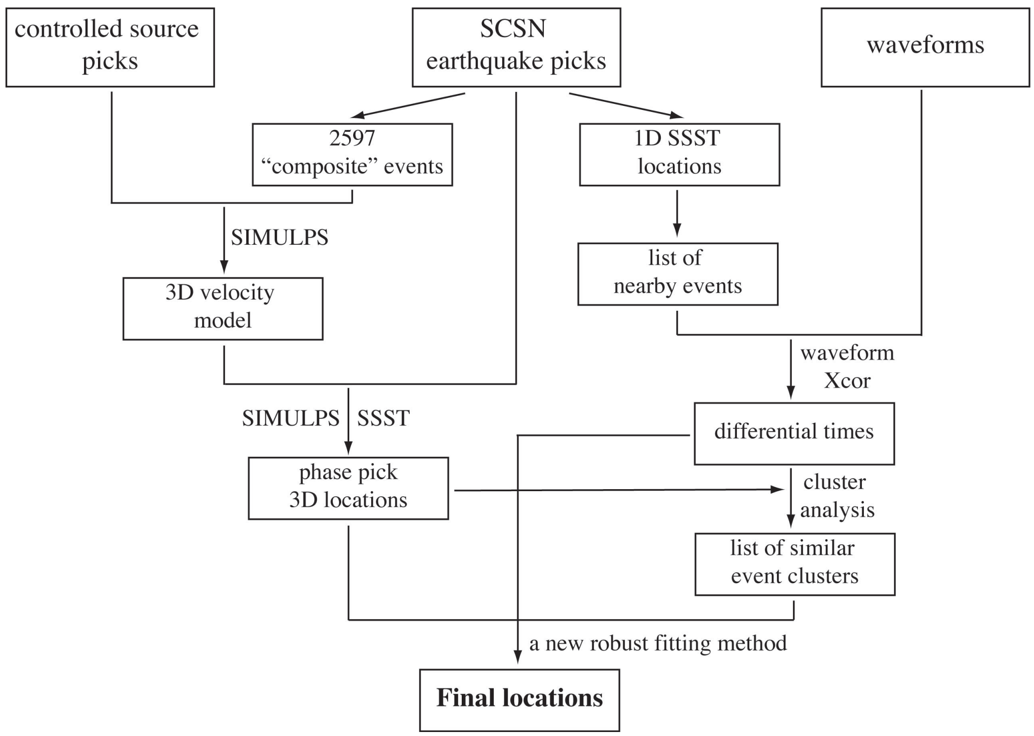

Figure 7.1. A workflow chart of our location procedures in this study.

7.2 Locations from Phase Picks and a 3-D Velocity Model

To obtain accurate absolute starting locations for waveform cross-correlation relocation, we use the new 3-D crustal P and S velocity models of Lin *et al.* (2007) to relocate all seismicity in southern California from 1981 to 2005 while keeping the velocity model fixed. We use the 3-D ray tracing capability

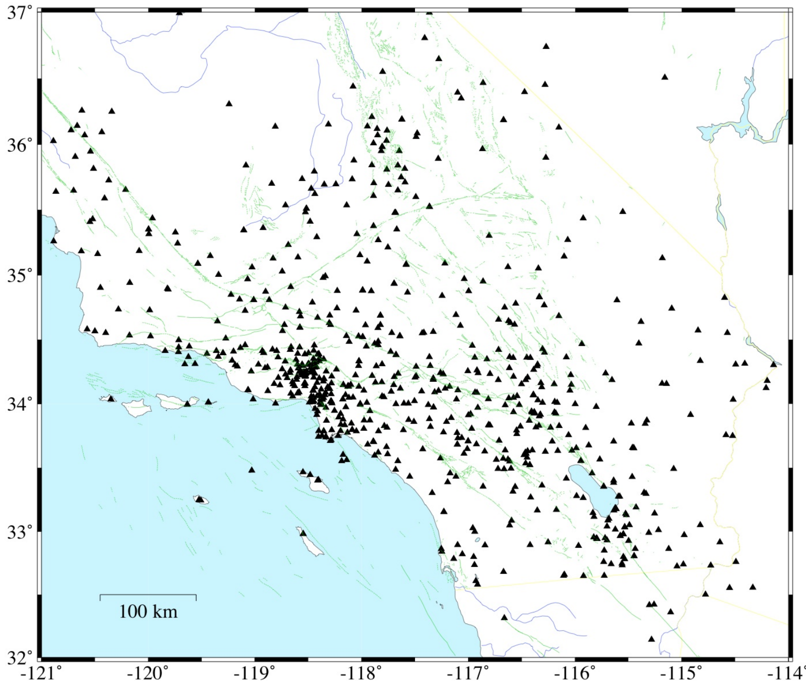

Figure 7.2. Locations of the 783 stations used in our study area.

of the SIMULPS algorithm (Thurber, 1983, 1993; Eberhart-Phillips, 1990; Evans *et al.*, 1994) to compute locations for all events with respect to the tomography model while iteratively adjusting the pick times using a source-specific station term approach (Richards-Dinger and Shearer, 2000; Lin and Shearer, 2005) to improve the relative locations among nearby events.

7.2.1 Data Sets

Our data for the initial event locations are the phase arrival times of *P* and *S* waves from 452,943 events, including local events, regional events and quarry blasts, recorded at the Southern California Seismic Network (SCSN) stations and picked by the network operators. Figure 7.2 shows the station locations in our study area. We require each event to have at least 5 observations (P and S–P picks) from stations within a 150 km distance cutoff. This results in about 430,000 events to be relocated using 3-D ray tracing. To refine the relative locations among closely spaced events, we combine the 3-D ray tracing with the source-specific station term relative location method.

7.2.2 Shrinking Box Source-Specific Station Term Method

The source-specific station term (SSST) method improves relative event locations among nearby events using phase arrival times (Richards-Dinger and Shearer, 2000; Lin and Shearer, 2005). This method attempts to correct for the systematic biases in arrival times caused by three-dimensional velocity variations without actually solving for the velocity structure itself. The station corrections are calculated for each source-receiver pair at a given station using the residuals from nearby events within a given distance cutoff separately for P and S, so the station correction varies as a function of source position. The station term part of the calculation is separate from the event location so the method can be applied using any desired location technique. The shrinking box SSST is an extension of the simple SSST in that it computes the SSST terms while continuously shrinking the cutoff distance between the first and final iteration. For more details, please refer to Lin and Shearer (2005).

7.2.3 Combination of 3-D Ray Tracing with SSST

The crustal structure in the 3-D velocity model provides improved absolute hypocenter locations by correcting for the biasing effects of large-scale velocity variations. However, the tomography model is relatively smooth and cannot account for small-scale velocity structure that can also introduce bias and scatter in event locations. Thus to further refine the event locations, we combine the shrinking box SSST method and 3-D ray tracing in Thurber's SIMULPS computer algorithm. Our strategy is to first relocate all seismicity using the 3-D ray tracing, then compute SSSTs for each individual pick from the travel-time residuals of nearby events. Next, we subtract the SSST terms from the arrival-time picks, and repeat the 3-D relocations with the new travel-time data. We perform 6 iterations of 3-D location and SSST computation. The distance cutoff for the station term calculation is reduced gradually during the iterations from 100 km to 10 km. We find that this approach converges quickly to a stable set of locations and station terms. Figure 7.3 shows the reduction of the travel-time residual median-absolute-deviation (MAD) from the 430,000 events with iteration number in our SSST calculation. The MAD of the residuals drops from 0.048 s to 0.029 s. For comparison, the root-mean-square (RMS) residual decreases from 0.16 to 0.12 s. The event locations at this point represent our best estimates based on phase pick data alone without the further improvements that are possible using differential times from waveform cross-correlation.

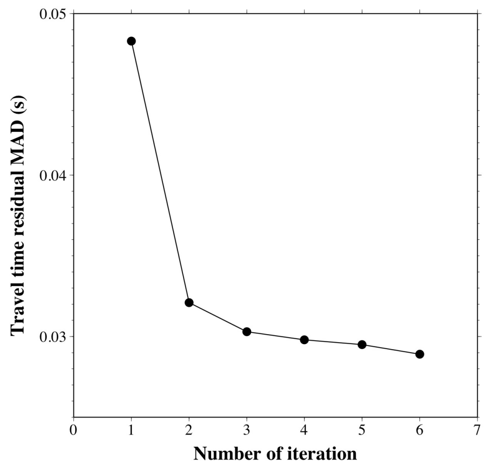

Figure 7.3. Reduction of traveltime residual MAD with iteration numbers of SSST calculations.

7.3 Waveform Cross-Correlation

The waveforms of nearby earthquakes recorded at the same station are often similar enough that waveform cross-correlation can be used to obtain much more precise differential times than can be picked on individual seismograms, in which case greatly improved relative locations among the events can be computed. The waveform cross-correlation process in this study is similar to that described in Hauksson and Shearer (2005) and Shearer *et al.* (2005).

7.3.1 Waveform Data Processing

We obtain waveform data from the SCSN, as archived at the Southern California Earthquake Data Center (SCEDC) for all available local events, regional events and quarry blasts in southern California from 1981 to 2005. We use the Seismic Transfer Program (STP) (www.data.scec.org/STP/stp.html) to extract the waveforms in Seismic Analysis Code (SAC) format (www.llnl.gov/sac/). We obtain all components (e.g., vertical, east, west) and channels (short-period, broadband, etc.) contained in the database archive. Our first step is to trim the seismograms to 60 s, starting 10 s before the theoretical P-arrival time. We store the resulting time series using the event-based GFS format (G. Masters, personal comm., 2006) within a year/month directory structure. Following these steps, the GFS files consume about 626 Gb on an online Redundant Array of Independent Disks (RAID) system that provides rapid and random access to the data. We then resample the data to a uniform 100-Hz sample rate (using a spline interpolation method) and apply a bandpass filter between 1 and 10 Hz.

7.3.2 Waveform Cross-Correlaion Calculation

It is computationally infeasible to cross-correlate every event pair for all 450,000 events because the size of the problem scales as $n(n-1)/2$. Thus, we restrict the calculation to event pairs separated by less than 2 km. However, to ensure a significant number of pairs even in regions of sparse seismicity, if the number of events within 2 km of an event is less than 100, we add additional events defined using a Delaunay tesselation (Richards-Dinger and Shearer, 2000) of our catalog until we have at least 100 neighboring events. We define the neighboring events using an event catalog based on 1-D locations using the shrinking box SSST method (at this point we had not yet computed the locations based on the 3-D model). Although the absolute location accuracy of this initial catalog is limited by the use of a 1-D model (the model used in Shearer *et al.*, 2005), the relative location accuracy is sufficient for us to use these locations to identify similar event pairs. In total we compute cross-correlation functions for all available station and components for over 94 million event pairs, about 7 times more pairs than we computed previously for the SHLK catalog (Shearer *et al.*, 2005).

We compute the cross-correlation functions separately for P and S waves, applying symmetric time shifts of up to ± 1.5 s, using a spline interpolation method to achieve a nominal timing precision of 0.001 s (1 ms). If catalog picks are available, we use a 1.5 s window around P and a 2.5 s window around S. If picks are not available, we estimate arrival times from the earthquake location and a simple 1-D model, using a 2-s P window and a 3-s S window. Our pick windows are designed to avoid including part of the S wave in the P window or part of the P wave in the S window.

Information is saved only for the 31 million event pairs with an average waveform correlation coefficient of 0.45 or greater and with at least 10 individual differential times with correlation coefficients of 0.6 or greater. The resulting correlation coefficients and time shifts contain information regarding the similarity of events and their relative locations. In our previous study (Hauksson and Shearer, 2005; Shearer *et al.*, 2005), we used roughly the same criteria and obtained correlation information for about 3 million pairs of events. The ten-fold increase in usable pairs reflects the greater number of pairs computed (6 more years of data and more pairs per target event) and an increased yield of correlated pairs (obtained because a greater fraction of the pairs are separated by distances of less than 2 km). A variety of different methods can be applied to analyze cross-correlation data. In this study, we apply a cluster analysis method similar to that described in Shearer *et al.* (2005).

7.4 Similar-Event Cluster Analysis

The next step in our processing is to use the waveform cross-correlation results to identify clusters of similar events. The output of the cross-correlation calculation contains information about the similarity of selected pairs of events. Based on our experience, we adopted the criteria that the event pair must have 8 or more P or S measurements with correlation coefficients above 0.65 for stations within 80 km of the events. There are often several measurements from different components of the same station. We remove this redundancy before applying our selection criteria by favoring P measurements from the vertical component and S measurements from the horizontal components, and then selecting the measurement with the highest correlation. For those event pairs that exceed our similarity cutoff, we compute the mean correlation coefficient of the individual P and S values to use as an overall measure of the similarity of the pair. Next, we apply a cluster analysis approach (Hartigan, 1975) to identify groups of events that are correlated with each other. Then we use the waveform cross-correlation times to relocate the 323,000 events in 3,676 similar event clusters with more than 5 events.

7.5 Differential-Time Relocation Method

We use the differential times from the waveform cross-correlation to relocate events within each similar event cluster in order to further improve the relative event locations. Here we describe a new method for computing these locations, which has some advantages compared to the technique we applied previously for the SHLK catalog (Shearer *et al.*, 2005). The cartoons in Figure 7.4 show how our method works. In this example, there are 10 events, shown by the red circles, in a similar event cluster centered at the star in Figure 7.4a. Each event is linked with some, but not all, of the other events in the cluster by differential times. The event number is sorted chronologically. We start with event 1, which is linked with 7 other events in this example. We apply a grid-search algorithm to find the best location of event 1 (shown by the green circle) that minimizes the robust least-squares (Lin and Shearer, 2007) of the differential-time residuals while keeping the locations of the 7 neighboring events fixed. The new fitting method measures distance using the L_2 norm for data misfits below some specified value, d_{max} (which in general will depend on the observations), and the L_1 norm for larger values. This hybrid $l^1 - l^2$ error measure was proposed by Huber (1973) and is relatively insensitive to outliers in data, so we term it the "robust least squares" method. This robustness is important because we want to use as many differential times as possible, even at the risk of including some falsely correlated waveforms that produce large residuals. We relocate other events in the cluster in the same way except that we use the updated locations of the neighbors (see the relocation of event 2 in Figure 7.4b). After one iteration, all the event locations in the cluster are updated to the green circles in Figure 7.4c. Usually the centroid of the relocated cluster (the green star) is slightly different than the initial centroid (the red star). To stabilize the inversion and because the differential times are only very weakly sensitive to the absolute cluster location, after each iteration we shift the entire cluster so that the new centroid of the cluster is the same as the centroid of the starting locations, shown in Figure 7.4d. Thus the absolute cluster locations remain constrained by the locations based on the P and S picks and computed from ray tracing through the 3-D model. We repeat this process with the updated locations for a few iterations and generally observe rapid convergence to a stable set of locations (Figure 7.4e) that does not depend upon the initial event ordering. Using this method, we separately relocate each of the 3,676 similar event clusters in southern California.

For computational reasons, to compute the theoretical times for these differential locations, we use a 1-D velocity model (Figure 7.5), which is the layer-averaged model from the new 3-D model in Lin *et al.* (2007). However, because this 1-D model is used only for differential locations based on differential times, most of the biasing effects of 3-D velocity structure are removed and we expect that very similar results would be obtained using a 3-D model. To test the sensitivity of our differential locations to changes in the velocity model, we computed results for some clusters using a different 1-D velocity model (that of Shearer *et al.*, 2005) and found only very small differences to the results presented here. The absolute locations of each cluster, of course, remain fixed at the cluster centroids as determined by ray tracing through our 3-D velocity model.

$M \geq 4$ earthquakes generally do not cross-correlate well with smaller events because of their more complicated waveforms and frequent clipping of their records. However, we found that often our automated processing method would assign these large events to a similar event cluster and relocate them based on a small number of spurious cross-correlations with other events. We do not believe these locations are reliable and therefore we replaced the locations for the 896 local $M \geq 4$ events in our final catalog with their 3-D locations obtained using the shrinking box SSST method. It is possible that more careful culling of the waveform data would allow these events to be relocated to greater accuracy but we do not attempt this here.

7.6 Relocation Results

Figure 7.6 maps the final relocated seismicity for about 430,000 events from 1981 to 2005. Black dots show similar event clusters relocated using cross-correlation data. The distribution of similar event clusters is similar to those in Shearer *et al.* (2005). About 25% of events do not correlate within clusters of at least 5 events and are plotted in color by year at their 3-D locations (24%) or 1-D locations (1%) if the 3-D locations are not available. For comparison, about 60% of the events in the SHLK catalog are in similar event clusters. According to Schaff and Waldhauser (2005), approximately 95% of the northern

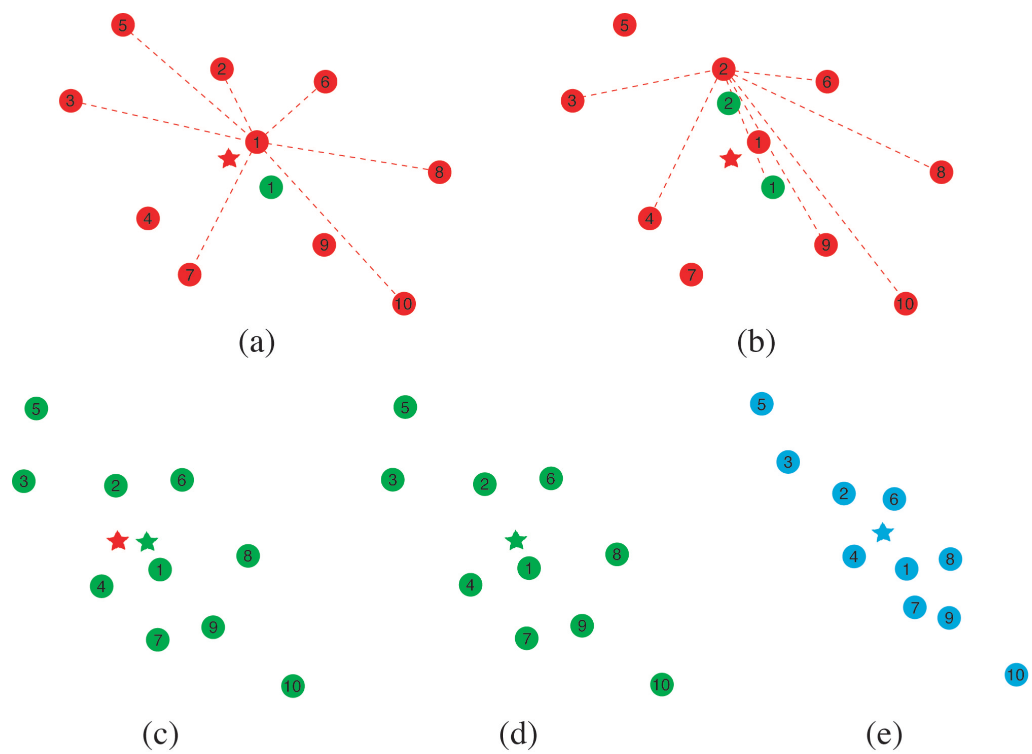

Figure 7.4. Cartoons showing our new differential time location method. (a) The red circles represent the starting locations for the 10 events in a similar event cluster. The star is the centroid of the cluster. After fitting the differential times between event 1 and the linked events, event 1 is shifted to the green circle. (b) Relocation of event 2 using the new location of event 1 if they are correlated with each other. (c) Distribution of the cluster after all the events are relocated shown by the green circles. Note the new centroid of the cluster (the green star) is different than the starting centroid. (d) Shifted cluster location centered at the starting centroid. (e) The final locations for this cluster after repeat (a)-(d) for a few iterations.

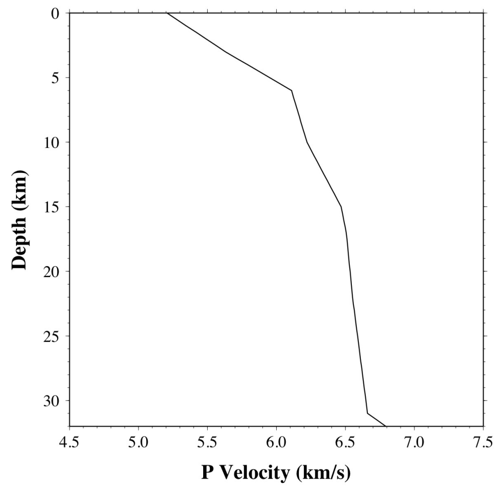

Figure 7.5. The P velocity model used for calculating theoretical travel times during cross-correlation relocation.

California seismicity includes events that have cross-correlation coefficients greater that 0.7 with at least one other event recorded at four or more stations. While the fraction of similar events depends to some extent on the details of the waveform similarity criteria required to define similar-event pairs, it does appear that southern California seismicity is less likely to occur in similar event clusters than northern California seismicity.

7.7 Comparisons Between Location Catalogs

In this section, we compare locations of local events from six recent catalogs for southern California seismicity, including: (1) the standard catalog of 408,105 local events from 1981 to 2005 located by the SCSN using a layered 1-D velocity model for southern California; (2) the Richards-Dinger and Shearer (2000) catalog (referred as the RDS catalog) including 288,912 events from 1981 to 1998 relocated using a 1-D gradient velocity model and the SSST method; (3) the Hauksson (2000) catalog (referred as the HAUKSSON_3D catalog) including 342,112 events from 1981 to 2000 relocated using a 3-D velocity model for southern California; (4) the Hauksson and Shearer (2005) catalog (referred as the HAUKSSON_DD catalog) including 327,430 events from 1984 to 2002 relocated using the double-difference (DD) location method (Waldhauser and Ellsworth, 2000; Waldhauser, 2001) and waveform

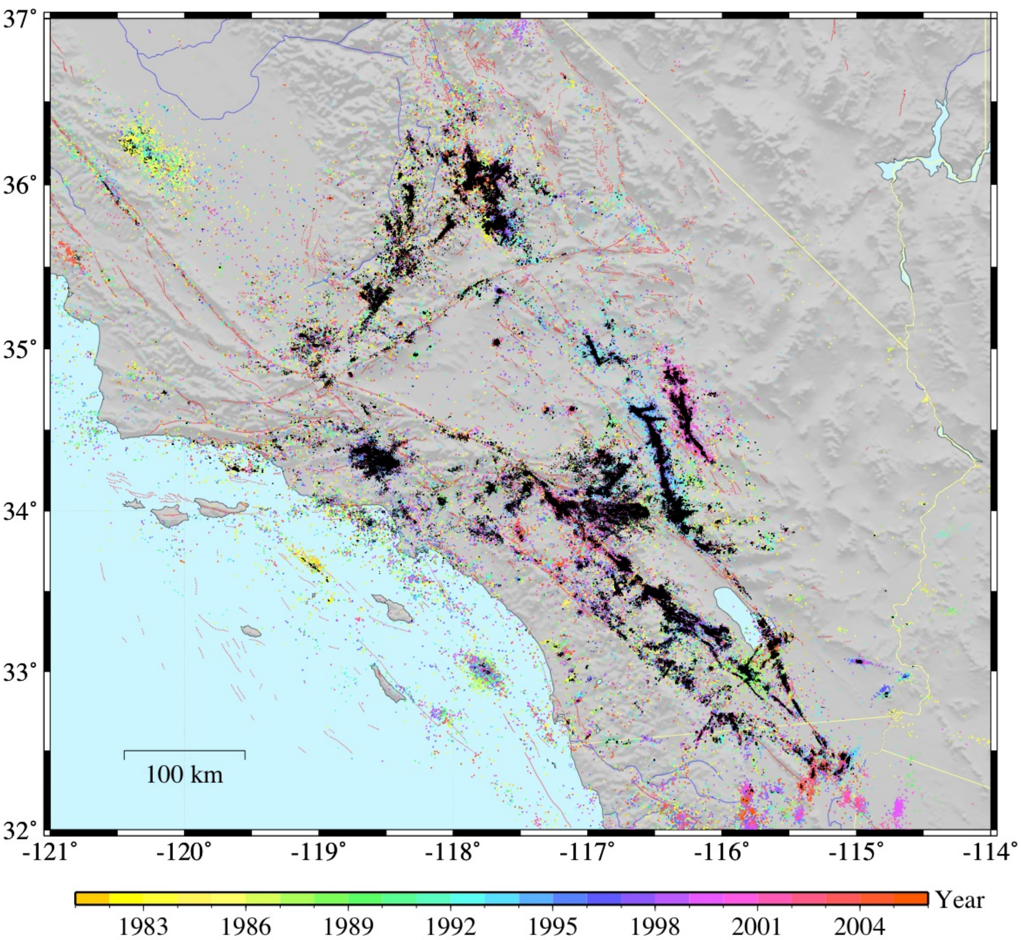

Figure 7.6. Map view of the relocated seismicity from 1981 to 2005 in our study. Black dots show similar event clusters relocated using cross-correlation data. About 25% of events do not correlate and are plotted in color by year at their 3-D locations or 1-D locations.

cross-correlation based on the 3-D initial locations (Hauksson, 2000); (5) the SHLK catalog by Shearer *et al.* (2005) including 316,020 events from 1984 to 2002 relocated using the 1-D SSST method, similar event cluster analysis and waveform cross-correlation data; and (6) the new locations presented in this study (referred as the LSH catalog) including 399,521 events from 1981 to 2005 using cluster analysis, waveform cross-correlation data and a new robust differential time location method based on 3-D starting locations.

7.7.1 Depth Distribution

First, we compare histograms of depth distributions from the six catalogs in Figure 7.7. In the SCSN catalog, there is a big peak at 6 km depth, which may be due to the velocity discontinuity at 6 km depth in the layered velocity model. The RDS catalog was obtained based on a 1-D gradient velocity model and a SSST relative location method. Due to the relatively fast near-surface velocity in this model, this catalog has more events located between 0 and 3 km depth. For the HAUKSSON_3D catalog, because of the simultaneous inversion of earthquake locations and velocity perturbations, the distribution of depths is very smooth. Based on this catalog, the relative locations are refined by the double-difference location method and waveform cross-correlation data in the HAUKSSON_DD catalog. There is a small peak in this catalog at 6 km depth, which might be due to the sharp change in the velocity slope at 6 km depth in the 1-D velocity model (see Hauksson and Shearer (2005), Shearer *et al.* (2005)). There is also a small drop at about 9 km, which might be caused by the inconsistency between the 3-D and 1-D velocity models used for the 3-D and DD locations. The distribution of the SHLK catalog is similar to the RDS catalog for depths more than 10 km and has fewer shallower events. Our new LSH location catalog has depths similar to that of both HAUKSSON_DD and SHLK. At shallow depths ($<$ 6 km), it is similar to the HAUKSSON_DD, whereas deeper it is similar to SHLK. This is reasonable because our new locations are based on a 3-D velocity model (as in the HAUKSSON_DD), cluster analysis and waveform cross-correlation (same as in the SHLK). However, the distribution in our new catalog is more uniform, especially for shallower depths.

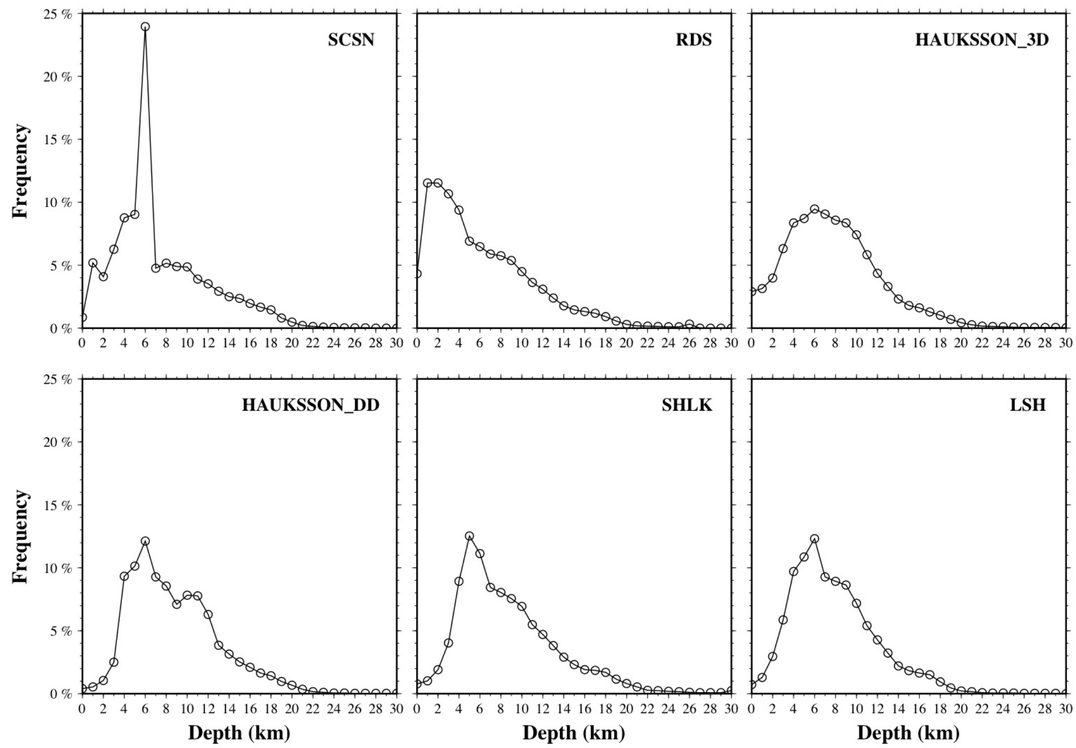

Figure 7.7. Histograms of depth distributions for 6 different southern California seismicity catalogs.

7.7.2 The Imperial Valley Region

In our previous catalog (Shearer *et al.*, 2005), we used a custom 1-D velocity model to obtain a more accurate set of hypocenters for the Imperial Valley, due to the substantially different velocity structure in this large sedimentary basin compared to the rest of southern California. In order to test the effectiveness of our 3-D model in accounting for this anomalous structure, we compare both the epicenter and depth distributions for this region from four catalogs. Figure 7.8 shows the map view of the seismicity for this region from (a) the SCSN catalog; (b) the LSH catalog in this study; (c) the SHLK catalog using the 1-D model for southern California (see Figure 1(a) in Shearer *et al.* (2005)); and (d) the SHLK_IMP_1.0 catalog using the 1-D model derived from refraction seismic experiments (see Figure 1(b) in Shearer *et al.* (2005)). The red and green straight lines are the profiles for the cross-sections shown in Figure 7.9. In

Figure 7.8, the relocated seismicity in (b), (c), and (d) is sharper than in the standard SCSN catalog. We observe differences in absolute locations for some clusters in this region between the LSH catalog and the SHLK and SHLK_IMP_1.0 catalogs that are due to the 3-D ray-tracing; however, the relative locations are very similar. The absolute locations in the new LSH catalog are preferred because only ray tracing through a 3-D model can correctly account for the strong lateral velocity changes at the edges of the Imperial Valley. The biases from different 1-D velocity models are likely to be strongest in depth. Figure 7.9 presents the cross-sections of the seismicity within 10 km of the profiles shown by the straight lines in Figure 7.8. The relocated seismicity is much sharper than the SCSN catalog. The new locations and those in the SHLK_IMP_1.0 catalog appear more stable than those in the SHLK catalog and more tightly clustered. Note the similarity between the new LSH catalog and the SHLK_IMP_1.0 catalog, which suggests that the 3-D velocity model produces reasonably unbiased absolute locations. We therefore do not apply a separate velocity model for the Imperial Valley region in our new study.

7.8 Location Error Estimates

Our new locations produce a dramatic sharpening of seismicity features compared to standard catalogs and a significant sharpening of some features compared to our previous SHLK catalog. Presumably this sharpening indicates decreased location errors because there is nothing intrinsic to our algorithms that should cause linear seismicity alignments. However, it is desirable to compute quantitative estimates of likely location errors for individual events. In order to do this, we estimate the absolute and relative location errors separately.

7.8.1 Absolute Location Errors

The SIMULPS algorithm (Evans *et al.*, 1994) provides the hypocenter error ellipse. It computes the errors as the largest of the horizontal and vertical projections of the principal standard errors for each single event. Because we keep the absolute location of each similar event cluster fixed during the waveform cross-correlation relocation, we use the hypocenter errors from the output of the 3-D relocation

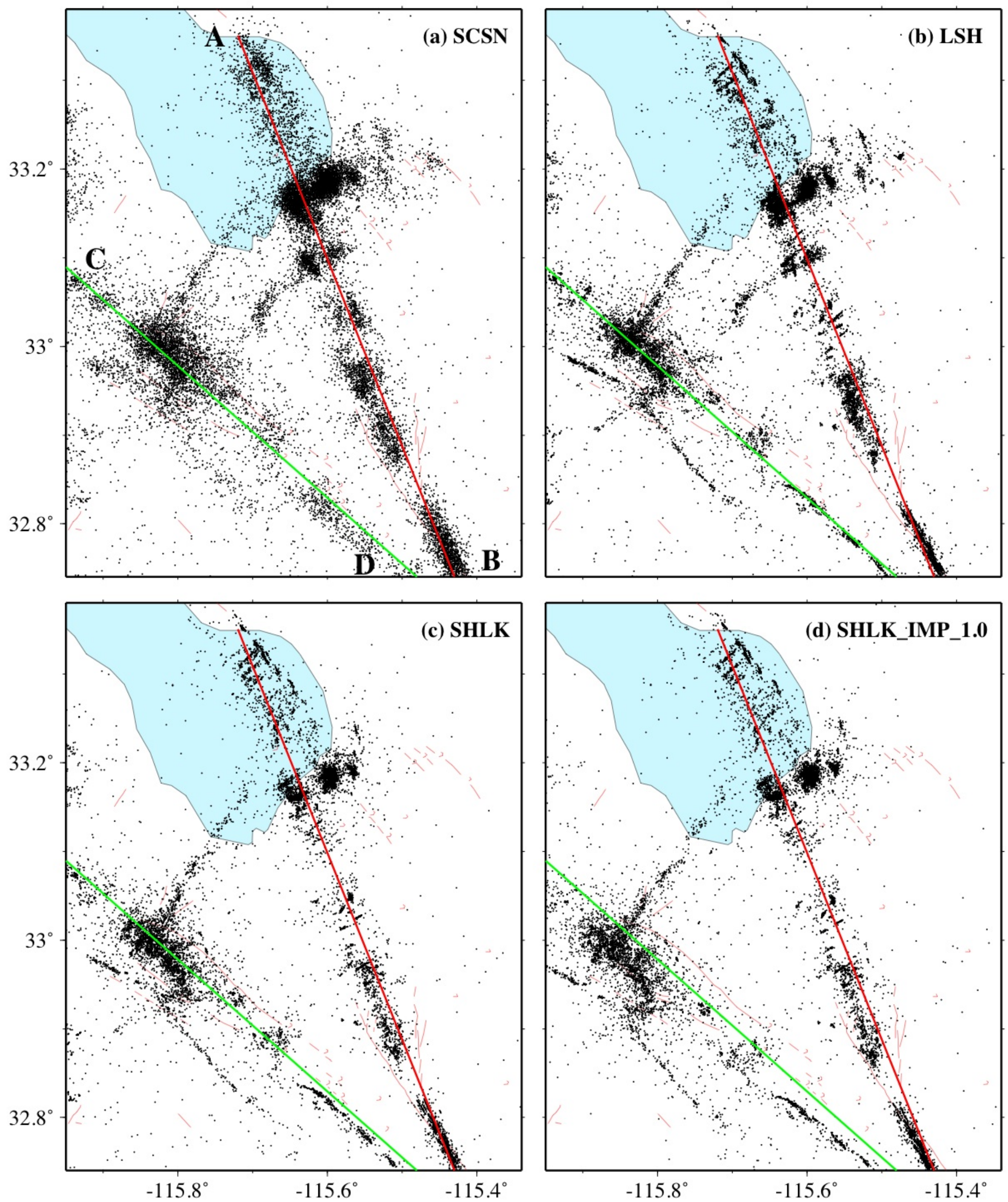

Figure 7.8. Epicenter distributions for the Imperial Valley region from (a) the SCSN catalog; (b) the new LSH catalog in this study; (c) the SHLK catalog using the 1-D model for southern California (see Figure 1(a) in Shearer *et al.* (2005)); (d) the SHLK_IMP_1.0 catalog using the 1-D model derived from refraction seismic experiments (see Figure 1(b) in Shearer *et al.* (2005)). The red and green straight lines are the profiles for the cross-sections shown in Figure 7.9.

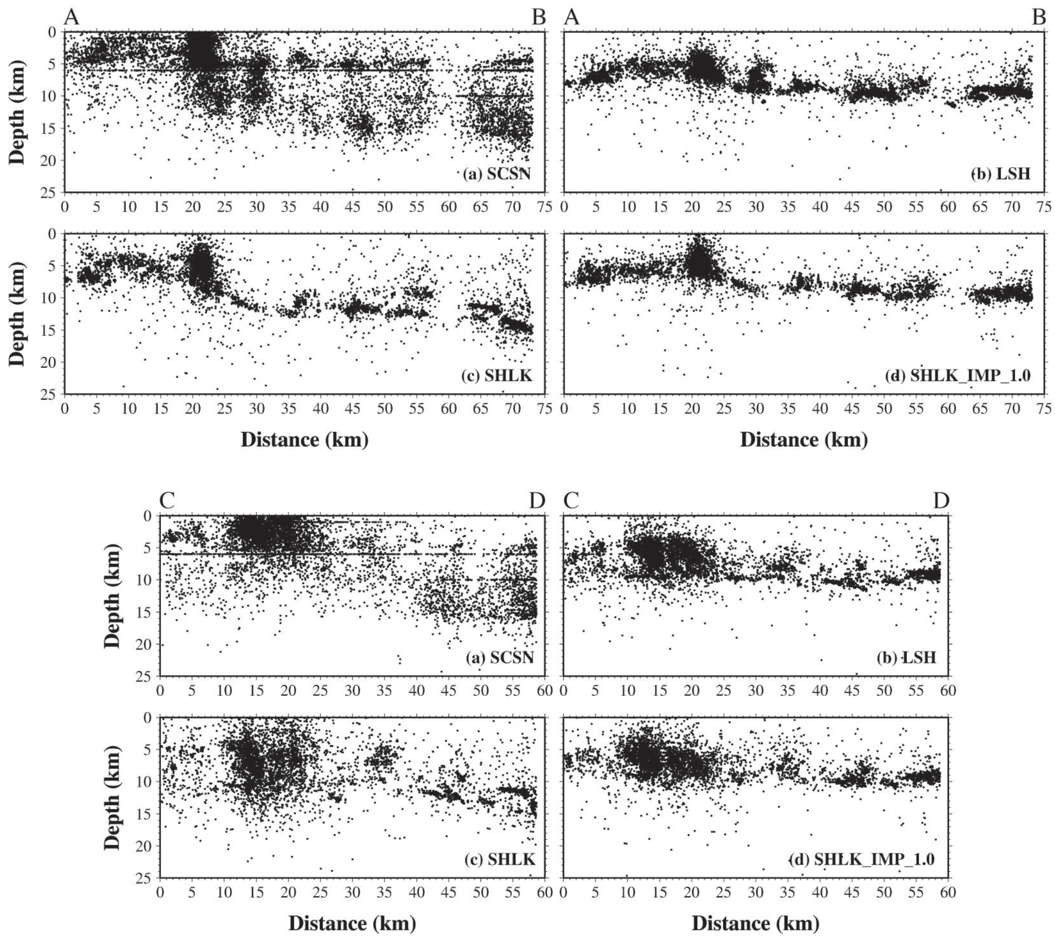

Figure 7.9. Cross-sections of the seismicity within 10 km of the profiles shown in Figure 7.8 in the four location catalogs.

to provide estimates of the absolute location errors in our catalog. The absolute location error in horizontal and vertical is given for each single event. We plot histograms of the hypocenter errors for the 430,000 events in Figure 7.10. The MAD of the horizontal errors is 0.1 km, and 0.2 km for the vertical errors. (The RMS of the horizontal errors is 0.5 km, and 1.1 km for the vertical errors.) These should be considered minimum errors because they represent the formal statistical errors in the solution and do not fully account for the possibility of errors in the velocity model or other systematic biases.

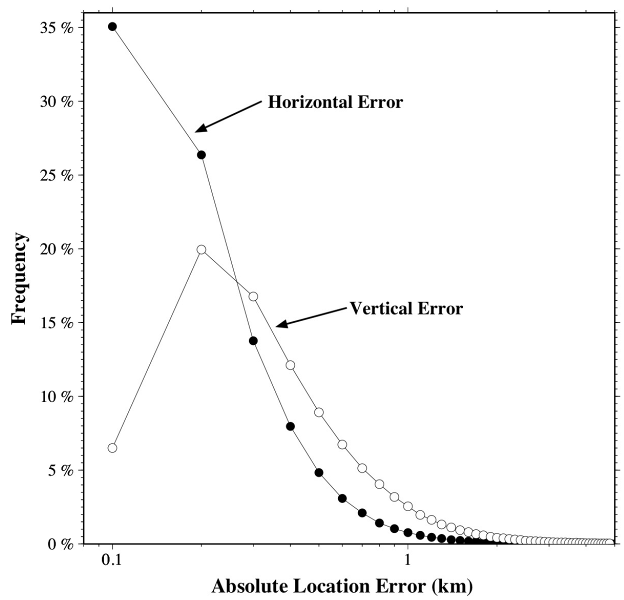

Figure 7.10. Histograms of absolute hypocenter errors from the SIMULPS results for the 430,000 relocated events. The MAD is 0.1 km for the horizontal errors and 0.2 km for the vertical errors.

We also used the 3-D velocity model to independently relocate the hypocenters and origin times of the 36 shots with known locations and origin times used in Lin *et al.* (2007) . Figure 7.11 shows the location errors for these shots. Except for 3 of the 36 events, all events have epicenter errors less than 1.5 km, with most errors less than 1.0 km. The 3 exceptional events have epicenter errors of about 2.8 km. For the vertical location errors, 30 are less than 3.0 km, and with most are less than 2.0 km. The others are about 6.0 km. For the 36 shots used here, the number of P picks is 1,349, but the the number of S picks is only 19. Considering this aspect and also the rapid velocity variations in the near surface, the absolute

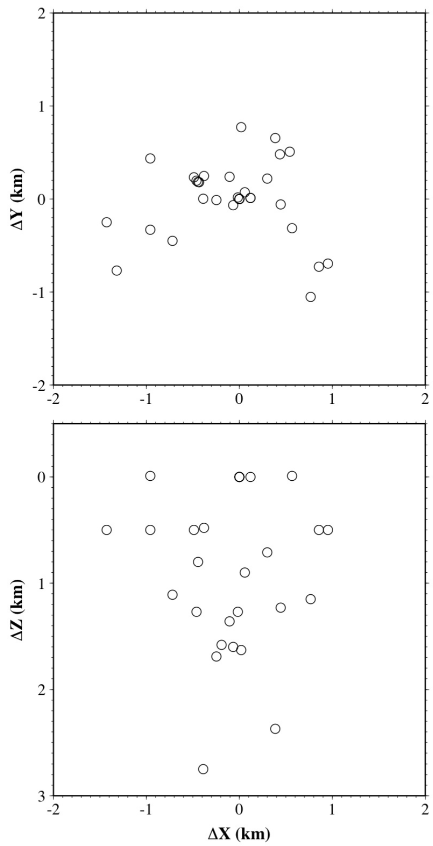

Figure 7.11. Location errors for the 36 shots used in the tomographic inversions and relocated in the new 3-D velocity model.

location errors from these shots can be treated as the maximum likely errors in our location catalog.

7.8.2 Relative Location Errors

Within each similar event cluster, we apply a grid-search algorithm using the robust least-squares method to relocate all the events. Because we do not use the L_2 norm, it is not possible to compute error ellipses based upon the χ^2 misfit criteria of the classical least-squares method. As an alternative, we have applied a bootstrap approach (Efron and Gong, 1983; Efron and Tibshirani, 1991), in which the differential times for each event are randomly resampled (individual times may be sampled multiple times or not sampled at all). This process is repeated for 20 subsamples for each event and we relocate each event using the resampled differential times. We estimate the standard deviations of these 20 subsamples as the standard errors of the relative locations for each event. However, it should be noted that these formal statistical uncertainties can be quite small when the number of data points is large. Again, we plot the histograms of the relative errors in both horizontal and vertical locations from 323,000 cross-correlation relocated events in Figure 7.12. The MAD is 10 m for the relative horizontal location error and 21 m for the vertical location error. More accurate individual error estimates could be obtained by performing more than 20 bootstrap resamplings (limited computing time prevented us doing this), but the overall statistical properties of the estimated errors over many events should be reliably obtained even with a limited number of resamplings. It is possible that a faster method of estimating relative location errors could be obtained by more direct methods, such as studying the size and shape of the individual event misfit functions, but we do not attempt this here.

In general, our estimated absolute location errors are similar to the HAUKSSON_3D catalog and the relative location errors are comparable to the SHLK catalog.

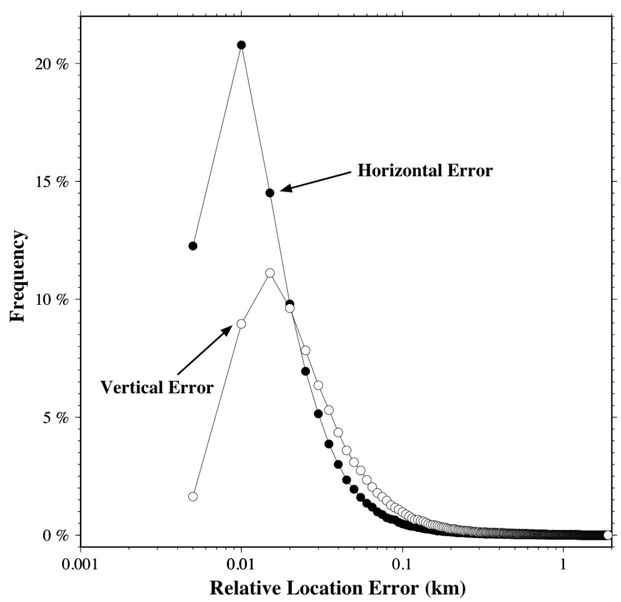

Figure 7.12. Histograms of relative location errors from bootstrap resampling for the 323,000 cross-correlation relocated events.

7.9 Discussion

Our new catalog is available through the Southern California Earthquake Data Center and we anticipate that it will be useful to a variety of researchers studying seismicity and tectonics in southern California. In particular our improved locations should help to resolve details of fine-scale fault structure in regions of active seismicity. One important question is the exact relationship between small earthquakes and major faults (e.g., Hauksson *et al.*, 2006). Is the seismicity near these faults actually on the fault surface or on nearby subsidiary faults? A comprehensive study of this question is beyond the scope of this paper. However, we will highlight results from our catalog for two portions of the San Andreas Fault (SAF).

In general there is sparse seismicity on the SAF in southern California, particularly when compared to the linear seismicity features that characterize the SAF in central California. However, there are two regions where groups of earthquakes are close to the SAF and aligned roughly parallel to the fault. One of these is between Palmdale and Wrightwood along the northern side of the San Gabriel Mountains. Figure 7.13 shows a map view and cross-sections of earthquake locations in the western part of this region, where the seismicity is densest. Focal mechanisms are plotted from the quality 1 and 2 solutions of J. Hardebeck (2005, http://www.data.scec.org/research/socal_focal_JLH.html; see also Hardebeck and Shearer, 2003). The bulk of the seismicity is located several kilometers south of the surface expression of the SAF, a much larger difference than our estimated location errors. The orientation of the SAF at depth is not known but is often assumed to be vertical (Community Fault Model, updated January 2004, by Shaw *et al.*, http://structure.harvard.edu/cfm, also see Plesch *et al.*, 2002). The mechanisms are mainly reverse, oblique and right-lateral strike slip, with relatively few mechanisms matching exactly the expected motion along the SAF. In cross-section the seismicity often appears to roughly align on southwest dipping planes. The focal mechanisms for cross-sections AB and CD are consistent with reverse faulting on these planes. The seismicity is more complex in cross-section EF where the events are closer to the SAF surface trace. Earthquakes located south of the fault deepen to the southwest but have mainly vertical, strike-slip mechanisms. It is possible that these events are located on strike-slip faults

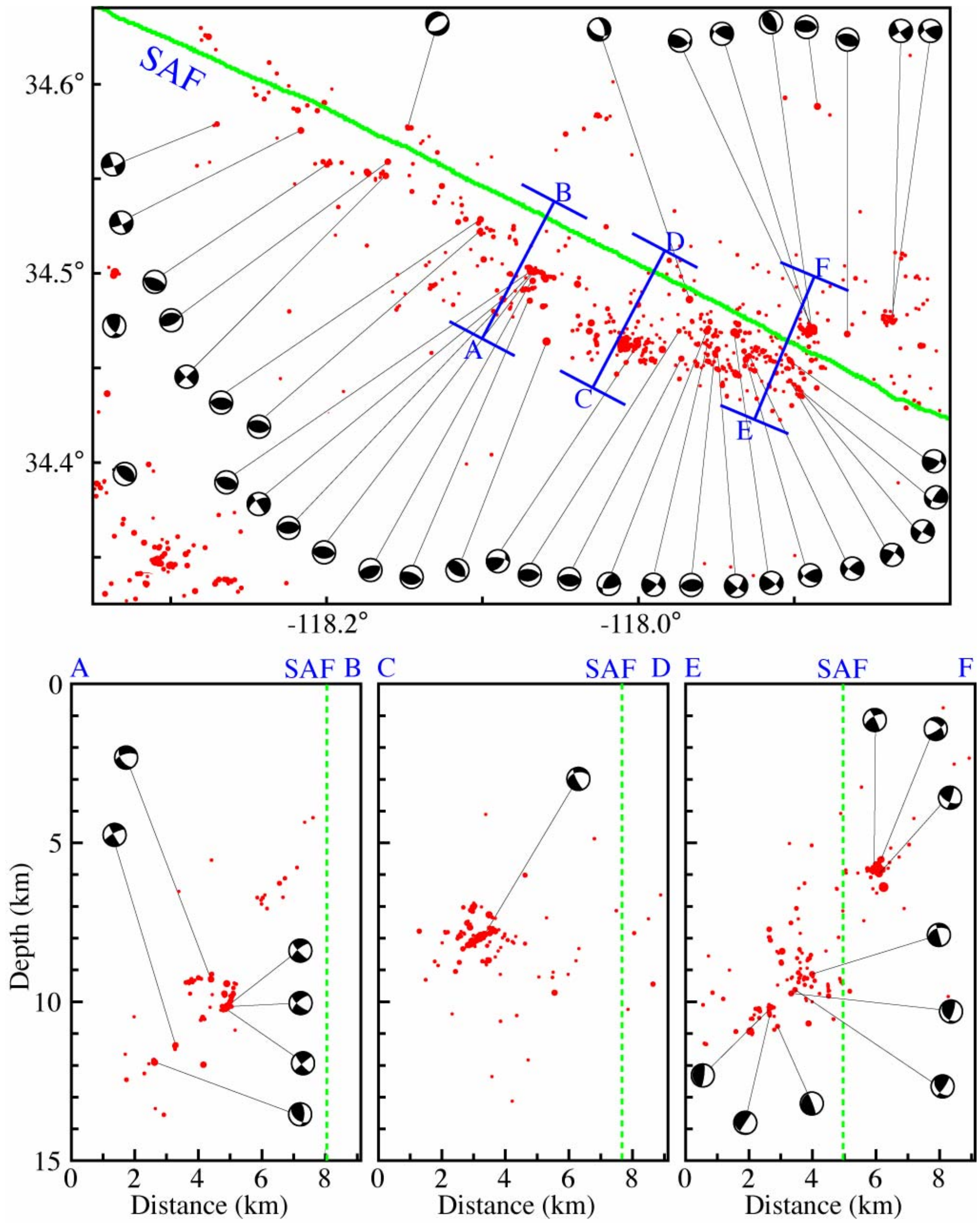

Figure 7.13. Seismicity near the San Andreas Fault (SAF) north of the San Gabriel Mountains, shown in map view and the labeled cross-sections. Focal mechanisms are from the Hardebeck 2005 catalog (see text). The dashed lines show the vertical projection of the known surface trace of the SAF; the true position of the fault at depth is uncertain.

parallel to the SAF or even on the SAF itself if the fault dips slightly to the southwest at depth. However, there is also a concentration of seismicity at 6 km depth just north of the SAF, which contains reverse faulting mechanisms of varying orientation.

The second region is northeast of the Salton Sea along the southernmost section of the SAF and is plotted in Figure 7.14. The seismicity is located 3 to 5 km to the northeast of the surface trace of the SAF, a separation that greatly exceeds any likely errors in our locations. Most of the earthquakes are between 6 and 11 km deep and roughly align on northeast dipping planes whose surface projection is close to the SAF. High-quality focal mechanisms are sparse in this region but the majority suggest right-lateral strike-slip motion, oriented parallel to the SAF. An exception is a concentration of seismicity in cross-section CD, which contains 3 normal faulting mechanisms. However, the bulk of the seismicity could be occurring on the SAF if it dips about 60 degrees to the northeast. This geometry could also help explain geodetic data for this area, which indicate that the maximum shear strain is displaced about 7 km northeast of the surface trace of the SAF (Fialko, 2006).

Our new earthquake locations are often sufficiently precise within similar event clusters that seismicity planes can be identified at relatively small scales (typical examples are from 0.5 to 2 km across). This resolution should permit much more detailed mapping of fault geometries than has previously been possible using catalogs derived from more standard earthquake location methods, at least for those faults currently illuminated by seismicity. The orientations of these planes can also help resolve the ambiguity between the primary and auxiliary planes in focal mechanism solutions (Shearer *et al.*, 2003).

7.10 Conclusions

We present high-precision earthquake locations for southern California from 1981 to 2005 computed using waveform cross-correlation with a new robust least-squares method. We examine 6 more years of data and many more cross-correlated event pairs in this study relative to our previous catalog. We use a new 3-D velocity model to improve absolute location accuracy and apply a new differential time relocation method that is very robust to outliers in the data. The location error estimates provide information on the

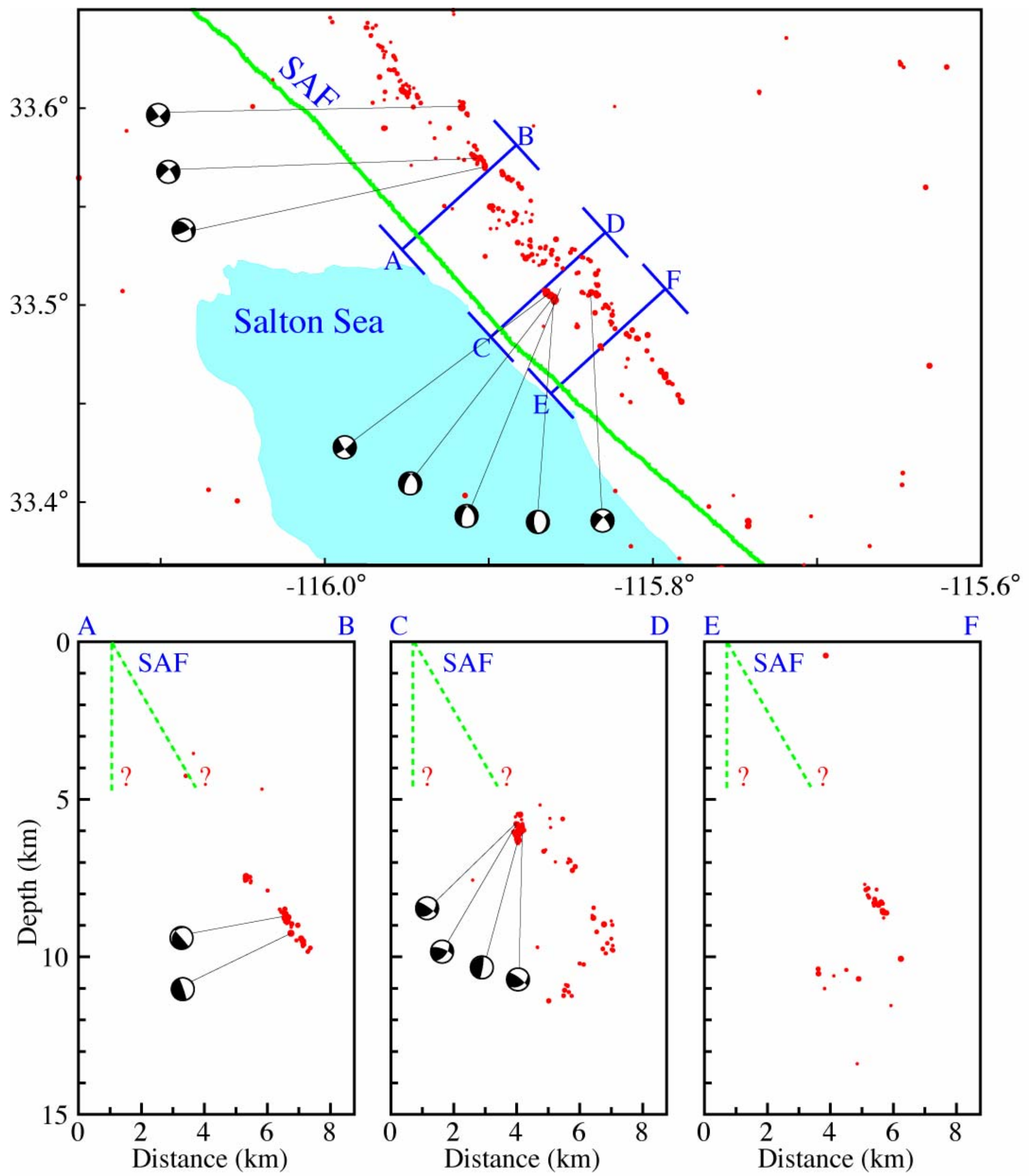

Figure 7.14. Seismicity near the San Andreas Fault (SAF) north of the Salton Sea, shown in map view and the labeled cross-sections. Focal mechanisms are from the Hardebeck 2005 catalog (see text). The labeled line shows the known surface trace of the SAF; the true position of the fault at depth is uncertain.

location quality for individual events and the overall dataset. These results build on our earlier relocation work and provide additional insight regarding the fine-scale seismicity structure in southern California. Our catalog is available through the Southern California Earthquake Data Center. Ultimately our goal is to implement these methods into routine network practice so that future events can be located quickly to the same accuracy as the complete catalog.

7.11 Acknowledgments

We thank Cliff Thurber for his SIMULPS tomography package and Paul Wessel and Walter Smith for developing and supporting the GMT mapping tools (http://gmt.soest.hawaii.edu/). Funding for this research was provided by NEHRP/USGS grant 03HQPA0001. This research was also supported by the Southern California Earthquake Center, which is funded by NSF Cooperative Agreement EAR-0106924 and USGS Cooperative Agreement 02HQAG0008. The SCEC contribution number for this paper is 1064.

7.12 References

Astiz, L. and P. M. Shearer (2000). Earthquake locations in the inner continental borderland, offshore southern California. *Bull. Seismol. Soc. Am.*, **90**, 425–449.

Astiz, L., P. M. Shearer and D. C. Agnew (2000). Precise relocations and stress change calculations for the Upland earthquake sequence in southern California. *J. Geophys. Res.*, **105**, 2937–2953.

Dodge, D. A., G. C. Beroza and W. L. Ellsworth (1995). Foreshock sequence of the 1992 Landers, California, earthquake and its implications for earthquake nucleation. *J. Geophys. Res.*, **100**, 9865–9880.

Eberhart-Phillips, D. (1990). Three-dimensional P and S velocity structure in the Coalinga region, California. *J. Geophys. Res.*, **95**, 15,343–15,363.

Efron, B. and G. Gong (1983). A leisurely look at the bootstrap, the jackknife and cross-validation. *Am. Statist.*, **37**, 36–48.

Efron, B. and R. Tibshirani (1991). Statistical data analysis in the computer age. *Science*, **253**, 390–395.

Evans, J. R., D. Eberhart-Phillips and C. H. Thurber (1994). User's manual for SIMULPS12 for imaging Vp and Vp/Vs: A derivative of the "Thurber" tomographic inversion SIMUL3 for local earthquakes and explosions. *U. S. Geol. Surv. open-File Rep*, 94–431.

Felzer, K. R. and E. E. Brodsky (2006). Decay of aftershock density with distance indicates triggering by dynamic stress. *Nature*, **441**, 735–738.

Fialko, Y. (2006). Interseismic strain accumulation and earthquake potential on the southern San Andreas fault system. *Nature*, **441**, 968–971.

Gillard, D., A. M. Rubin and P. Okubo (1996). Highly concentrated seismicity caused by deformation of Kilauea's deep magma system. *Nature*, **384**, 343–346.

Got, J.-L., J. Fréchet and F. W. Klein (1994). Deep fault plane geometry inferred from multiplet relative relocation beneath the south flank of Kilauea. *J. Geophys. Res.*, **99**, 15,375–15,386.

Hardebeck, J. L. and P. M. Shearer (2003). Using S/P amplitude ratios to constrain the focal mechanisms of small earthquakes. *Bull. Seismol. Soc. Am.*, **93**, 2434–2444.

Hartigan, J. A. (1975). *Clustering Algorithms*. John Wiley, New York.

Hauksson, E. (2000). Crustal structure and seismicity distribution adjacent to the Pacific and North America plate boundary in southern California. *J. Geophys. Res.*, **105**, 13,875–13,903.

Hauksson, E. and P. Shearer (2005). Southern California hypocenter relocation with waveform cross-correlation, Part 1: results using the double-difference method. *Bull. Seismol. Soc. Am.*, **95**, 896–903.

Hauksson, E., J. Woessner and P. Shearer (2006). Associating seismicity to late Quaternary faults in southern California. *Eos Trans. AGU*, **87**, Fall Meet. Suppl., Abstract S11B–04.

Huber, P. J. (1973). Robust regression: asymptotics, conjectures and monte carlo. *Ann. Statist.*, **1**, 799–821.

Kagan, Y. Y. (2006). Earthquake spatial distribution: the correlation dimension. *Geophys. J. Int.*, doi:10.1111/j.1365–246X.2006.03251.x.

Lin, G. and P. M. Shearer (2005). Tests of relative earthquake location techniques using synthetic data. *J. Geophys. Res.*, **110**, B04304, doi: 10.1029/2004JB003380.

Lin, G. and P. M. Shearer (2007). Estimating local Vp/Vs ratios within similar earthquake clusters. *Bull. Seismol. Soc. Am.*, in press.

Lin, G., P. M. Shearer, E. Hauksson and C. H. Thurber (2007). A 3-D crustal velocity model for southern California from a composite event method. *J. Geophys. Res.*, submitted.

Liu, J., K. Sieh and E. Hauksson (2003). A structural interpretation of the aftershock "cloud" of the 1992 Mw 7.3 Landers Earthquake. *Bull. Seismol. Soc. Am.*, **93**, 1333–1344.

Lohman, R. B. and J. J. McGuire (2006). Earthquake swarms driven by aseismic creep in the Salton Trough, CA. *Water Resources Research*, under revision.

Nadeau, R. M., W. Foxall and T. V. McEvilly (1995). Clustering and periodic recurrence of microearthquakes on the San Andreas Fault at Parkfield, California. *Science*, **267**, 503–507.

Nakamura, Y. (1978). A_1 moonquakes: source distribution and mechanism. *Proc. Lunar Planet. Sci. Conf.*, **9**, 3589–3607.

Nicholson, T., M. Sambridge and O. Gudmundsson (2004). Three-dimensional empirical traveltimes: construction and applications. *Geophys. J. Int.*, **156**, 307–328.

Plesch, A., J. H. Shaw, J. Dolan, L. Grant, E. Hauksson, M. Kamerling, M. Legg, S. Lindvall, C. Nicholson, T. Rockwell, C. Sorlien and R. Yeats (2002). SCEC 3D Community Fault Model for southern California. *Eos Trans. AGU*, **83**, Fall Meet. Suppl., Abstract S21A–0966.

Powers, P. and T. Jordan (2005). Seismicity rate vs. distance from strike-slip faults in southern California. *Eos Trans. AGU*, **86**, S13B–0199.

Richards-Dinger, K. B. and P. M. Shearer (2000). Earthquake locations in southern California obtained using source-specific station terms. *J. Geophys. Res.*, **105**, 10,939–10,960.

Rubin, A. M., D. Gillard and J.-L. Got (1999). Streaks of microearthquakes along creeping faults. *Nature*, **400**, 635–641.

Schaff, D. P. and F. Waldhauser (2005). Waveform cross-correlation-based differential travel-time measurements at the Northern California Seismic Network. *Bull. Seismol. Soc. Am.*, **95**, 2446–2461.

Shearer, P. M. (1997). Improving local earthquake locations using the L1 norm and waveform cross correlation: application to the Whittier Narrows, California, aftershock sequence. *J. Geophys. Res.*, **102**, 8269–8283.

Shearer, P. M. (1998). Evidence from a cluster of small earthquakes for a fault at 18 km depth beneath Oak Ridge, southern California. *Bull. Seismol. Soc. Am.*, **88**, 1327–1336.

Shearer, P. M. (2002). Parallel fault strands at 9-km depth resolved on the Imperial Fault, southern California. *Geophys. Res. Lett.*, **29**, doi: 10.1029/2002GL015302.

Shearer, P. M., J. L. Hardebeck, L. Astiz and K. B. Richards-Dinger (2003). Analysis of similar event clusters in aftershocks of the 1994 Northridge, California, earthquake. *J. Geophys. Res.*, **108**, B1, 2035, doi 10.1029/2001JB000685.

Shearer, P. M., E. Hauksson and G. Lin (2005). Southern California hypocenter relocation with waveform cross-correlation, Part 2: results using source-specific station terms and cluster analysis. *Bull. Seismol. Soc. Am.*, **95**, 904–915.

Thurber, C. and D. Eberhart-Phillips (1999). Local earthquake tomography with flexible gridding. *Comp. Geosci.*, **25**, 809–818.

Thurber, C. H. (1983). Earthquake locations and three-dimensional crustal structure in the Coyote Lake area, central California. *J. Geophys. Res.*, **88**, 8226–8236.

Thurber, C. H. (1992). Hypocenter-velocity structure coupling in local earthquake tomography. *Phys. Earth Planet. Inter.*, **75**, 55–62.

Thurber, C. H. (1993). Local earthquake tomography: velocities and Vp/Vs-theory. *in: Seismic Tomogrphy: Theory and Practice*, eds. H. M. Iyer and K. Hirahara, Chapman and Hall, London, 563–583.

Waldhauser, F. (2001). hypoDD: A program to compute double-difference hypocenter locations (hypoDD version 1.0, 03/2001). *U. S. Geol. Surv. open-File Rept.*, 01–113.

Waldhauser, F. and W. L. Ellsworth (2000). A double-difference earthquake location algorithm: method and application to the Northern Hayward Fault, California. *Bull. Seismol. Soc. Am.*, **90**, 1353–1368.

Waldhauser, F., W. L. Ellsworth and A. Cole (1999). Slip-parallel seismic lineations on the northern Hayward Fault, California. *Geophys. Res. Lett.*, **26**, 3525–3528.

Zhang, H. and C. H. Thurber (2003). Double-difference tomography: the method and its application to the Hayward Fault, California. *Bull. Seismol. Soc. Am.*, **93**, 1875–1889.

The text of this chapter, in full, is a reformatted version of the material as it appears in Lin, G., P. Shearer and E. Hauksson, Southern California seismicity from 1981 to 2005 relocated using waveform cross-correlation, submitted for publication in *Journal of Geophysical Research*, 2007. The dissertation author was the primary researcher and author. The co-authors directed and supervised the research which forms the basis of this chapter.

Chapter 8

Conclusions

8.1 Summary of Main Results

In this dissertation, I have considered several aspects of improvements in earthquake locations. A few important accomplishments and conclusions of this study can be summarized as follows:

- I compared three relative earthquake location techniques based on synthetic data. The source-specific station term (SSST) location method provides improved relative locations of comparable accuracy to other methods (e.g., the Double-Difference location method, Waldhauser and Ellsworth, 2000; Waldhauser, 2001) for both single compact event clusters and distributed seismicity. A new method — the shrinking box SSST method — is also introduced, which not only provides similar improvements in relative earthquake locations with other techniques, but also improves absolute location accuracy compared to the simple SSST method. The advantage of our method is that the event location part of the calculation is separate from the station term calculation and can be performed quickly using any desired single event location method.

- Controlled sources are often applied in simultaneous earthquake location and velocity inversions to provide absolute reference locations for three-dimensional velocity models and to constrain the shallow crustal structure. I have shown that absolute locations to about $\sim$100 m accuracy can be obtained for quarry seismicity by using remote sensing data . This can provide additional ground truth locations to add to the existing calibration shot data. The 19 relocated quarry blasts obtained by this method are used in our three-dimensional velocity model study for southern California in

Chapter 6.

- We released the COMPLOC software package to the community and provide documentation in Chapter 4. This location package allows users to greatly improve relative event locations using the SSST location algorithm with phase data. However, the current release does not permit use of waveform cross-correlation differential times.

- The V_p/V_s method in Chapter 5 was developed and tested to estimate local V_p/V_s ratios for compact similar earthquake clusters using the precise P- and S- differential times obtained using waveform cross-correlation. Our technique has higher resolution for near-source V_p/V_s ratios than typical tomographic inversion methods, provides constraints on near-fault rock properties and helps improve relative earthquake locations.

- A new three-dimensional seismic velocity model for southern California is developed using the "composite event method" applied to Thurber's SIMULPS algorithm. The advantage of using composite events rather than single master events is that the random picking error is reduced by averaging picks from many nearby events and that the maximum possible number of stations can be included for each event. Our velocity model is similar to models from previous studies but also has some new features. The model can be used as a starting point for structural studies, earthquake locations, and ground motion calculations.

- Based on the three-dimensional velocity model in Chapter 6, waveform cross-correlation and cluster analysis, we obtain a new earthquake location catalog for about 450,000 southern California earthquakes between 1981 and 2005. Our new catalog is available through the Southern California Earthquake Data Center and we anticipate that it will be useful to a variety of researchers studying seismicity and tectonics in southern California. In particular our improved locations should help to resolve details of fine-scale fault structure in regions of active seismicity.

8.2 Suggestions for Future Research

My Ph.D. research focuses on improving earthquake locations in southern California, but the techniques can be applied elsewhere in the world. It will be useful to extend these studies to other areas and test their applicabilities.

The SSST location method can greatly improve relative earthquake locations. The COMPLOC location package of the SSST algorithm is helpful for researchers to relocate events with only phase data. However, this package does not provide location error estimates and does not include differential times from waveform cross-correlation. The parameters that are often used to stabilize the location process, such as damping and weighting, are also not used in the package. This has the advantage of simplifying the program and might not be necessary due to the use of more robust statistical methods (e.g., L_1 norm or our robust least-squares method) than the classical least-squares approach. However, these should be considered in the next available release.

Our V_p/V_s estimate technique provides higher resolution of V_p/V_s ratios in source regions than tomographic inversions because of the high accuracy of differential times from waveform cross-correlation. It would be good to check the consistency of the ratios from this study with the tomographic results and with the real rock properties. It is likely that more accurate V_p/V_s ratios will stabilize the location process and improve relative locations. The current waveform cross-correlation locations were obtained using a fixed seismic velocity model. It will be interesting to apply the V_p/V_s ratios recovered from this technique to the location process to see how they affect earthquake locations.

Seismic structure studies are important in both local and regional scales to help us better understand Earth structure. My current use of a three-dimensional velocity model is mainly to improve absolute earthquake locations, but the model should also be helpful in other studies, such as resolving the geological structure of the crust, performing path and site effect studies, and computing strong ground motion simulations. It will be instructive to relate the velocity models with the relevant geological structures and other associated studies. It is also surprising to find the association of seismically active regions with low V_p/V_s ratios. However, it is possible that unresolved fine-scale structure in V_p/V_s may be present near seismically active areas that would yield very different V_p/V_s values near the earthquakes themselves due to the crude resolution of our tomography model compared to the accuracy of the earthquake locations. A promising way to study this possibility would be to directly estimate local V_p/V_s ratios within similar event clusters using the method in Chapter 5.

The current LSH location catalog for southern California seismicity provides both absolute and relative location errors. The bootstrap approach is a useful but inefficient way to estimate the relative location errors in each cluster, because this is equivalent to relocating the whole catalog several times. The reason we used the bootstrap approach is that it is difficult to apply the classical χ^2 misfit criteria to our robust least-squares method (or any other non-least-squares method). It would be desirable to develop a systematically efficient method to estimate both absolute and relative location errors. Considering the ongoing seismicity in southern California and the need for accurate locations in research on recent earthquakes, it will be very helpful to work out a routine so that future events can be located quickly to the same accuracy as the complete catalog.

8.3 References

Waldhauser, F. (2001). hypoDD: A program to compute double-difference hypocenter locations (hypoDD version 1.0, 03/2001). *U. S. Geol. Surv. open-File Rept.*, 01–113.

Waldhauser, F. and W. L. Ellsworth (2000). A double-difference earthquake location algorithm: method and application to the Northern Hayward Fault, California. *Bull. Seismol. Soc. Am.*, **90**, 1353–1368.